

**DIFFEOMORPHIC MATCHING AND DYNAMIC  
DEFORMABLE SHAPES**

---

A Dissertation  
Presented to  
the Faculty of the Department of Mathematics  
University of Houston

---

In Partial Fulfillment  
of the Requirements for the Degree  
Doctor of Philosophy

---

By  
Aarti Jajoo  
December 2011

**DIFFEOMORPHIC MATCHING AND DYNAMIC  
DEFORMABLE SHAPES**

---

Aarti Jajoo

APPROVED:

---

Prof. Ronald H. W. Hoppe  
Chairman

---

Prof. Robert Azencott  
Co-Chairman

---

Prof. Roland Glowinski

---

Prof. Jiwen He

---

Prof. Matthias Heinkenschloss

---

Dean, College of Natural Sciences and Mathematics

# Acknowledgements

This thesis work would not have been possible without collaborative efforts and support from a lot of people. Firstly, I would like to thank both my advisers Prof. Dr. R. Azencott and Prof. Dr. R. Hoppe for introducing me to such an interesting field. Without their guidance, support, and patience this work wouldn't have been possible. I am indebted to both of them.

I also want to thank Prof. Dr. J. He for various useful discussions I have had with him, he has been very generous while sharing ideas. I also want to thank Prof. Dr. R. Glowinski for his various useful remarks. I want to thank Prof. Dr. M. Heinkenschloss for his useful remarks and feedback for the thesis. Furthermore, I am really thankful to all of them for generously agreeing to be part of my committee.

I would also want to thank Dr. A. Martynenko for sharing his computational skills.

I would like to thank all the professors and staff members at the Math Department, Univ. of Houston. I would also like to thank all the faculty members of Mathematical Sciences Foundations, Delhi. I want to thank all my professors at Univ. of Rajasthan and Maharani's College, specially Prof. Dr. K. N. Singh and Prof. Dr. M. Garg.

Last but not the least, I would like to mention the great support and faith I have got from my parents, brother and sister, other family members, and friends (here and back home) all these years, without which certainly it wouldn't have been possible to reach here.

---

## Contents

---

<b>1</b>	<b>Introduction</b>	<b>1</b>
<b>2</b>	<b>Diffeomorphic Shape Matching</b>	<b>5</b>
2.1	Brief History . . . . .	6
2.2	Mathematical Setup . . . . .	8
2.2.1	Space of Diffeomorphisms Associated with Time Dependent Vector Fields . . . . .	8
2.2.2	Reproducing Kernel Hilbert Space . . . . .	11
2.2.3	Distance between Shapes . . . . .	14
2.3	Variational Formulation in Context of Multiple Snapshots . . . . .	16
<b>3</b>	<b>Existence of a Solution of the Variational Problem. Necessary Optimality Conditions</b>	<b>18</b>
3.1	Existence of the Variational Problem . . . . .	19
3.2	Necessary Optimality Conditions . . . . .	25
<b>4</b>	<b>Dirac Measures and Diffeomorphic Point Matching</b>	<b>32</b>

<b>5</b>	<b>The Fully Discrete Optimal Control Problem</b>	<b>38</b>
<b>6</b>	<b>Numerical Solutions of the Optimization Problem</b>	<b>43</b>
6.1	Diffeomorphic Matching for Multiple Snapshots of 3D Curves and Surfaces . . . . .	43
6.1.1	Initialization of the Gradient Method with Armijo Line Search	45
6.1.2	Smoothing of the Hausdorff Disparity . . . . .	48
6.1.3	Choice of the Scale Parameters in the Gaussian Kernels . . . . .	49
6.2	Continuation in the Regularization Parameter . . . . .	50
<b>7</b>	<b>Smoothing in Time Domain</b>	<b>54</b>
7.1	Solutions with Non-smooth Transitions in Time . . . . .	55
7.1.1	Data . . . . .	55
7.1.2	Quantifying the Non-smoothness of Solution . . . . .	56
7.2	Modified Functional . . . . .	56
7.3	Adding Local Smoothing Terms to the Objective Functional . . . . .	59
7.3.1	Numerical Experiments . . . . .	59
7.4	Adding the Global Smoothing Term to the Objective Functional . . . . .	60
7.4.1	Results for Curves . . . . .	60
7.4.2	Result for Surfaces . . . . .	64
<b>8</b>	<b>Numerical Results: Reconstructed Motion of Human Mitral Valve</b>	<b>66</b>
8.1	Human Mitral Valve Apparatus . . . . .	66
8.1.1	Anatomy and Physiology of Mitral Valve . . . . .	68
8.1.2	Mitral Valve Regurgitation . . . . .	69
8.1.3	Mitral Valve Regurgitation Treatment: Repair vs. Replacement	70
8.1.4	Mitral Valve Shape Models: From Ecocardiographic Images to Static Modeling using NURBS . . . . .	71
8.2	Mitral Valve Apparatus as a NURBS Model . . . . .	73

## CONTENTS

---

8.3	Multiple Snapshots for the Mitral Annulus and Leaflets . . . . .	75
8.4	Diffeomorphic Matching for Multiple Annulus Snapshots . . . . .	76
8.4.1	Smoothed Hausdorff Matching for Multiple Annulus Snapshots.	78
8.4.2	Diffeomorphic Matching for Multiple Annulus Snapshots: Measure Matching. . . . .	79
8.4.3	Diffeomorphic Matching for 10 Annulus Snapshots . . . . .	83
8.5	Diffeomorphic Matching of the Anterior Leaflet . . . . .	84
8.6	Diffeomorphic Matching for Multiple Snapshots of the Posterior Leaflet	89
8.7	Diffeomorphic Matching of the Whole Mitral Valve Apparatus . . . . .	93
<b>9</b>	<b>Conclusions and Future Work</b>	<b>95</b>
	<b>Bibliography</b>	<b>99</b>

---

## List of Figures

---

7.1	x axis represent the time and y axis represent $\theta_t^{\text{Avg}}$ as defined in 7.2, 'o' represent the value at time $t_j, j = 1, \dots, 9$ i.e. time instances with known snapshots . . . . .	57
7.2	Left figure depicts the time evolution of the average of the norm of $\alpha(t)$ , right figure depicts the evolution of the average of finite difference derivative of $\alpha(t)$ . . . . .	57
7.3	average of angles: green-for the original solution, blue-for $\mu = 0.5$ , pink-for $\mu = 2$ , red-for $\mu = 4$ solution with local smoothing term . . .	60
7.4	average of the norm of $\alpha_i, 0 \leq i \leq N_x - 1$ (left), norm of the difference between the alpha of two consecutive time(right) . . . . .	61
7.5	average of angles: green-the original solution, blue- $\mu = 0.5$ , pink- $\mu = 2$ . . . . .	62
7.6	average of the norm of $\alpha_t$ (left), norm of the difference between the alpha of two consecutive time(right) . . . . .	62
7.7	One trajetory: uniform time steps and different $\mu$ : $\mu = 0$ -green, $\mu = 0.5$ -blue, $\mu = 2$ -pink . . . . .	63
7.8	Average of angles: green-for the original solution, blue-for $\mu = 0.5$ , pink-for $\mu = 2$ . . . . .	64

*LIST OF FIGURES*

---

7.9	Represent the accuracy of the matching, as we can see all the curves overlap and hence we don't compromise on accuracy . . . . .	65
8.1	Structure of Human Heart . . . . .	67
8.2	The four valves during diastole and systole . . . . .	68
8.3	Mitral valve posterior surface, chordae tendinea and papillary muscles	70
8.4	Mitral valve: the middle line is the coaptation line along which the surfaces of the anterior and posterior leaflets meet when the valve is closed. The closed black thick curve is the mitral annulus. . . . .	74
8.5	The 5 closed curves are 5 successive annulus snapshots. The dotted curve is the initial snapshot. From bottom to top, the next 3 curves are the intermediary snapshots and the last one is the final target. The vertical '—' lines are computed deformation trajectories for selected points of the reference curve. . . . .	75
8.6	Diffeomorphic matching for multiple mitral annulus snapshots, using smoothed Hausdorff distances: Convergence history for the geometric accuracy indicators $\text{Dist}_j$ and for the smoothed Hausdorff disparity components $\text{Disp}_j$ . . . . .	78
8.7	Diffeomorphic matching for multiple annulus snapshots, using smoothed Hausdorff distances: Pareto frontiers for the geometric accuracy indicators $\text{Dist}_j$ (top left), for the Hausdorff disparities $\text{Disp}_j$ (top right), and for the global Hausdorff disparity $\sum_j \text{Disp}_j$ (bottom). . . . .	80
8.8	Diffeomorphic matching for multiple annulus snapshots, using measure matching disparities: Convergence history for the individual geometric accuracy indicators $\text{Dist}_j$ (left) and the measure matching disparities $\text{Disp}_j$ (right). . . . .	81
8.9	Diffeomorphic matching for multiple annulus snapshots using measure matching disparities: Pareto frontiers for the geometric accuracy indicators $\text{Dist}_j$ (top left), for the individual measure matching disparities $\text{Disp}_j$ (top right), and for the global measure matching disparity $\sum_j \text{Disp}_j$ (bottom). . . . .	82
8.10	Diffeomorphic matching for ten annulus snapshots using Hausdorff disparities: Convergence history of geometric accuracies (left) and corresponding Pareto frontiers (right) using a single regularization parameter $\lambda$ for the nine Hausdorff disparities. . . . .	83

*LIST OF FIGURES*

---

8.11	Diffeomorphic matching for ten annulus snapshots: Convergence history of the geometric accuracies (left) and corresponding Pareto frontiers (right) using nine dynamic regularization parameters $\lambda_j$ . . . . .	84
8.12	Diffeomorphic matching of four anterior leaflet snapshots: Pareto frontiers for the separate Hausdorff disparities to snapshots (left) and for the global Hausdorff disparity (right). . . . .	85
8.13	Pareto frontiers for the maximum distances to snapshots (left) and for their 90th percentiles (right). . . . .	85
8.14	Computed deformations matching four snapshots of the anterior leaflet at instants 0, 1, 5, 10 . . . . .	86
8.15	Computed deformations of the anterior leaflet boundary: for easier visualization, the boundary deformations are displayed separately for instants 0, 1 and for instants 1, 5, 10. . . . .	87
8.16	Matching errors between the computed anterior leaflet deformations $\hat{S}_j$ and the snapshots $S_j$ . . . . .	88
8.17	Diffeomorphic matching for four posterior leaflet snapshots: Geometric accuracy indicators and Pareto frontiers for strictly equal regularization weights $\lambda_j$ . . . . .	90
8.18	Diffeomorphic matching for four posterior leaflet snapshots: Geometric accuracy indicators and Pareto frontiers for dynamically adjusted regularization weights $\lambda_j$ . . . . .	90
8.19	Computed deformations matching four snapshots of the posterior leaflet at instants 0, 1, 5, 10. . . . .	91
8.20	Computed deformations of the posterior leaflet boundary: the continuous boundary deformations are displayed separately for instants 0, 1 and for instants 1, 5, 10. . . . .	92
8.21	Matching errors between the computed posterior leaflet deformations $\hat{S}_j$ and the snapshots $S_j$ . . . . .	92
8.22	Diffeomorphic matching of the whole Mitral Valve Apparatus: Convergence history for the geometric matching accuracy. . . . .	94

---

## List of Tables

---

7.1	Performance indicator at different level of $\mu$ . . . . .	61
7.2	Sum of angles . . . . .	63
7.3	Sum of angles . . . . .	65

# CHAPTER 1

---

## Introduction

---

In medical applications such as clinical diagnosis and surgery as well as therapy planning there is often a need to analyze 3D movies of deformable anatomical objects. This analysis is based on 3D imaging modalities such as MRS (Magnetic Resonance Spectroscopy), PET (Positron Emission Tomography), SPECT (Single Photon Emission Computed Tomography) for functional information, and CT (Computed Tomography), MRI (Magnetic Resonance Imaging), Ultrasound Echography, X-ray, etc. for anatomical visualization. However, the 3D movies obtained by such imaging modalities are usually blurred by noise. The use of optical flow extraction methods in combination with expert tagging only allows to reconstruct snapshots  $S_j$  of the

---

anatomical object at successive time frames  $t_j, 0 \leq j \leq q$ . The task in automated 3D image matching is the reconstruction of the 3D movie on the basis of these snapshots. This can be achieved by a time dependent family of  $\mathbb{R}^3$  diffeomorphisms  $F_t$  such that  $F_{t_0}(S_0) = S_0$  and  $F_{t_j}(S_0)$  is as close to  $S_j, 1 \leq j \leq q$ , as possible in terms of appropriately chosen matching quality criteria. The matching of two snapshots  $S_0$  and  $S_1$  has been extensively studied in the literature. We refer to the concepts based on diffeomorphic matching as developed by Grenander, Miller, Trouvé, Younes, and others initiated during the second half of the nineties of the last century [23, 36, 49] and subsequently studied in [12, 17, 30, 32, 44, 45]. A comprehensive exposition of the basic methodologies of diffeomorphic matching as well as further references can be found in the recent monograph by Younes [56]. In this thesis, we will focus on the generalization of the concepts to an arbitrary number of snapshots resulting in a minimization problem to be treated within a variational framework featuring a Hilbert space setting by means of Reproducing Kernel Hilbert Spaces (RKHS). As an application in medical imaging, we will consider the reconstruction of 3D movies from echocardiographic data of the mitral valve apparatus of the human heart.

The thesis is organized as follows: After these introductory remarks, in Chapter 2 we provide the mathematical tools that we need to set up the variational framework for diffeomorphic matching. Moreover, we formulate the variational problem in case of multiple snapshots as an optimal control problem for an objective functional featuring a suitably chosen matching quality criterion and a regularization term by means of an associated energy. The underlying state equation is a dynamical system for the time dependent family of  $\mathbb{R}^3$  diffeomorphisms, representing the state, whereas the

---

control is a time dependent flow of vector fields.

Chapter 3 is devoted to a proof of the existence of a solution to that optimal control problem using standard tools from the calculus of variations and the theory of evolution equations. Moreover, Chapter 3 contains the derivation of the first order necessary optimality conditions involving an adjoint state equation in terms of a time dependent family of regular Borel measures that satisfy a backward-in-time evolution equation and a fundamental relationship between the adjoint state and the control which is the gradient equation with respect to the control reduced formulation of the problem.

The following chapters are concerned with the numerical solution of the optimal control problem. In particular, in Chapter 4 we consider a semi-discretization in space approximating the reference and target objects by point sets. Hence, the thus semi-discretized optimal control problem amounts to the solution of a diffeomorphic point matching problem [19, 34, 35]. The associated optimality system consists of a forward-in-time system of ordinary differential equations (ODEs) for the semi-discrete state, a backward-in-time system of ODEs for the semi-discrete adjoint state, as well as a gradient equation relating the semi-discrete adjoint state to the semi-discrete control.

Chapter 5 deals with a further discretization in time of the semi-discrete optimality system by applying the forward Euler scheme to the respective systems of ODEs. We show that the fully discretized optimality system admits an interpretation as the optimality conditions of an associated fully discrete optimal control problem.

In Chapter 6, we address the numerical solution of the fully discrete optimization

---

problem by a gradient method with Armijo line search. Particular emphasis will be on a continuation strategy for the regularization parameter in the objective functional and on the proper choice of the scaling parameter for the Gaussian kernel in the underlying RKHS.

In Chapter 7, we discuss a particular issue associated with the diffeomorphic matching of multiple snapshots which is the occurrence of discontinuities in the adjoint state due to jump conditions at the intermediate time frames. This leads to non-smooth transitions in the reconstructed 3D movie. As a possible remedy, we suggest the inclusion of a smoothing term in the objective functional.

The second part of the thesis is about the application of the algorithmic tools developed in the first part to the reconstruction of echocardiographic data of the human mitral valve apparatus during one heart cycle. In Chapter 8, we briefly address the use of interactive tagging to extract snapshots and their representation by non-uniform rational B-splines (NURBS) [7, 9]. The main part of this chapter is devoted to a detailed documentation of numerical results for the reconstructed motion of essential parts of the mitral valve such as the annulus and the anterior as well as the posterior leaflet [10].

In the final Chapter 10, we draw some conclusions and give an outlook on future work.

## CHAPTER 2

---

### Diffeomorphic Shape Matching

---

This chapter is dedicated to a brief summary of previous work related to the diffeomorphic framework followed by the mathematical setup required for the variational formulation associated with optimal matching of multiple snapshots. Throughout this chapter we will use standard notations from Lebesgue and Sobolev space theory (cf., e.g., [48]). In particular, we refer  $\Omega \subset \mathbb{R}^d, d \in \mathbb{N}$ , we refer to  $L^p(\Omega), 1 \leq p \leq \infty$ , as the Banach space of p-th power Lebesgue integrable vector valued functions with norm  $\|\cdot\|_{0,p,D}$  and to  $W^{s,p}(\Omega), s \in \mathbb{R}_+$ , as the associated Sobolev space with norm  $\|\cdot\|_{s,p,\Omega}$ . For  $p = 2$ , these space are Hilbert spaces, and we omit the subindex 2. For an interval  $I \subset \mathbb{R}_+$  and a Hilbert space  $V$  with norm  $\|\cdot\|_V$ , we denote

$L^p(I; V)$ ,  $1 \leq p \leq \infty$ , the Banach space of functions  $v : I \rightarrow V, t \in T \rightarrow v_t \in V$  with norm

$$\|v\|_{L^p(I;V)} := \left( \int_I \|v_t\|_V^p \right)^{1/p}.$$

We refer  $C(\Omega)$  as the Banach space of bounded, continuous functions on  $D$  with norm  $\|\cdot\|_{C(\Omega)}$  and by  $\mathcal{M}(\Omega)$  the dual space of regular Borel measures  $\mu$  with norm  $\|\mu\|_{\mathcal{M}} := \sup\{ | \langle \mu, \nu \rangle_{\mathcal{M};C} | \mid \|v\|_{C(\Omega)} \leq 1 \}$ , where  $\langle \cdot, \cdot \rangle_{\mathcal{M},C}$  stands for the dual pairing between  $\mathcal{M}(\Omega)$  and  $C(\Omega)$ , i.e.,

$$\langle \mu, \nu \rangle_{\mathcal{M};C} = \int \nu d\mu.$$

We denote  $C^{0,\kappa}$ ,  $\kappa > 0$ , refers to the subspace  $u \in C(\Omega)$  that are Holder continuous i.e. there exists a constant  $C \geq 0$  such that

$$|u(x) - u(y)| \leq C|x - y|^\kappa, \quad x, y \in \Omega.$$

$C^{0,\kappa}$  is a Banach space with the norm

$$\|u\|_{C^{0,\kappa}} := \|u\|_{C(\Omega)} + \sup_{x,y} \frac{|u(x) - u(y)|}{|x - y|^\kappa} \tag{2.1}$$

## 2.1 Brief History

In the field of image analysis there have been lot of developments occurred in the last few decades, with applications in medical imaging, etc. The main goal of such work was primarily to compare two observed images belonging to a same class of objects, e.g. brain images, images concerning facial expressions, etc. New variational methods were explored by G.Dupuis, J. Glaunès, U. Grenander, M. Miller, D. Mumford, A.

Trouvé, L. Younes et.al. [12, 23, 31, 32] with applications to a quantified comparison of images of human brains. In these papers, the regularization is achieved through the replacement of the rigid constraint  $F(S_0) = S_1$  by a soft constraint based on various geometric 'surface matching' distances  $\text{dis}[F(S_0), S_1]$ . The unknown diffeomorphism  $F$  is restricted to be of the form  $F = F^v$ , where  $F^v$  is generated by integration between times 0 and 1 of some time dependent flow  $v = (v_t)$  of smooth  $\mathbb{R}^3$ -vector fields  $v_t$ ,  $0 \leq t \leq 1$ . The vector fields  $v_t$  are required to belong to a Hilbert subspace  $V$  of the Banach space  $C_r^3$  of smooth functions from  $\mathbb{R}^3$  to  $\mathbb{R}^3$  tending to zero at infinity. The Hilbert space norm in  $V$  is assumed to be bounded by a constant multiple of the Banach space norm in  $C_r^3$ . Then, for some fixed constant  $\lambda > 0$  one considers the variational problem of finding a vector field flow  $v = (v_t)$  minimizing the cost functional

$$J(v) = \int_0^1 \|v_t\|_V^2 dt + \lambda \text{dis}[F^v(S_0), S_1], \quad (2.2)$$

which linearly combines a kinetic energy term and a surface matching term.

This variational point of view is directly linked (as  $\lambda \rightarrow \infty$ ) to the construction of *geodesics in infinite dimensional Lie groups of diffeomorphisms* in the spirit of ideas pioneered by Arnold, Ebin, and Marsden who showed (see, e.g., [4]) that for an incompressible fluid, obeying Euler equations, the spatial displacements  $F_t(x)$  between times 0 and  $t$  of fluid particles emanating from  $x \in \mathbb{R}^3$  minimize the integral in time and space of the fluid kinetic energy. The time dependent  $\mathbb{R}^3$ -diffeomorphisms  $F_t$  define a continuous path in the group of  $\mathbb{R}^3$ -diffeomorphisms, and this path is a geodesic  $t \rightarrow F_t$  of an infinite dimensional Lie group  $G$  of  $\mathbb{R}^3$ -diffeomorphisms, endowed with the local Hilbert metric defined by the fluid's kinetic energy on the

Lie algebra of  $G$ . This Lie algebra is naturally identified with the Hilbert space of smooth vector fields on  $\mathbb{R}^3$  defined by fluid velocities at time 0. The classical Euler fluid mechanical equations for the fluid velocities become precisely interpreted as the variational equations characterizing geodesics in  $G$ . Natural right-invariant deformation distances on the group  $G$  can then be associated to this Riemannian structure (see, e.g., [49]).

For the diffeomorphic matching of two smooth  $k$ -dimensional shapes ( $k \in \{1, 2, 3\}$ ) by  $\mathbb{R}^3$ -diffeomorphisms, the geometric view just outlined above has been intensively explored in [12, 23, 31, 49] and numerically implemented for comparisons of key anatomic parts of human brains such as the hippocampus, the temporal lobes, etc.

## 2.2 Mathematical Setup

### 2.2.1 Space of Diffeomorphisms Associated with Time Dependent Vector Fields

**Definition 2.1.** *A map  $\phi : \Omega \rightarrow \Omega$  is called diffeomorphism if:  $\phi$  is one-one, onto, continuously differentiable and  $\phi^{-1}$  is continuous.*

The collection of all such diffeomorphisms forms a group under the operation as composition of functions. We restrict our search of diffeomorphism to a particular class of diffeomorphisms: generated by time-dependent vector fields, the idea pioneered by U. Grenander et. al [23].

### 2.2.1.1 Time Dependent Vector Fields with Finite Kinetic Energy

We choose a Hilbert space  $V$  of vector fields on  $\mathbb{R}^3$  and we consider the associated Hilbert space  $L^2(I, V)$  of vector field flows  $v : t \rightarrow v_t \in V$ , indexed by a time parameter  $t$  in the interval  $I = [t_0, t_1]$ , having finite *kinetic energy*  $E(v)$  defined by

$$E(v) := \frac{1}{2} \|v\|_{L^2(I, V)}^2 = \frac{1}{2} \int_{t_0}^{t_1} \|v_t\|_V^2 dt. \quad (2.3)$$

We assume that the Hilbert space  $V$  of  $\mathbb{R}^3$ -vector fields is continuously embedded in a Sobolev space  $W^{s,2}(\mathbb{R}^3)^3$  for some  $s > 5/2$ . By the Sobolev embedding theorem,  $W^{s,2}(\mathbb{R}^3)^3, s > 5/2$ , is continuously embedded in the Banach space  $C^{1, s-5/2}(\mathbb{R}^3)^3$  of  $\mathbb{R}^3$ -vector fields.

### 2.2.1.2 Dynamic System of Diffeomorphic Deformations

For  $t \in I$  and  $v = (v_t)$  as above, we define the flow of  $\mathbb{R}^3$ -diffeomorphisms  $F_t$  as the solution of the flow dynamics equations

$$\partial_t F_t = v_t(F_t) \quad , \quad t \in I, \quad (2.4a)$$

$$F_0 = \text{Id}, \quad (2.4b)$$

where Id refers to the identity map of  $\mathbb{R}^3$ .

**Theorem 2.1.** *Assume  $v \in L^2(I; V)$  where  $V$  is continuously embedded in  $W^{s,2}(\mathbb{R}^3)$  for some  $s > 5/2$ . Then, the initial-value problem (2.4a),(2.4b) admits a unique solution.*

## 2.2. MATHEMATICAL SETUP

---

*Proof.* [23] We first show existence and uniqueness of a solution for  $t \in [0, \tau]$  with  $\tau \geq 0$  sufficiently small. To this end, we reformulate the initial-value problem 2.4 as the fixed point equation  $\mathcal{T}F = F$ , where the non-linear operator  $\mathcal{T} : C([0, \tau] \times \mathbb{R}^3)^3 \rightarrow C([0, \tau] \times \mathbb{R}^3)^3$  is given by

$$\mathcal{T}F_t = F_0 + \int_0^t v_s(F_s) ds.$$

For  $F^{(1)}, F^{(2)} \in C([0, \tau] \times \mathbb{R}^3)^3$  there holds

$$\|\mathcal{T}F^{(1)} - \mathcal{T}F^{(2)}\|_{C([0, \tau] \times \mathbb{R}^3)^3} = \max_{0 \leq t \leq \tau} \left| \int_0^t (v_s(F_s^{(1)}) - v_s(F_s^{(2)})) ds \right| \quad (2.5)$$

By the Sobolev embedding theorem [48], for  $3/2 < s < 5/2$  the Sobolev space  $W^{s,2}(\mathbb{R}^3)^3$  is continuously embedded in  $C^{1,s-3/2}(\mathbb{R}^3)^3$ , i.e., there exist a constant  $C_1 > 0$  such that

$$\|u\|_{C([0, \tau] \times \mathbb{R}^3)^3} \leq C_1 \|u\|_{s, \mathbb{R}^3}, \quad u \in W^{s,2}(\mathbb{R}^3). \quad (2.6)$$

Also, due to the assumed continuous embedding  $V \subset W^{s,2}(\mathbb{R}^3)$ , there exists  $C_2 > 0$  such that

$$\|u\|_{s, \mathbb{R}^3} \leq C_2 \|u\|_V, \quad u \in V. \quad (2.7)$$

Again due to Sobolev embedding theorem  $\forall v \in V$ ,  $v$  is a continuously differentiable function and hence  $v$  will satisfy Lipschitz condition, cf. Chapter 4 of [5].

Observing (2.6) and (2.7) and using the Cauchy-Schwartz inequality, it follows that

$$\begin{aligned} \|\mathcal{T}F^{(1)} - \mathcal{T}F^{(2)}\|_{C([0, \tau] \times \mathbb{R}^3)^3} &\leq C_1 C_2 \max_{0 \leq t \leq \tau} \int_0^t \|v_s\|_V |F_s^{(1)} - F_s^{(2)}|_{\mathbb{R}^3} ds \\ &\leq C_1 C_2 \tau^{\frac{1}{2}} \|v\|_{L^2([0, \tau]; V)} \|F^{(1)} - F^{(2)}\|_{C([0, \tau] \times \mathbb{R}^3)^3}. \end{aligned} \quad (2.8)$$

## 2.2. MATHEMATICAL SETUP

---

Hence, for  $\tau > 0$  such that  $C_1 C_2 \tau^{\frac{1}{2}} \|v\|_{L^2([0,\tau];V)} < 1$ , the non-linear operator  $\mathcal{T}$  is a contraction and we conclude. If  $\tau \geq 1$ , we are done. Otherwise, for  $m = 1, 2, \dots$  we successively consider (2.4b) on  $(m\tau, (m+1)\tau)$  with initial condition  $z_{m\tau}$  until  $(m+1)\tau \geq 1$ .  $\square$

**Theorem 2.2.** *Under the assumptions in Theorem 2.1, the solution  $F_t, t \in I$  of problem (2.4a),(2.4b) is an  $\mathbb{R}^3$ -diffeomorphism of smoothness class  $1 \leq r < s - 3/2$ .*

*Proof.* We refer to [23] for the proof.  $\square$

### 2.2.2 Reproducing Kernel Hilbert Space

In this section we define a RKHS and discuss the fundamental properties of RKHS. For more details we mainly refer to [47],[6].

**Definition 2.2.** *Let  $H$  be a Hilbert space of functions on  $\mathbb{R}^d$  with inner product  $(\cdot, \cdot)_H$  and norm  $\|\cdot\|_H$ . A function  $K : \mathbb{R} \times \mathbb{R} \rightarrow \mathbb{C}$  is said to be a reproducing kernel of  $H$ , if the following conditions are satisfied*

**RK1** *For every  $x \in \mathbb{R}^d$ , we have  $K_x \in H$ , where  $K_x : \mathbb{R}^d \rightarrow \mathbb{C}$  is the function given by*

$$K_x(y) = K(y, x) \quad , \quad y \in \mathbb{R}^d$$

**RK2** *For every  $x \in \mathbb{R}^d$  and every  $f \in H$  there holds*

$$f(x) = (f, K_x)_H$$

## 2.2. MATHEMATICAL SETUP

---

**Definition 2.3.** The kernel  $K$  is called Hermitian, if for any finite set of points  $\{y_1, \dots, y_n\} \subset \mathbb{R}^d$  and for any collection of  $\{\gamma_i | \gamma_i \in \mathbb{C}, 1 \leq i \leq n\}$  there holds

$$\sum_{i,j=1}^n \bar{\gamma}_i K(y_i, y_j) \gamma_j \in \mathbb{R},$$

and it is called positive definite, if

$$\sum_{i,j=1}^n \bar{\gamma}_i K(y_i, y_j) \gamma_j \geq 0.$$

**Definition 2.4.** The Hilbert space  $H$  is said to be a Reproducing Kernel Hilbert Space (RKHS), if there exists a reproducing kernel  $K$  on  $H$ .

**Remark 2.1.** By definition we observe that if we choose  $f = K_x$  in (RK2) and use (RK1), we obtain

$$K_x(y) = (K_x, K_y)_H = K(y, x), \quad x, y \in \mathbb{R}^d, \quad (2.9)$$

$$\|K_x\|_H = K(x, x)^{1/2}, \quad x \in \mathbb{R}^d. \quad (2.10)$$

**Theorem 2.3.** For any positive definite kernel  $K : \mathbb{R}^d \times \mathbb{R}^d \rightarrow \mathbb{C}$  there exists a uniquely determined RKHS of functions on  $\mathbb{R}^d$  admitting the reproducing kernel  $K$ .

*Proof.* Let  $H_0$  be the linear space of functions  $f$  on  $\mathbb{R}^d$  that can be represented as a linear combination of generating functions  $K_{x_i}$  with respect to a finite set of points  $x_i \in \mathbb{R}^d$ ,  $1 \leq i \leq n$ , according to

$$f(y) = \sum_{i=1}^n \alpha_i K_{x_i}(y), \quad y \in \mathbb{R}^d, \alpha_i \in \mathbb{C}, 1 \leq i \leq n. \quad (2.11)$$

For  $f$  as in (2.11) and  $g = \sum_{i=1}^m \beta_i K_{y_i}$ ,  $y_i \in \mathbb{R}^d$ ,  $\beta_i \in \mathbb{C}$ ,  $1 \leq i \leq m$ , we define an inner product  $(f, g)_{H_0}$  by means of

$$(f, g)_{H_0} := \sum_{i=1}^n \sum_{j=1}^m \alpha_i \bar{\beta}_j K(x_i, y_j). \quad (2.12)$$

## 2.2. MATHEMATICAL SETUP

---

It follows that for  $x \in \mathbb{R}^d$

$$(f, K(x, \cdot))_{H_0} = \sum_{i=1}^n K(x, x_i) = f(x)$$

i.e.,  $H_0$  has the reproducing property and the inner product  $(f, g)_{H_0}$  does not depend on the representation of the functions  $f, g \in H_0$ . We define  $H$  as the completion of the pre-Hilbert space  $(H_0, (\cdot, \cdot)_{H_0})$  and show that  $H$  has a unique representation as an RKHS with reproducing kernel  $K$ . For this, let  $(f_n)_{\mathbb{N}}, (g_m)_{\mathbb{N}}, f_n, g_m \in H_0, n, m \in \mathbb{N}$ , be two Cauchy sequences in  $H_0$  with limit functions  $f, g : \mathbb{R}^d \rightarrow \mathbb{R}$ . We define an inner product

$$(f, g)_H := \lim_{n, m \rightarrow \infty} (f_n, g_m)_{H_0}.$$

Using the triangle inequality and the Cauchy Schwarz inequality it can be shown that  $(\cdot, \cdot)_H$  is well defined. In order to verify that  $K$  has the reproducing property with respect to  $H$ , let  $f \in H$  and  $(f_n)_{\mathbb{N}} \subset H$  such that  $f_n \rightarrow f$  as  $n \rightarrow \infty$ . Then, for  $x \in \mathbb{R}^d$  there holds

$$f(x) = \lim_{n \rightarrow \infty} f_n(x) = \lim_{n \rightarrow \infty} (f_n, K_x)_{H_0} = (\lim_{n \rightarrow \infty} f_n, K_x)_{H_0} = (f, K_x)_H.$$

The uniqueness of  $H$  can be established as follows: Assume  $\hat{H}$  to be another RKHS with the same reproducing kernel  $K$ . Since  $K_x \in \hat{H}, x \in \mathbb{R}^d$ , we have  $H_0 \in \hat{H}$ . If  $f \in \hat{H}$  satisfies  $f(x) = (f, K_x)_{\hat{H}}, x \in \mathbb{R}^d$ , then  $f \equiv 0$  and hence,  $\{K_x | x \in \mathbb{R}^d\}$  is total in  $\hat{H}$  ???. Hence, for any  $f, g \in \hat{H}$  we find  $(f_n)_{\mathbb{N}}, (g_m)_{\mathbb{N}} \in H_0, n \in \mathbb{N}$ , such that  $f_n \rightarrow f$  and  $g_m \rightarrow g$  as  $n \rightarrow \infty$ , which implies

$$(f, g)_{\hat{H}} = (f, g)_{H_0}, \quad f, g \in H_0. \quad (2.13)$$

Now since  $H_0 \subseteq \hat{H}$  and (2.13) there holds  $H \subseteq \hat{H}$ . Also by construction of  $H$  we must have  $\hat{H} \subseteq H$  and thus  $H = \hat{H}$ .  $\square$

In our context, the relevant Hilbert space  $V$  of  $\mathbb{R}^3$ -vector fields is often defined as the *self-reproducing Hilbert space*  $V = V_K$  of  $\mathbb{R}^3$ -vector fields defined by a smooth symmetric bounded positive definite kernel  $K$  on  $\mathbb{R}^3 \times \mathbb{R}^3$ , where  $K$  is assumed to be bounded, smooth, and invariant under translations.

For many shape matching applications,  $K$  can be the *radial Gaussian kernel*  $K_\sigma$

$$K_\sigma(x, x') = \frac{1}{(2\pi)^{3/2}\sigma^3} \exp\left(-\frac{\|x - x'\|^2}{\sigma^2}\right) \quad (2.14)$$

with a suitable *scale parameter*  $\sigma > 0$ . Note that when  $V = V_{K_\sigma}$ , the Sobolev embedding hypothesis above is satisfied for any  $s > 5/2$ . The choice  $V = V_{K_\sigma}$  seems to be a good pragmatic choice for diffeomorphic shape matching applications as seen in previous studies[36].

### 2.2.3 Distance between Shapes

To compare two shapes  $S$  and  $S'$  with boundary, regularly embedded in  $\mathbb{R}^3$  we define smooth non-negative geometric distances  $D(S, S')$  quantifying the geometric disparity between the two. The classical Hausdorff disparities  $h(S, S')$  and  $h(S', S)$  between subsets  $S, S'$  of  $\mathbb{R}^3$  are defined by

$$h(S, S') = \max_{x \in S} \left( \min_{x' \in S'} |x - x'| \right).$$

They determine the *Hausdorff distance*  $D_h$  by

$$D_h(S, S') = \max(h(S, S'), h(S', S)). \quad (2.15)$$

Hausdorff distances introduce theoretical complications in the variational framework below, since  $D_h(S, S')$  is not always smooth with respect to small perturbations of  $S$

or of  $S'$ , but Hausdorff disparities are nevertheless quite useful in numerical schemes as will be clarified later in chapter 6. For many shape matching applications, one can identify as in [31], each submanifold  $S$  regularly embedded in  $\mathbb{R}^3$ , with the measure  $\mu_S \in \text{BM3}$  induced on  $S$  by the Lebesgue measure of  $\mathbb{R}^3$ . Here,  $\text{BM3}$  is the space of bounded Borel measures  $m, m'$  on  $\mathbb{R}^3$ , endowed with the Hilbert norm  $\|m\|_\Gamma$  associated with the scalar product

$$\langle m, m' \rangle_\Gamma = \int_{\mathbb{R}^3} \int_{\mathbb{R}^3} \Gamma(x, x') dm(x) dm'(x'), \quad (2.16)$$

where  $\Gamma$  is any smooth, symmetric, translation invariant, and bounded *positive definite kernel* on  $\mathbb{R}^3 \times \mathbb{R}^3$ , such as the often used *radial Gaussian kernel*  $K_\sigma$ . The corresponding distance between two bounded Borel subsets  $S, S'$  of  $\mathbb{R}^3$  is then defined by

$$D_\Gamma^2(S, S') = \|\mu_S - \mu_{S'}\|_\Gamma^2 \quad (2.17)$$

and has nice smoothness properties.

Denote by  $\text{Diff}(\mathbb{R}^3)$  the space of all  $\mathbb{R}^3$ -diffeomorphisms endowed with the topology of uniform convergence on bounded subsets of  $\mathbb{R}^3$ . Then for any fixed pair  $S, S'$  of bounded submanifolds regularly embedded in  $\mathbb{R}^3$ , the distance  $D_\Gamma(G(S), S')$  is a continuous function of  $G \in \text{Diff}(\mathbb{R}^3)$  (see [31]).

## 2.3 Variational Formulation in Context of Multiple Snapshots

We now present the variational formulation for diffeomorphic matching of intermediary snapshots. Consider a given sequence of  $q + 1$  instantaneous 'snapshots'  $S_j = S_{t_j} \subset \mathbb{R}^3$  generated at fixed intermediary times  $t_j, 0 \leq j \leq q$ , by a deformable shape  $S_t$  with unknown dynamics. Each  $S_j$  is typically a bounded piecewise smooth submanifold with boundary, regularly embedded in  $\mathbb{R}^3$ . We seek a vector field flow  $v = (v_t)$  on  $\mathbb{R}^3$  belonging to the Hilbert space  $L^2(I, V), I := [t_0, t_q]$  such that for  $j = 1, \dots, q$ , the  $\mathbb{R}^3$ -diffeomorphism  $F_t$  solution of (2.4a),(2.4b) deforms the initial snapshot  $S_0$  into a submanifold  $\hat{S}_j = F_{t_j}(S_0)$  'coinciding' as well as possible with the given snapshot  $S_j$ . We select a disparity functional  $D^2(S, S')$  such as one of the functionals introduced earlier, and quantify the constraint matching adequacy of  $v$  by the  $q$  numerical disparities

$$\text{Disp}_j(v) = D^2(\hat{S}_j, S_j) \quad , \quad j = 1, \dots, q.$$

We fix  $q$  positive numerical weights  $\lambda_j > 0$ , and we define the *disparity cost functional* by

$$\text{Disp}(v) := \sum_{j=1}^q \lambda_j \text{Disp}_j(v). \quad (2.18)$$

These disparity functionals actually belong to a much wider class of functionals  $\mathcal{D}(V)$  which we now introduce.

For  $v \in L^2(I, V)$  we denote by  $F_t^v \in \text{Diff}(\mathbb{R}^3)$  the solution of (2.4a),(2.4b) determined by  $v$ . We define  $\mathcal{D}(V)$  as the space of all disparity functionals  $\text{Disp} : L^2(I, V) \rightarrow \mathbb{R}_+$

### 2.3. VARIATIONAL FORMULATION IN CONTEXT OF MULTIPLE SNAPSHOTS

---

which are of the form

$$\text{Disp}(v) = \phi(F_{t_1}^v, \dots, F_{t_q}^v) \quad (2.19)$$

for some fixed, but arbitrary choices of the integer  $q$ , of the instants  $t_1, \dots, t_q$  in  $\mathbb{R}_+$ , and of the continuous function  $\phi : (\text{Diff}(\mathbb{R}^3))^q \rightarrow \mathbb{R}_+$ .

We define the objective functional  $J : L^2(I, V) \rightarrow \mathbb{R}$  by

$$J(v) := E(v) + \text{Disp}(v) \quad , \quad v \in L^2(I, V), \quad (2.20)$$

where  $E(v)$  is the kinetic energy as given by (2.3) and  $\text{Disp}(v)$  is as in 2.19. We consider the minimization problem

$$\inf_{v \in L^2(I, V)} J(v). \quad (2.21)$$

## CHAPTER 3

---

### Existence of a Solution of the Variational Problem.

#### Necessary Optimality Conditions

---

In order to show the existence of a solution to the variational problem 2.20 formulated in Chapter 2, we use standard techniques from calculus of variations. The subtle part of the proof lies in establishing that a sequence of diffeomorphic flows obtained by solving (2.4) associated with a weakly converging bounded sequence of vector field flows, is uniformly convergent on bounded subsets of  $\mathbb{R}^3$ . Further, in section 3.2 we obtain the Gâteaux derivative of the functional  $J$  in terms of vector valued Borel measures, and derive necessary optimality conditions for the optimal control problem

in term of the Gâteaux derivative.

### 3.1 Existence of the Variational Problem

**Theorem 3.1.** *Under the assumption that  $V$  is continuously embedded in  $W^{s,2}(\mathbb{R}^3)^3$ , the optimization problem given below has a solution.*

$$\inf_{v \in L^2(I, V)} J(v) = E(v) + \text{Disp}(v) \quad ,$$

where  $E(v) = \frac{1}{2} \|v\|_{L^2(I, V)}^2$  is the kinetic energy as explained in (2.3) and  $\text{Disp}(v) = \phi(F_{t_1}^v, \dots, F_{t_q}^v)$  as in 2.19 such that  $\phi : (\text{Diff}(\mathbb{R}^3))^q \rightarrow \mathbb{R}_+$  is a continuous function where  $F_t^v$  is solution of the following ODE.

$$\partial_t F_t = v_t(F_t) \quad , \quad t \in I,$$

$$F_0 = \text{Id}.$$

*Proof.* Let  $\{v^n\}_{\mathbb{N}}, v^n \in L^2(I, V), n \in \mathbb{N}$ , be a minimizing sequence, i.e.,

$$J(v^n) \rightarrow \inf_{v \in L^2(I, V)} J(v) \quad (n \rightarrow \infty). \quad (3.1)$$

Obviously, this sequence is bounded in  $L^2(I, V)$  and hence is weakly compact. Consequently, we find  $v^* \in L^2(I, V)$  and a subsequence (still indexed by  $\mathbb{N}$ ) converging weakly to  $v^*$  in  $L^2(I, V)$ . This implies

$$\liminf_{n \rightarrow \infty} \|v^n\|_{L^2(I, V)}^2 \geq \|v^*\|_{L^2(I, V)}^2. \quad (3.2)$$

### 3.1. EXISTENCE OF THE VARIATIONAL PROBLEM

---

We denote by  $F_t^n$  and  $F_t^*$  the unique flows of  $\mathbb{R}^3$ -diffeomorphisms solving (2.4a),(2.4b) with respect to the vector field flows  $v^n$  and  $v^*$ , respectively. The main part of the proof will be to verify the following key convergence result

$$F_t^*(x) = \lim_{n \rightarrow \infty} F_t^n(x) \quad \forall t \in I, x \in \mathbb{R}^3, \quad (3.3)$$

where, for each fixed  $t \in I$ , the convergence in (3.3) is uniform in  $x$  on bounded subsets  $B$  of  $\mathbb{R}^3$ . If we assume that (3.3) holds true, then  $F_{t_j}^n \rightarrow F_{t_j}^*$ ,  $0 \leq j \leq q$ , in  $C(\mathbb{R}^3, \mathbb{R}^3)$  as  $n \rightarrow \infty$  and hence, the continuity hypothesis on the disparity functional implies

$$\text{Disp}(v^*) = \lim_{n \rightarrow \infty} \text{Disp}(v^n). \quad (3.4)$$

In view of (3.3), (3.2) and (3.4), we obtain

$$\inf_{v \in L^2(I, V)} J(v) \geq \liminf_{n \rightarrow \infty} J(v^n) = \liminf_{n \rightarrow \infty} E(v^n) + \lim_{n \rightarrow \infty} \text{Disp}(v^n) \geq E(v^*) + \text{Disp}(v^*) = J(v^*),$$

which implies

$$J(v^*) = \inf_{v \in L^2(I, V)} J(v),$$

i.e.,  $v^*$  is a minimizer of  $J$ .

We now prove the key point (3.3). Let  $B$  be a fixed, but arbitrary bounded subset of  $\mathbb{R}^3$ . Since  $V$  is continuously embedded in the Banach space of bounded continuous vector fields, we have

$$\|v_t(x)\|_{\mathbb{R}^3} \leq \sup_{x \in \mathbb{R}^3} \|v_t(x)\|_{\mathbb{R}^3} = \|v_t\|_{C(\mathbb{R}^3)} \leq C \|v_t\|_V \quad \forall x \in \mathbb{R}^3, t \in I, v \in V. \quad (3.5)$$

Then, the equations (2.4a),(2.4b) imply that for all  $(t, x) \in I \times B$  and all  $n \in \mathbb{N}$

### 3.1. EXISTENCE OF THE VARIATIONAL PROBLEM

---

there holds

$$\begin{aligned} \|F_t^n(x)\|_{\mathbb{R}^3} &\leq \|x\|_{\mathbb{R}^3} + \int_0^t |v_t^n(F_t^n(x))|_{\mathbb{R}^3} dt \leq \|x\|_{\mathbb{R}^3} + C \int_0^t \|v_t^n\|_V dt \\ &\leq \|x\|_{\mathbb{R}^3} + C(t-t_0)^{\frac{1}{2}} \int_0^t \|v_t^n\|_V^2 dt \leq \|x\|_{\mathbb{R}^3} + C\|v^n\|_{L^2(I,V)} \leq C_B. \end{aligned} \quad (3.6)$$

Moreover, for all  $a, b \in I$  and  $x \in \mathbb{R}^3$  we have

$$\begin{aligned} |F_a^n(x) - F_b^n(x)| &= \left| \int_a^b v_t^n(F_t^n(x)) dt \right| \leq \int_a^b \|v_t^n(F_t^n(x))\|_{\mathbb{R}^3} dt \\ &\leq C \int_a^b \|v_t^n\|_V dt \leq C(b-a)^{1/2} \|v^n\|_{L^2(I,V)} \leq C(b-a)^{1/2}. \end{aligned} \quad (3.7)$$

Due to the continuous embedding of  $V$  into  $W^{s,2}(\mathbb{R}^3)^3$ ,  $s > 5/2$ ,  $v$  is a continuously differentiable function. Hence  $v$  will satisfy Lipschitz condition, cf. Chapter 4 of [5].

$$\|v_t(x) - v_t(y)\| \leq ct \|v_t\|_V \|x - y\| \quad \forall x, y \in \mathbb{R}^3, \quad t \in I, \quad v \in L^2(I, V) \quad (3.8)$$

The inequalities (3.7) and (3.8) imply equicontinuity of the functions

$$(t, x) \in I \times \mathbb{R}^3 \rightarrow F_t^n(x).$$

Moreover, for  $(t, x) \in I \times B$ , the sequence of  $\mathbb{R}^3$ -norms  $\|F_t^n(x)\|$  is bounded. By Ascoli's theorem, after extraction of a subsequence (for ease of notation still denoted  $\{v^n\}_{\mathbb{N}}$ ), we may assume that the sequence  $\{F_t^n(x)\}_{\mathbb{N}}$  converges uniformly for  $(t, x) \in I \times B$  to some continuous function  $(t, x) \rightarrow u_t(x) \in \mathbb{R}^3$ . Applying this result to a sequence of balls  $B \subset \mathbb{R}^3$  with fixed center and radii tending to infinity, and selecting a 'diagonal' subsequence of  $\{v^n\}_{\mathbb{N}}$ , we deduce the existence of a minimizing sequence

### 3.1. EXISTENCE OF THE VARIATIONAL PROBLEM

---

(still denoted  $\{v^n\}_{\mathbb{N}}$ ) and of a continuous function  $(t, x) \rightarrow z_t^*(x) \in \mathbb{R}^3$  such that

$$z_t^*(x) = \lim_{n \rightarrow \infty} F_t^n(x) \quad \text{uniformly for } (t, x) \text{ in bounded subsets of } I \times \mathbb{R}^3. \quad (3.9)$$

We fix a bounded set  $B \subset \mathbb{R}^3$  and some  $\varepsilon > 0$ . Then, there exists  $n_1 \in \mathbb{N}$  such that for  $n > n_1$

$$\|F_t^n(x) - z_t^*(x)\| \leq \varepsilon \quad \forall (t, x) \in I \times B.$$

We choose  $\delta > 0$  small enough such that the continuous function  $z^* : (t, x) \rightarrow z_t^*(x)$  has oscillations less than  $\varepsilon$  on any rectangular box in  $I \times B$  with diameter less than  $\delta$ . We further consider a covering of the bounded set  $B \subset \mathbb{R}^3$  by a finite family  $\Omega$  of disjoint rectangular boxes  $\omega \in \Omega$  and a finite partition  $\Theta$  of the interval  $I$  into subintervals  $T \in \Theta$  such that all rectangular boxes  $T \times \omega$  have diameters less than  $\delta$ . Clearly, we can then select a function

$$Z : (t, x) \in I \times \mathbb{R}^3 \rightarrow Z_t(x) \in \mathbb{R}^3,$$

which satisfies  $Z_t(x)$  constant on each  $T \times \omega$  with  $T \in \Theta, \omega \in \Omega$ , and such that

$$\|Z_t(x) - z_t^*(x)\| < \varepsilon \quad \forall (t, x) \in I \times B. \quad (3.10)$$

For  $a, b \in I$  and  $x \in B$  we want to estimate the integral

$$\int_a^b \left( v_t^n(F_t^n(x)) - v_t^*(z_t^*(x)) \right) dt, \quad (3.11)$$

where the integrand  $U := v_t^n(F_t^n(x)) - v_t^*(z_t^*(x))$  can be split according to

$$U = U_1 + U_2 + U_3 + U_4 \quad (3.12)$$

### 3.1. EXISTENCE OF THE VARIATIONAL PROBLEM

---

with

$$\begin{aligned} U_1 &= v_t^n(F_t^n(x)) - v_t^n(z_t^*(x)) \quad , \quad U_2 = v_t^n(z_t^*(x)) - v_t^n(Z_t(x)), \\ U_3 &= v_t^*(Z_t(x)) - v_t^*(z_t^*(x)) \quad , \quad U_4 = v_t^n(Z_t(x)) - v_t^*(Z_t(x)). \end{aligned}$$

For any two functions  $f_t(x)$  and  $g_t(x)$  that are continuous on  $I \times B$  with values in  $\mathbb{R}^3$  and satisfy

$$\|f_t(x) - g_t(x)\|_{\mathbb{R}^3} \leq \varepsilon \quad \forall (t, x) \in I \times B,$$

we have the bound

$$\|v_t(f_t(x)) - v_t(g_t(x))\|_{\mathbb{R}^3} \leq C \varepsilon \|v_t\|_V \quad \forall t \in I, \quad x \in B, v \in L^2(I, V).$$

This implies that for all  $a, b \in I$ ,  $x \in B$  there holds

$$\left| \int_a^b (v_t(f_t(x)) - v_t(g_t(x))) dt \right| \leq C \varepsilon \int_a^b \|v_t\|_V dt \leq C \varepsilon \|v\|_{L^2(I, V)}.$$

Applying the preceding argument separately to  $U_1, U_2, U_3$ , we find that for all  $a, b \in I$ ,  $x \in B$ , and all  $n > n_1$  we have

$$\int_a^b [ |U_1| + |U_2| + |U_3| ] dt \leq C \varepsilon \left( 2\|v^n\|_{L^2(I, V)} + \|v^*\|_{L^2(I, V)} \right) \leq C \varepsilon. \quad (3.13)$$

Since the Hilbert space  $V$  is continuously embedded in  $W^{s,2}(\mathbb{R}^3)^3$ ,  $s > 5/2$ , for each  $y \in \mathbb{R}^3$  there exists a function  $\ker^y \in V$  generating the evaluation map on  $V$  by means of

$$w(y) = \langle \ker^y, w \rangle, \quad \forall w \in V.$$

### 3.1. EXISTENCE OF THE VARIATIONAL PROBLEM

---

Now, for each  $y \in \mathbb{R}^3$  and each pair  $a, b \in I$  we define a function

$$\text{KER} : t \rightarrow \text{KER}_t = 1_{[a,b]}(t) \ker^y.$$

Clearly,  $\text{KER} \in L^2(I, V)$  and we have

$$\int_{[a,b]} v_t(y) dt = \int_I \langle \text{KER}, v_t \rangle_V dt = \langle \text{KER}, v \rangle_V \quad \forall v \in L^2(I, V), y \in \mathbb{R}^3.$$

Since  $v^n - v^* \rightarrow 0$  in  $L^2(I, V)$ , the last equality shows that for each fixed  $y \in \mathbb{R}^3$  and each pair  $a, b \in I$  we have

$$\lim_{n \rightarrow \infty} \left( \int_{[a,b]} (v_t^n(y) - v_t^*(y)) dt \right) = 0. \quad (3.14)$$

For each pair  $(T, \omega) \in \Theta \times \Omega$  there is a fixed vector  $y(T, \omega) \in \mathbb{R}^3$  such that  $Z_t(x) = y(T, \omega)$  for all  $(t, x) \in T \times \omega$ . Fixing  $\omega \in \Omega$ , for all  $x \in \omega$  we have

$$\begin{aligned} \int_a^b U_4 dt &= \sum_{T \in \Theta} \int_{T \cap [a,b]} \left( v_t^n(Z_t(x)) - v_t^*(Z_t(x)) \right) dt \\ &= \sum_{T \in \Theta} \int_{T \cap [a,b]} \left( v_t^n(y(T, \omega)) - v_t^*(y(T, \omega)) \right) dt. \end{aligned} \quad (3.15)$$

In view of (3.14), we see that each term on the right-hand side of (3.15) tends to 0 as  $n \rightarrow \infty$  uniformly for  $x \in \omega$ . Since the partition  $\Theta$  is finite and fixed, we deduce

$$\lim_{n \rightarrow \infty} \left[ \int_a^b U_4 dt \right] = 0 \quad (3.16)$$

uniformly for  $x \in \omega$ , and hence also uniformly for  $x \in B$ , since the partition  $\Omega$  is finite and fixed. Consequently, for given  $a, b \in I$  and all  $x \in B$  we can find  $n_2 > n_1$  such that for  $n > n_2$  there holds

$$\left| \int_a^b U_4 dt \right| \leq \varepsilon. \quad (3.17)$$

### 3.2. NECESSARY OPTIMALITY CONDITIONS

---

Combining (3.17) with (3.12) and (3.13), we conclude that for any given  $a, b \in I$  and uniformly for all  $x \in B$  there holds

$$\lim_{n \rightarrow \infty} \left( \int_a^b \left( v_t^n(F_t^n(x)) - v_t^*(z^*(t, x)) \right) dt \right) = 0. \quad (3.18)$$

The equations (2.4a),(2.4b) for  $F_t^n(x)$  imply

$$F_t^n(x) = x + \int_{t_0}^t \left( v_t^n(F_t^n(x)) \right) \quad \forall t \in I, x \in \mathbb{R}^3.$$

Hence, the two limits (3.9) and (3.18) show that

$$z^*(t, x) = x + \int_{t_0}^t \left( v_t^*(z^*(t, x)) \right) \quad \forall t \in I, x \in \mathbb{R}^3.$$

In view of Theorem 2.1, we see that  $z^*$  must coincide with the unique solution  $F^*$  of (2.4a),(2.4b) determined by  $v^*$ . This proves the key convergence result (3.3).  $\square$

## 3.2 Necessary Optimality Conditions

We now derive first order necessary optimality conditions in terms of the Gâteaux derivative of the objective functional  $J$ . Denote by  $\text{CR3} = C(\mathbb{R}^3, \mathbb{R}^3)$  the vector space of continuous maps from  $\mathbb{R}^3$  to  $\mathbb{R}^3$  endowed with the topology of uniform convergence on bounded subsets of  $\mathbb{R}^3$ . Call  $\text{MR3}$  the dual of  $\text{CR3}$ , i.e the space of all linear continuous maps  $\Lambda : \text{CR3} \rightarrow \mathbb{R}$  which are of the form

$$\Lambda(g) = \int_{\mathbb{R}^3} \langle \lambda(x), g(x) \rangle_{\mathbb{R}^3} d\theta(x) \quad \forall g \in \text{CR3}, \quad (3.19)$$

### 3.2. NECESSARY OPTIMALITY CONDITIONS

---

where  $\theta$  is any positive bounded Borel measure on  $\mathbb{R}^3$  and  $\lambda : \mathbb{R}^3 \rightarrow \mathbb{R}^3$  is any Borel function with compact support such that

$$\int_{\mathbb{R}^3} \|\lambda(x)\|_{\mathbb{R}^3} d\theta(x) < \infty. \quad (3.20)$$

We introduce  $\text{Gat}(V, 3)$  as the space of all functions  $v \rightarrow G^v$  from  $L^2(I, V)$  into CR3 having a Gâteaux derivative  $\nabla G^v$  at each  $v \in L^2(I, V)$ . The operators  $\nabla G^v$  are linear maps from  $L^2(I, V)$  to  $C(\mathbb{R}^3, \mathbb{R}^3)$  of the form

$$\nabla G^v . w = \lim_{\varepsilon \rightarrow 0} (1/\varepsilon) (G^{v+\varepsilon w} - G^v) \quad \forall w \in L^2(I, V). \quad (3.21)$$

We say that a functional  $\phi : (\text{CR3})^q \rightarrow \mathbb{R}$ ,  $\phi$  has weak partial derivatives  $\partial_j \phi(Z) \in \text{MR3}$  at  $Z \in (\text{CR3})^q$ , if for any set of  $q$  functions  $G_j \in \text{Gat}(V, 3)$  the composite function  $f(v) = \phi(G_1^v, \dots, G_q^v)$  has a Gâteaux derivative  $\nabla f(v)$  at each  $v \in L^2(I, V)$ , and the derivative in the direction  $w \in L^2(I, V)$  is given by

$$\nabla f(v) . w = \sum_{j=1}^q \partial_j \phi(Z) . [\nabla_v G_j . w] \quad \forall w \in L^2(I, V), \quad (3.22)$$

where  $Z = (G_1^v, \dots, G_q^v)$ .

**Theorem 3.2.** *Let  $J$  be the objective functional as given by (2.20) with a disparity functional of the form  $\text{Disp}(v) = \phi(F_{t_1}^v, \dots, F_{t_q}^v)$ , where  $\phi : (C(\mathbb{R}^3), \mathbb{R}^3)^q \rightarrow \mathbb{R}^3$  has Gâteaux partial derivatives  $\partial_j \phi$ . Assume that for all  $g \in \text{CR3}$*

$$\partial_j \phi . g = \int_{\mathbb{R}^3} \langle \lambda_j(x), g(x) \rangle_{\mathbb{R}^3} d\theta_j(x), \quad (3.23)$$

where  $\theta_j, 1 \leq j \leq q$ , are positive bounded Borel measures with compact support in  $\mathbb{R}^3$  and the  $\lambda_j : \mathbb{R}^3 \rightarrow \mathbb{R}^3, 1 \leq j \leq q$ , are continuous functions. Then, the Gâteaux

### 3.2. NECESSARY OPTIMALITY CONDITIONS

---

derivative  $\nabla J(v) \in L^2(I, V)$  is given by

$$\nabla J(v).w = \int_{t_0}^{t_q} \left( \int_{\mathbb{R}^3} w_t d(\rho_{t,v} + \eta_{t,v}) \right) dt, \quad (3.24)$$

where for each  $t$  and  $v$  the quantities  $\rho_{t,v}$  and  $\eta_{t,v}$  are  $\mathbb{R}^3$ -vector valued Borel measures on  $\mathbb{R}^3$ , and the measures  $\eta_{t,v}$  remain constant in  $t$  over each interval  $[t_j, t_{j+1})$ . Explicit formulas for these measures are given below in the proof of this theorem.

If  $v^* \in L^2(I, V)$  is a minimizing diffeomorphic flow, then  $\nabla J(v^*) = 0$ , and this implies  $\rho_{t,v^*} + \eta_{t,v^*} = 0$  for all  $t \in I$ .

*Proof.* Obviously, the Gâteaux derivative  $\nabla E(v)$  of the kinetic energy is given by

$$\nabla E(v).w = \langle v, w \rangle_{L^2(I, V)}. \quad (3.25)$$

We fix  $v \in L^2(I, V)$  and  $x \in \mathbb{R}^3$  and denote by  $DF_t^v(x) : \mathbb{R}^3 \rightarrow \mathbb{R}^3$  the Jacobian  $m$  of the diffeomorphism  $F_t^v$  at  $x$ . Since

$$\partial_t F_t^v(x) = v_t(F_t^v(x)) \quad \text{and} \quad F_0^v(x) = x,$$

the Gâteaux derivative

$$g_t = g_t(x, v, w) = \nabla_v F_t^v(x)$$

of  $F_t^v(x)$  with respect to  $v$  in the direction  $w \in L^2(I, V)$  will be

$$g_t(x, v, w) = \lim_{\varepsilon \rightarrow 0} \frac{F_t^{v+\varepsilon w}(x) - F_t^v(x)}{\varepsilon}. \quad (3.26)$$

### 3.2. NECESSARY OPTIMALITY CONDITIONS

---

Which implies

$$\begin{aligned}
 \partial_t g_t(x, v, w) &= \lim_{\varepsilon \rightarrow 0} \frac{\partial_t F_t^{v+\varepsilon w}(x) - \partial_t F_t^v(x)}{\varepsilon} \\
 &= \lim_{\varepsilon \rightarrow 0} \frac{(v + \varepsilon w_t)(F_t^{v+\varepsilon w}) - v_t(F_t^v(x))}{\varepsilon} \\
 &= \lim_{\varepsilon \rightarrow 0} \frac{v(F_t^{v+\varepsilon w}) - v_t(F_t^v(x))}{\varepsilon} + \lim_{\varepsilon \rightarrow 0} w_t(F_t^{v+\varepsilon w}) \\
 &= Dv_t(F_t^v(x)).g_t + w_t(F_t^v). \quad (3.27)
 \end{aligned}$$

Hence  $g_t$  satisfies

$$\partial_t g_t - Dv_t(F_t^v(x)).g_t = w_t(F_t^v(x)),$$

$$g_0 = 0,$$

so that  $g_t$  is the solution of an initial-value problem for a linear ordinary differential equation with non-zero right-hand side  $r_t = r_t(x, v, w) = w_t(F_t^v(x))$ . Setting  $p_t = p_t(x, v) = Dv_t(F_t^v(x))$ , this initial-value problem can be written as

$$\partial_t g_t = p_t.g_t + m_t, \quad (3.28a)$$

$$g_0 = 0. \quad (3.28b)$$

We denote by  $R_{s,t}, t_0 < s < t < t_q$  the resolvent of the homogeneous linear ordinary differential equation  $\partial_t z_t = p_t.z_t$  which satisfies

$$\partial_t R_{s,t} = p_t.R_{s,t} \quad \text{and} \quad R_{s,s} = \text{Id} \quad \forall s < t.$$

We note that  $R_{s,t}$  depends only on  $s, t, x, v$  and that the solution  $g_t$  of (3.28a),(3.28b) is then given by

$$g_t = \int_{t_0}^t R_{s,t}.m_s \, ds.$$

### 3.2. NECESSARY OPTIMALITY CONDITIONS

---

With a slight change of notations, omitting the explicit dependence on  $x \in \mathbb{R}^3$ , this results in

$$\nabla_v F_t^v \cdot w = \int_{t_0}^t R_{s,t}^v \cdot w_s(F_s^v) ds. \quad (3.29)$$

In view of the hypothesis on the functional  $\phi$ , it follows that

$$(\nabla \text{Disp}^v) \cdot w = \sum_{j=1}^q \partial_j \phi \cdot \nabla_v F_{t_j}^v \cdot w,$$

and hence, taking (3.29) into account, we have

$$[\nabla \text{Disp}^v] \cdot w = \sum_{j=1}^q \int_{t_0}^{t_j} [\partial_j \phi \cdot R_{s,t_j}^v \cdot] \cdot [w_s(F_s^v)] ds.$$

For each  $s \in I$  and fixed  $v \in L^2(I, V)$  we define the linear map  $A_s : V \rightarrow \mathbb{R}$  by

$$A_s^v = \sum_{j=1}^q 1_{[t_0, t_j]}(s) \partial_j \phi R_{s,t_j}^v, \quad (3.30)$$

whence

$$[\nabla \text{Disp}^v] \cdot w = \int_{t_0}^{t_q} A_s^v \cdot [w_s(F_s^v)] ds. \quad (3.31)$$

Finally, due to (3.25) we obtain

$$\nabla J(v) \cdot w = \int_{t_0}^{t_q} \left[ \langle v_t, w_t \rangle_V + A_t^v \cdot [w_t(F_t^v)] \right] dt. \quad (3.32)$$

We fix an instant  $s < t_j$  and for  $x \in \mathbb{R}^3$  temporarily define the  $3 \times 3$  matrix  $R(x)$  and the diffeomorphism  $x \rightarrow u(x) \in \mathbb{R}^3$  according to

$$R(x) = R_{s,t_j}^v(x) \quad \text{and} \quad u(x) = F_s^v(x).$$

For the function  $g : x \rightarrow g(x) = R(x)w_s(u(x))$  we thus get

$$\partial_j \phi \cdot [R_{s,t_j}^v \cdot [w_s(F_s^v)]] = \int_{\mathbb{R}^3} \langle \lambda_j(x), R(x)w_s(u(x)) \rangle_{\mathbb{R}^3} d\theta_j(x).$$

### 3.2. NECESSARY OPTIMALITY CONDITIONS

---

We define the bounded measure  $\mu_j = u(\theta_j)$  as the direct image of the measure  $\theta_j$  by the diffeomorphism  $u$  and note that  $\mu_j$  depends only on  $j, s, v$ , which are fixed temporarily. In view of the definition of transported measures, we have

$$\int_{\mathbb{R}^3} \langle \lambda_j(x), R(x)w_s(u(x)) \rangle_{\mathbb{R}^3} d\theta_j(x) = \int_{\mathbb{R}^3} \langle R^T(u^{-1}(y))\lambda_j(u^{-1}(y)), w_s(y) \rangle_{\mathbb{R}^3} d\mu_j(y), \quad (3.33)$$

where  $R^T$  stands for the transpose of the matrix  $R$ .

Now, for  $s < t_j$  we define

$$\begin{aligned} a_{j,s,v}(x) &:= [R_{s,t_j}^v(x)]^T \cdot \lambda_j(x) \quad \forall x \in \mathbb{R}^3, \\ b_{j,s,v}(y) &:= a_{j,s,v} \circ [F_s^v]^{-1}(y), \\ \mu_{j,s,v} &:= F_s^v[\theta_j]. \end{aligned}$$

It follows that

$$A_s^v \cdot [w_s(F_s^v)] = \sum_{j=1}^q 1_{[t_0, t_j]}(s) \int_{\mathbb{R}^3} \langle b_{j,s,v}(y), w_s(y) \rangle_{\mathbb{R}^3} d\mu_{j,s,v}(y).$$

We introduce the vector-valued Borel measure  $\nu_{j,s,v}$ , taking values in  $\mathbb{R}^3$ , as the measure with vector-valued density  $b_{j,s,v}$  with respect to the bounded Borel measure  $\mu_{j,s,v}$ , so that for any continuous function  $g : \mathbb{R}^3 \rightarrow \mathbb{R}^3$  there holds

$$\int_{\mathbb{R}^3} g d\nu_{j,s,v} = \int_{\mathbb{R}^3} \langle b_{j,s,v}(y), w_s(y) \rangle_{\mathbb{R}^3} d\mu_{j,s,v}.$$

We then define the vector-valued measure  $\eta_{s,v}$  on  $\mathbb{R}^3$  by means of

$$\eta_{s,v} = \sum_{j=1}^q 1_{[t_0, t_j]}(s) \nu_{j,s,v},$$

### 3.2. NECESSARY OPTIMALITY CONDITIONS

---

and thus obtain

$$\nabla J(v).w = \int_{t_0}^{t_q} \left( \langle v_t, w_t \rangle_V + \int_{\mathbb{R}^3} w_t d\eta_{t,v} \right) dt. \quad (3.34)$$

On the Hilbert space  $V$ , the norm and the scalar product are defined by the kernel  $K(x, y)$ , whence

$$\langle v_t, w_t \rangle_V = \int_{\mathbb{R}^3} \langle K v_t(x), w_t(x) \rangle_{\mathbb{R}^3} dx = \int_{\mathbb{R}^3} w_t d\rho_{t,v}.$$

Here, the vector-valued measure  $\rho_{t,v}$  has density  $K v_t$  with respect to the Lebesgue measure on  $\mathbb{R}^3$ . Finally, we obtain the following representation which is valid for all  $w \in L^2(I, V)$

$$\nabla J(v).w = \int_{t_0}^{t_q} \left( \int_{\mathbb{R}^3} w_t d(\rho_{t,v} + \eta_{t,v}) \right) dt. \quad (3.35)$$

Let  $v^* \in L^2(I, V)$  be a minimizer of the objective functional  $J$ . Obviously, we must have

$$\nabla J(v^*).w = 0 \quad \forall w \in L^2(I, V). \quad (3.36)$$

In view of (3.35), this forces the measures  $\rho_{t,v} + \eta_{t,v}$  to be zero for all  $t \in I$  except for a possible exceptional set  $\Omega \subset I$  of Lebesgue measure zero. Since the measures  $\eta_{t,v}$  are constant in  $t$  within each interval  $[t_j, t_{j+1})$  and the measures  $\rho_{t,v}$  are continuous in  $t$ , we conclude that  $\Omega$  must be empty.  $\square$

## CHAPTER 4

---

### Dirac Measures and Diffeomorphic Point Matching

---

Diffeomorphic point matching [19, 34, 38] is a particular case of diffeomorphic matching of measures that can be derived from the general framework of Chapter 2. In such a framework, a given sequence of  $q + 1$  instantaneous shape snapshots  $S_j = S_{t_j}$  at fixed time frames  $t_j$ ,  $j = 0, \dots, q$ , is identified by a family of point sets  $X_j = \{x_1^j, \dots, x_{N_j}^j\}$ . Let  $\hat{S}_j = F_{t_j}^v(S_0)$  be a sequence of  $q$  submanifolds generated at instants  $t_j$ ,  $1 \leq j \leq q$ , from the initial snapshot  $S_0$  by a  $\mathbb{R}^3$ -diffeomorphism  $F_t^v$  satisfying (2.4a),(2.4b) with unknown flow dynamics  $v \in L^2(I, V)$ . Let  $\hat{X}_j = F_{t_j}^v(X_0) = \{F_{t_j}^v(x_1^0), \dots, F_{t_j}^v(x_{N_0}^0)\}$  be the sequence of  $q$  point sets generated by  $F_t^v$  at instants  $t_j$ ,  $1 \leq j \leq q$  from the initial point set  $X_0$ . We denote by  $x_n(t) = F_t^v(x_n^0)$ ,

---

$t \in I$ , the corresponding  $N_0$  trajectories emanating from  $x_n^0$ ,  $1 \leq n \leq N_0$ , at  $t = 0$ . Thus we have  $\hat{X}_j = \{x_1(t_j), \dots, x_{N_0}(t_j)\}$ ,  $1 \leq j \leq q$ . It is natural to represent  $S_j$  and  $\hat{S}_j$ ,  $1 \leq j \leq q$ , as weighted sums of Dirac measures  $\delta_{x_m^j}$ ,  $1 \leq m \leq N_j$ , and  $\delta_{x_n(t_j)}$ ,  $1 \leq n \leq N_0$ , associated with the point sets  $X_j$  and  $\hat{X}_j$ . In particular, we assume

$$\mu_{S_j} = \sum_{m=1}^{N_j} b_m^j \delta_{x_m^j}, \quad \mu_{\hat{S}_j} = \sum_{n=1}^{N_0} a_n \delta_{x_n(t_j)}, \quad a_n, b_m^j \in \mathbb{R} \quad , \quad j = 1, \dots, q.$$

It follows that the *disparity cost functional* (2.18) takes the form

$$\text{Disp}(v) = \sum_{j=1}^q \lambda_j D_{K_{\sigma_j}}^2(\hat{S}_j, S_j) = \sum_{j=1}^q \lambda_j \|\mu_{\hat{S}_j} - \mu_{S_j}\|_{K_{\sigma_j}}^2. \quad (4.1)$$

The terms  $\|\mu_{\hat{S}_j} - \mu_{S_j}\|_{K_{\sigma_j}}^2$ ,  $1 \leq j \leq q$ , represent the Borel distances between the shapes  $S_j$  and  $\hat{S}_j$  associated with radial Gaussian kernels  $K_{\sigma_j}$  for suitable scale parameters  $\sigma_j > 0$ . From (2.16) and (2.17), we have

$$\|\mu_{\hat{S}_j} - \mu_{S_j}\|_{K_{\sigma_j}}^2 = \langle \mu_{\hat{S}_j} - \mu_{S_j}, \mu_{\hat{S}_j} - \mu_{S_j} \rangle_{K_{\sigma_j}} = \langle \mu_{\hat{S}_j}, \mu_{\hat{S}_j} \rangle_{K_{\sigma_j}} - 2\langle \mu_{\hat{S}_j}, \mu_{S_j} \rangle_{K_{\sigma_j}} + \langle \mu_{S_j}, \mu_{S_j} \rangle_{K_{\sigma_j}}, \quad (4.2)$$

where

$$\langle \mu_{\hat{S}_j}, \mu_{\hat{S}_j} \rangle_{K_{\sigma_j}} = \int_{\mathbb{R}^3} \int_{\mathbb{R}^3} K_{\sigma_j}(x, x') d\mu_{\hat{S}_j}(x) d\mu_{\hat{S}_j}(x') = \sum_{n=1}^{N_0} \sum_{n'=1}^{N_0} a_n a_{n'} K_{\sigma_j}(x_n(t_j), x_{n'}(t_j)), \quad (4.3a)$$

$$\langle \mu_{\hat{S}_j}, \mu_{S_j} \rangle_{K_{\sigma_j}} = \int_{\mathbb{R}^3} \int_{\mathbb{R}^3} K_{\sigma_j}(x, x') d\mu_{\hat{S}_j}(x) d\mu_{S_j}(x') = \sum_{n=1}^{N_0} \sum_{m=1}^{N_j} a_n b_m^j K_{\sigma_j}(x_n(t_j), x_m^j), \quad (4.3b)$$

$$\langle \mu_{S_j}, \mu_{S_j} \rangle_{K_{\sigma_j}} = \int_{\mathbb{R}^3} \int_{\mathbb{R}^3} K_{\sigma_j}(x, x') d\mu_{S_j}(x) d\mu_{S_j}(x') = \sum_{m=1}^{N_j} \sum_{m'=1}^{N_j} b_m^j b_{m'}^j K_{\sigma_j}(x_m^j, x_{m'}^j). \quad (4.3c)$$

---

Recall that  $x_n(t) = F_t^v(x_n^0)$ ,  $t \in I$ ,  $1 \leq n \leq N_0$ , are the solutions of the ODEs

$$\frac{dx_n(t)}{dt} = v_t(x_n(t)), \quad t \in (0, 1], \quad (4.4a)$$

$$x_n(0) = x_n^0. \quad (4.4b)$$

Thus the trajectories  $x_n(t)$ ,  $1 \leq n \leq N_0$ , and the disparity cost functional  $\text{Disp}(v)$ , are uniquely determined by the values of  $v_t$  taken at  $N_0$  points  $x_n(t)$ . Taking into account that  $V = V_K$  is a RKHS associated to a radial Gaussian kernel  $K = K_{\sigma_0}$ , this allows us to restrict the search for  $v_t \in V$  to the set of linear combination of  $K_{x_n(t)}$ ,  $1 \leq n \leq N_0$ , and thus places us in a finite dimensional situation. We look for the flow  $v_t$  under the form  $v_t = \sum_{n=1}^{N_0} \alpha_n(t) K_{x_n(t)}$ ,  $\alpha_n(t) \in \mathbb{R}^3$ , which may also be written

$$v_t(x) = \sum_{n=1}^{N_0} K_{\sigma_0}(x_n(t), x) \alpha_n(t) \quad , \quad \forall x \in \mathbb{R}^3. \quad (4.5)$$

By the self reproducing property of  $K$ , we have

$$\|v_t\|_V^2 = \sum_{n=1}^{N_0} \sum_{n'=1}^{N_0} K_{\sigma_0}(x_n(t), x_{n'}(t)) \alpha_n^T(t) \alpha_{n'}(t).$$

We introduce the matrix-vector notations:

$$x^{(0)} = (x_1^{(0)}, \dots, x_{N_0}^{(0)})^T \in \mathbb{R}^{N_0 d}, \quad x(t) = (x_1(t), \dots, x_{N_0}(t))^T \in \mathbb{R}^{N_0 d}, \quad t \in I,$$

$$\alpha(t) := (\alpha_1(t), \dots, \alpha_{N_0}(t))^T \in \mathbb{R}^{N_0 d}, \quad t \in I,$$

$$A(x(t)) = (A_{nn'}(x(t)))_{n,n'=1}^{N_0} \in \mathbb{R}^{N_0 d \times N_0 d}, \quad A_{nn'}(x(t)) := K_{\sigma_0}(x_n(t), x_{n'}(t)) I_d \in \mathbb{R}^{d \times d}.$$

It follows that the kinetic energy  $E(v)$  defined by (2.3) takes the form

$$E(v) = \frac{1}{2} \int_0^1 \alpha(t)^T A(x(t)) \alpha(t) dt. \quad (4.6)$$

---

Hence, in terms of  $\alpha \in L^2(I, \mathbb{R}^{N_0d})$ , the objective functional reads

$$J(\alpha) = \frac{1}{2} \int_0^1 \alpha(t)^T A(x(t)) \alpha(t) dt + \sum_{j=1}^q \lambda_j \text{Disp}_j(x(t_j)) \quad (4.7)$$

where the  $q$  disparity functions  $\text{Disp}_j(x(t_j)) = \|\mu_{\hat{S}_j} - \mu_{S_j}\|_{K_{\sigma_j}}^2$ ,  $1 \leq j \leq q$  are given by the right-hand sides in (4.2) and (4.3). The diffeomorphic point matching amounts to the solution of the optimal control problem

$$\inf_{\alpha \in L^2(I, \mathbb{R}^{N_0d})} J(\alpha), \quad (4.8a)$$

subject to

$$\frac{dx(t)}{dt} = A(x(t)) \alpha(t), \quad t \in (0, 1], \quad (4.8b)$$

$$x(0) = x^{(0)}. \quad (4.8c)$$

The existence of a solution  $\alpha^*$  of (4.8a)-(4.8c) follows from Theorem 3.1, whereas the first order necessary optimality conditions can be either derived from Theorem 3.2 by evaluating the terms in (3.24) within the current setting (cf., e.g., [31]) or directly as will be shown in the proof of the following result.

**Theorem 4.1.** *Assume that  $\alpha^*(\cdot)$  is the solution of the optimal control problem (4.8), and that  $x^*(\cdot)$  is the corresponding trajectory. Then there exists a function  $p^*(\cdot)$ , called the adjoint state, such that the triple  $(x^*, p^*, \alpha^*)$  satisfies*

$$\frac{dx^*(t)}{dt} = A(x^*(t)) \alpha^*(t), \quad t \in (0, 1], \quad (4.9a)$$

$$x^*(0) = x^{(0)}, \quad (4.9b)$$

---


$$-\frac{dp^*(t)}{dt} = B(x^*(t), \alpha^*(t))^T \left( p^*(t) + \frac{1}{2} \alpha^*(t) \right), \quad t \in (t_{j-1}, t_j), \quad (4.10a)$$

$$p^*(t_q^+) = 0, \quad p^*(t_j^-) = p^*(t_j^+) + \lambda_j \nabla \text{Disp}_j(x^*(t_j)), \quad j = q, \dots, 1, \quad (4.10b)$$

$$A(x^*(t))(\alpha^*(t) + p^*(t)) = 0, \quad t \in (0, 1]. \quad (4.11)$$

In the adjoint state equation (4.10a), the matrix

$$B(x^*(t), \alpha^*(t)) = \nabla_x (A(x^*(t)) \alpha^*(t)),$$

is given by

$$B(x^*(t), \alpha^*(t)) = B_{nm}(x^*(t), \alpha^*(t))_{n,m=1}^{N_0} \in \mathbb{R}^{N_0 d \times N_0 d},$$

$$B_{nm}(x^*(t), \alpha^*(t)) := \alpha_m^*(t) (\nabla_2 K_{\sigma_0}(x_n^*(t), x_m^*(t)))^T + \delta_{nm} \sum_{k=1}^N \alpha_k^*(t) (\nabla_1 K_{\sigma_0}(x_n^*(t), x_k^*(t)))^T,$$

where  $\nabla_x$  denotes the gradient with respect the argument  $x(t)$  and  $\nabla_i K_{\sigma_0}(\cdot, \cdot), 1 \leq i \leq 2$ , stands for the gradient with respect to the  $i$ -th argument of  $K_{\sigma_0}(\cdot, \cdot)$ .

Moreover, (7.6b) represents the jump discontinuities of  $p^*(\cdot)$  at times  $t_j, 1 \leq j \leq q$ .

**Proof.** Introducing Lagrange multipliers  $p(t) = (p_1(t), \dots, p_{N_0}(t))^T \in \mathbb{R}^{N_0 d}, t \in I$ , the Lagrangian associated with (4.8a)-(4.8c) is given by

$$\begin{aligned} L(\alpha, x, p) &:= J(\alpha) - \int_0^1 p \cdot \left( \frac{dx}{dt} - A(x(t))\alpha(t) \right) dt \\ &= - \int_0^1 p \cdot \frac{dx}{dt} dt + \int_0^1 (p + \alpha/2) \cdot A(t, x)\alpha dt + \sum_{j=1}^q \lambda_j \text{Disp}_j(x(t_j)). \end{aligned}$$

---

The optimality conditions for a critical point  $(\alpha^*, x^*, p^*)$  of  $L(\alpha, x, p)$  read as follows:

$$L_\alpha(\alpha^*, x^*, p^*) = 0, \quad (4.12a)$$

$$L_x(\alpha^*, x^*, p^*) = 0, \quad (4.12b)$$

$$L_p(\alpha^*, x^*, p^*) = 0. \quad (4.12c)$$

Obviously, (4.12a) implies (4.11), whereas (4.12c) gives rise to (4.9). Using integration by parts

$$\begin{aligned} - \int_0^1 p \cdot \frac{dx}{dt} dt &= - \sum_{j=1}^q \int_{t_{j-1}}^{t_j} p \cdot \frac{dx}{dt} dt = \sum_{j=1}^q \left( \int_{t_{j-1}}^{t_j} \frac{dp}{dt} \cdot x dt - p(t_j^-) \cdot x(t_j) + p(t_{j-1}^+) \cdot x(t_{j-1}) \right) \\ &= \int_0^1 \frac{dp}{dt} \cdot x dt + \sum_{j=1}^{q-1} (-p(t_j^-) + p(t_j^+)) \cdot x(t_j) - p(1) \cdot x(1) + p(0) \cdot x(0), \end{aligned}$$

(4.12a) yields (4.10).

## CHAPTER 5

---

### The Fully Discrete Optimal Control Problem

---

In this chapter, we outline the basic matching algorithm based on gradient descent and time discretizations of the optimality conditions (7.5a),(4.9b) and (4.10a),(7.6b) as well as variants involving iteration-dependent weighting parameters for the matching term in the objective functional. We will also summarize several initialization schemes.

For the time discretizations of the optimal control problem (4.8) we introduce a partition  $\Delta_I$  of  $I$  according to

$$\Delta_I := \cup_{j=1}^q \Delta_{I_j}, \quad \Delta_{I_j} := \{t_{j-1} =: t^{L_{j-1}} < t^{L_{j-1}+1} < \dots < t^{L_j-1} < t^{L_j} := t_j\}, \quad (5.1)$$

---

where  $\Delta_{I_j}$ ,  $1 \leq j \leq q$ , are subpartitions of intervals  $I_j = [t_{j-1}, t_j]$  whose endpoints  $t_j$  are key time frames at which the shape snapshots  $S_j = S(t_j)$  are given. We set  $L_0 := 0$  and  $L := L_q$  and define step sizes  $\Delta t^\ell := t_{\ell+1} - t_\ell > 0$ ,  $0 \leq \ell \leq L - 1$ .

We introduce the discrete control space

$$\mathcal{U}^{\Delta_I} = \mathbb{R}^{L \times (N_0 d)}, \quad (5.2)$$

equipped with the inner product

$$(\boldsymbol{\alpha}, \boldsymbol{\beta})_{\Delta_I} = \sum_{\ell=0}^{L-1} \Delta t^\ell \boldsymbol{\alpha}^\ell \cdot \boldsymbol{\beta}^\ell = \sum_{\ell=0}^{L-1} \sum_{n=1}^{N_0} \Delta t^\ell \alpha_n^\ell \cdot \beta_n^\ell,$$

and discretize the state equation (7.5a),(4.9b) and the adjoint state equation (4.10a),(7.6b) by the explicit Euler method. Introducing the notations

$$\mathbf{x} = \{\mathbf{x}^\ell\}_{\ell=0}^L, \quad \mathbf{x}^\ell = \{x_n^\ell\}_{n=1}^{N_0}, \quad x_n^\ell \approx x_n(t^\ell), \quad (5.3a)$$

$$\mathbf{p} = \{\mathbf{p}^\ell\}_{\ell=0}^{L-1}, \quad \mathbf{p}^\ell = \{p_n^\ell\}_{n=1}^{N_0}, \quad p_n^\ell \approx p_n(t^\ell), \quad (5.3b)$$

$$\boldsymbol{\alpha} = \{\boldsymbol{\alpha}^\ell\}_{\ell=0}^{L-1}, \quad \boldsymbol{\alpha}^\ell = \{\alpha_n^\ell\}_{n=1}^{N_0}, \quad \alpha_n^\ell \approx \alpha_n(t^\ell), \quad (5.3c)$$

the discretized optimality system reads

$$\frac{\mathbf{x}^{\ell+1} - \mathbf{x}^\ell}{\Delta t^\ell} = A(\mathbf{x}^\ell) \boldsymbol{\alpha}^\ell, \quad \ell = 0, \dots, L - 1, \quad (5.4a)$$

$$\mathbf{x}^0 = \mathbf{x}^{(0)}, \quad (5.4b)$$

$$\frac{\mathbf{p}^{\ell-1} - \mathbf{p}^\ell}{\Delta t^\ell} = B(\mathbf{x}^\ell, \boldsymbol{\alpha}^\ell)^T \left( \mathbf{p}^\ell + \frac{1}{2} \boldsymbol{\alpha}^\ell \right), \quad \ell = L_j - 1, \dots, L_{j-1}, \quad (5.5a)$$

$$\mathbf{p}^{L_q-1} = 0, \quad \mathbf{p}^{L_j-1} = \mathbf{p}^{L_{j-1}} + \lambda_j \nabla \text{Disp}_j(\mathbf{x}^{L_j}), \quad j = q, \dots, 1 \quad (5.5b)$$

---


$$A(\mathbf{x}^\ell) (\boldsymbol{\alpha}^\ell + \mathbf{p}^\ell) = \mathbf{0} \quad , \quad 0 \leq \ell \leq L - 1. \quad (5.6)$$

The condition (5.5b), representing the jump discontinuities of  $\mathbf{p}^{L_j-1}$  at discrete times  $t^{L_j-1}$  ( $= t^{L_j} - \Delta t^{L_j}$ ), is the discrete version of (7.6b) for jump discontinuities of  $p^*(\cdot)$  at snapshot time frames  $t_j$  ( $= t^{L_j}$ ),  $1 \leq j \leq q$ . This time backward shift of jump discontinuities by steplength  $\Delta t^{L_j}$  stems from our choice of the explicit Euler method for the time discretization of the state equation (5.4a) and the adjoint state equation (5.5a). It turns out that (5.4)-(5.6) represent the optimality conditions for a discrete minimization problem. In fact, introducing  $J^{\Delta_I}(\boldsymbol{\alpha})$  as the discrete objective functional

$$J^{\Delta_I}(\boldsymbol{\alpha}) := \sum_{\ell=0}^{L-1} \frac{\Delta t^\ell}{2} (\boldsymbol{\alpha}^\ell)^T A(\mathbf{x}^\ell) \boldsymbol{\alpha}^\ell + \sum_{j=1}^q \lambda_j \text{Disp}_j(\mathbf{x}^{L_j}), \quad (5.7)$$

we have the following result.

**Theorem 5.1.** *The equations (5.4)-(5.6) are the first order necessary optimality conditions for the finite dimensional minimization problem*

$$\min_{\boldsymbol{\alpha} \in \mathcal{U}^{\Delta_I}} J^{\Delta_I}(\boldsymbol{\alpha}) \quad (5.8)$$

*subject to the discrete state equations (5.4a),(5.4b).*

**Proof.** *The proof is the discrete analogue of the proof of Theorem 4.1 and will thus be omitted.*

**Corollary 5.2.** *Let  $(\mathbf{x}^*, \mathbf{p}^*, \boldsymbol{\alpha}^*)$  with  $\mathbf{x}^* = \{\mathbf{x}_*^\ell\}_{\ell=0}^L$ ,  $\mathbf{p}^* = \{\mathbf{p}_*^\ell\}_{\ell=0}^L$ ,  $\boldsymbol{\alpha}^* = \{\boldsymbol{\alpha}_*^\ell\}_{\ell=0}^L$  satisfy the discrete optimality system (5.4)-(5.6). Then, it holds*

$$\mathbf{0} = \nabla J^{\Delta_I}(\boldsymbol{\alpha}^*), \quad (5.9)$$

where

$$\nabla J^{\Delta I}(\boldsymbol{\alpha}^*) = \{\mathbf{g}^\ell\}_{\ell=0}^{L-1}, \quad \mathbf{g}^\ell = A(\mathbf{x}^\ell) (\boldsymbol{\alpha}_*^\ell + \mathbf{p}_*^\ell). \quad (5.10)$$

**Proof.** We observe that

$$\delta J^{\Delta I}(\boldsymbol{\alpha}) = (\nabla J^{\Delta I}(\boldsymbol{\alpha}), \delta \boldsymbol{\alpha})_{\Delta I}. \quad (5.11)$$

From (5.7) we deduce

$$\begin{aligned} \delta J^{\Delta I}(\boldsymbol{\alpha}) &= \sum_{\ell=0}^{L-1} \Delta t^\ell \left( (\boldsymbol{\alpha}^\ell)^T A(\mathbf{x}^\ell) \delta \boldsymbol{\alpha}^\ell + \frac{1}{2} (\boldsymbol{\alpha}^\ell)^T B(\mathbf{x}^\ell, \boldsymbol{\alpha}^\ell) \delta \mathbf{x}^\ell \right) \\ &\quad + \sum_{j=1}^q \lambda_j \nabla \text{Disp}_j(\mathbf{x}^{L_j}) \delta \mathbf{x}^{L_j}, \end{aligned} \quad (5.12a)$$

where

$$\frac{\delta \mathbf{x}^{\ell+1} - \delta \mathbf{x}^\ell}{\Delta t^\ell} = A(\mathbf{x}^\ell) \delta \boldsymbol{\alpha}^\ell + B(\mathbf{x}^\ell, \boldsymbol{\alpha}^\ell) \delta \mathbf{x}^\ell, \quad \ell = 0, \dots, L-1, \quad (5.12b)$$

$$\delta \mathbf{x}^0 = \mathbf{0}. \quad (5.12c)$$

Multiplying both sides of (5.12b) by  $\mathbf{p}^\ell$ , partial summation yields

$$\begin{aligned} 0 &= \sum_{\ell=0}^{L-1} \Delta t^\ell \mathbf{p}^\ell \cdot \left( \frac{\delta \mathbf{x}^{\ell+1} - \delta \mathbf{x}^\ell}{\Delta t^\ell} - A(\mathbf{x}^\ell) \delta \boldsymbol{\alpha}^\ell - B(\mathbf{x}^\ell, \boldsymbol{\alpha}^\ell) \delta \mathbf{x}^\ell \right) \\ &= \sum_{\ell=1}^{L-1} \Delta t^\ell \frac{\mathbf{p}^{\ell-1} - \delta \mathbf{p}^\ell}{\Delta t^\ell} \cdot \delta \mathbf{x}^\ell + \mathbf{p}^{L-1} \cdot \delta \mathbf{x}^L - \mathbf{p}^0 \cdot \delta \mathbf{x}^0 - \sum_{\ell=0}^{L-1} \Delta t^\ell \mathbf{p}^\ell \cdot A(\mathbf{x}^\ell) \delta \boldsymbol{\alpha}^\ell \\ &\quad - \sum_{\ell=0}^{L-1} \Delta t^\ell \mathbf{p}^\ell \cdot B(\mathbf{x}^\ell, \boldsymbol{\alpha}^\ell) \delta \mathbf{x}^\ell. \end{aligned} \quad (5.13)$$

If we take (5.5a),(5.5b) into account, it follows from (5.13), (5.12a) that

$$\delta J^{\Delta I}(\boldsymbol{\alpha}) = \sum_{\ell=0}^{L-1} \Delta t^\ell A(\mathbf{x}^\ell) (\boldsymbol{\alpha}^\ell + \mathbf{p}^\ell) \cdot \delta \boldsymbol{\alpha}^\ell. \quad (5.14)$$

Since  $\delta \boldsymbol{\alpha} = \{\delta \boldsymbol{\alpha}^\ell\}_{\ell=0}^{L-1}$  is arbitrary, (5.11) results in

$$\nabla J^{\Delta I}(\boldsymbol{\alpha}) = \{\mathbf{g}^\ell\}_{\ell=0}^{L-1}, \quad \mathbf{g}^\ell = A(\mathbf{x}^\ell) (\boldsymbol{\alpha}^\ell + \mathbf{p}^\ell). \quad (5.15)$$

---

In view of (5.9),(5.10), the discrete minimization problem (5.8) can be solved by a gradient based algorithm operating in  $\mathcal{U}^{\Delta t}$ .

---

### Numerical Solutions of the Optimization Problem

---

#### **6.1 Diffeomorphic Matching for Multiple Snapshots of 3D Curves and Surfaces**

We compute a diffeomorphic matching for multiple snapshots of 3D curves, 3D surfaces, or finite unions of 3D curves and surfaces, by solving the minimization problem (5.8) with  $q$  weighting factors  $\lambda_j = \lambda, 1 \leq j \leq q$ , in the objective functional (5.7), where the weights help balance the various matching accuracies desirable for the  $q$  given snapshots .

## 6.1. DIFFEOMORPHIC MATCHING FOR MULTIPLE SNAPSHOTS OF 3D CURVES AND SURFACES

---

The gradient descent algorithms we have implemented and tested all use an outer/inner iterative scheme which features a continuation method in the regularization parameter  $\lambda$  as outer iterations and a gradient method with Armijo line search (cf., e.g., [3]) as inner iterations.

The *continuation method* plays an essential and efficient part : the regularization parameter  $\lambda$  is initialized at a low value and is increased by moderate multiplicative steps until the  $q$  geometric matching disparities with the given  $q$  snapshots have all reached a preassigned low target level. After each multiplicative increase of  $\lambda$ , the gradient  $G$  of the objective function jumps up in norm, and we keep  $\lambda$  fixed during an "inner" iteration of the gradient descent, until the norm of  $G$  reaches again a low preassigned value. The value of  $\lambda$  is then increased again ("outer" iteration).

At the end of the inner gradient descent iteration performed at a fixed value  $\lambda$ , the kinetic energy and the disparity term in the objective function  $J = Kin + \lambda Disp$  reach terminal values  $Kin_\lambda$  and  $Disp_\lambda$ . In  $R^2$ , the points  $[Kin_\lambda, Disp_\lambda]$  define a curve  $\Gamma \subset R^2$  parametrized by  $\lambda > 0$  called the *Pareto frontier* of the objective function  $J$ . The convexity of the Pareto frontier is usually a desirable feature for regularized optimization problems, and we have empirically observed this convexity in all the multiple snapshots matching applications we have studied below.

In the applications presented below, the given snapshots  $S_j = S_{t_j} \subset R^3, 0 \leq j \leq q$ , are assumed to have been generated at fixed instants  $t = t_j$  by unknown diffeomorphic deformations  $S(t)$  of a known initial deformable shape  $S(0)$ . The initial shape  $S(0)$  is a finite union of geometric components  $C_i$ , where each  $C_i$  is either a segment of piecewise smooth 3D-curve, or a piecewise smooth 3D-surface with piecewise smooth

boundary. Pairs  $C_i, C_k$  of components may intersect, but then these intersections are also components of  $S(0)$ .

Each snapshot  $S_j$  is then discretized (with arbitrary accuracy) by a finite mesh of points  $X_j = \{x_1^j, \dots, x_{N_j}^j\}$  where typically the number  $N_0$  of points on the reference configuration  $S_0$  is much smaller than the number  $N_j, 1 \leq j \leq q$ , of points on the other given snapshots. Indeed, the complexity of the numerical problem to be solved after discretization is essentially determined by the number  $N_0$  of discrete trajectories recomputed at each step of each inner iteration.

### 6.1.1 Initialization of the Gradient Method with Armijo Line Search

We first note that after the time and space discretization in order to initialize the unknown vector  $\alpha$  defined 5 , one can initialize first the unknown family of time dependent vector fields  $v = (v_t(x))$  , and then invert, for each value t of the discretized times, a large linear system of the type  $v = M_t \alpha$  , where  $M_t$  is a positive definite matrix for which the non zero coefficients are of the form  $K(x, y)$  for various  $x, y \in R^3$ . Here,  $K$  is the fixed radial Gaussian kernel defining the kinetic energy.

Of course to avoid this initial inversion of large matrices, one can crudely initialize  $\alpha$  by setting  $\alpha = 0$ . This turns out to be an acceptable choice in several of our numerical applications, but clearly does not allow the use of existing complementary information on the solution which may be known in concrete situations.

**6.1.1.0.1 Rough initialization by a smooth flow of affine transformations.**

Given two snapshots  $S$  and  $S'$  of homeomorphic 3D-surfaces with boundaries, one can discretize  $S$  and  $S'$  by two finite point meshes  $X$  and  $X'$ . Diagonalization of the inertia matrices of  $X$  and  $X'$  around their centers of gravity  $O, O'$  generates the unit eigenvectors  $e_1, e_2, e_3$  and  $e'_1, e'_2, e'_3$  with associated positive eigenvalues  $\gamma_1, \gamma_2, \gamma_3$  and  $\gamma'_1, \gamma'_2, \gamma'_3$ . Call  $T$  the translation mapping  $O$  on  $O'$ ,  $R$  the rotation mapping  $e_1, e_2, e_3$  on  $e'_1, e'_2, e'_3$ , and  $A$  the affinity mapping  $e_1, e_2, e_3$  on  $\frac{\gamma'_1}{\gamma_1}e'_1, \frac{\gamma'_2}{\gamma_2}e'_2, \frac{\gamma'_3}{\gamma_3}e'_3$ . The affine linear transformation  $L = ART$  of  $R^3$  maps  $X$  on  $LX$ , which has the same matrix of inertia as  $X'$ . One can obviously imbed explicitly and separately  $A, R, T$  into differentiable semi-groups  $A(t), R(t), T(t)$  of affinities, rotations, and translations, such that  $[A(1), R(1), T(1)] = [A, R, T]$  and  $[A(0), R(0), T(0)] = [Id, Id, Id]$ , where  $Id$  is the identity transformation of  $R^3$ . Then the affine linear transformations  $L(t) = A(t)R(t)T(t)$  are  $R^3$ -diffeomorphisms depending smoothly on  $t$  such that  $L(0) = Id, L(1) = L$ . They provide a first rough initialization for the unknown flow of diffeomorphisms matching  $X$  and  $X'$ . The associated vector fields defined for  $t \in R^+, x \in R^3$  by  $v_t(x) = \frac{dL(t)}{dt}x$  are a crude initialization for the numerical search of a vector field solution of an optimal matching between  $S$  and  $S'$ .

For the multiple snapshots case, one applies this initialization successively between  $S_j$  and  $S_{j+1}$  on the time interval  $[t_j, t_{j+1}]$  to compute an initial family of time dependent vector fields  $v_t(x)$  such that the associated diffeomorphic flow quite roughly matches  $S_0$  with the successive snapshots  $S_j$ .

**6.1.1.0.2 Hierarchical initialization by B-splines matching.** Consider two homeomorphic bounded 3D surfaces  $S_0$  and  $S_1$  discretized by finite point meshes

6.1. *DIFFEOMORPHIC MATCHING FOR MULTIPLE SNAPSHOTS OF 3D CURVES AND SURFACES*

---

$X_0, X_1$  with compact piecewise smooth boundaries  $B_0$  and  $B_1$ . Select arbitrary arc length origins  $P_0$  and  $P_1$  on  $B_0$  and  $B_1$  and let  $(a_0, a_1)$  be the corresponding Euclidean arc lengths abscissas on  $B_0$  and  $B_1$ . Define a piecewise smooth diffeomorphism  $f$  of  $B_0$  onto  $B_1$  as follows: for each  $Q \in B_0$ , set  $f(Q) = U \in B_1$  where  $a_1(U) = ca_0(Q)$  and  $c$  is the ratio of the lengths of  $B_0$  and  $B_1$ . Using the gradient descent algorithm defined above, we can then numerically determine a time dependent vector field  $w = w_t(x), t > 0, x \in R^3$  such that the associated flow of  $R^3$ -diffeomorphisms  $F_t$  verifies  $F_1(Q)$  close to  $f(Q)$  for all  $Q \in B_0$ . This is an easy optimization problem, since  $B_0$  is one dimensional and the desired mapping  $f$  of  $B_0$  onto  $B_1$  is known, so that numerical convergence is quite fast.

One can then generate a discretized surface  $X_\tau = F_\tau(X_0)$  with boundaries  $B_\tau = F_\tau(B_0)$  for any  $\tau \leq 1$ . Select a  $\tau < 1$  fairly close to 1 and discretize  $B_\tau$  by a finite mesh  $\partial X_\tau$ . Fix  $\varepsilon > 0$ . By a relaxation algorithm, provided  $\varepsilon$  is not too small, it is possible to select targets  $z(x) \in B_1$  for each  $x \in X_0$  such that the map  $x \rightarrow z(x)$  is injective on  $X_0$ , and such that the points  $z(x)$  and  $F_\tau(x)$  verify

$$\|z(x) - F_\tau(x)\| < \varepsilon + d(F_\tau(x), X_1), \quad \text{where} \quad d(y, X_1) = \min_{u \in X_1} \|u - y\|.$$

We then seek an  $R^3$ -valued function  $Pol(t, x)$  defined for  $\tau \leq t \leq 1$  and  $x \in R^3$  by linear combinations of cubic B-splines and such that we have  $Pol(\tau, x) = x$  for all  $x \in X_\tau \cup \partial X_\tau$ , and  $Pol(1, x) = z(x) \forall x \in X_\tau$ . This involves the resolution of a standard linear system for B-splines. Our initial time dependent vector fields  $v = v_t(x)$  for gradient descent is then defined by  $v_t = w_t$  for  $0 \leq t \leq \tau$  and by  $v_t(x) = \partial_t Pol(t, x)$  for all  $x \in R^3$  and  $\tau < t \leq 1$ .

### 6.1.2 Smoothing of the Hausdorff Disparity

In general, the Hausdorff distance (2.15) is not a smooth function. For our gradient descent with Armijo line search we define a smoothed version of the Hausdorff disparity as follows. Consider two compact 3D shapes  $S$  and  $S'$  discretized by finite meshes  $X$  and  $Y$ . Define functions  $\phi : X \rightarrow Y$  and  $\psi : Y \rightarrow X$

$$\phi(x) = \operatorname{argmin}_{y \in Y} \|x - y\| \quad \forall x \in X, \quad (6.1)$$

$$\psi(y) = \operatorname{argmin}_{x \in X} \|y - x\| \quad \forall y \in Y. \quad (6.2)$$

Clearly, these two functions are continuous but not necessarily injective. For each  $x \in X$  define  $U(x) \subset X$  as the set of the  $r$  closest neighbors of  $x$  in  $X$  including  $x$ . Similarly, one defines neighborhoods  $U(y) \subset Y$  of  $y$  for all  $y \in Y$ . The smoothed Hausdorff disparities  $h(X, Y)$  and  $h(Y, X)$  are defined by

$$h(X, Y) = (1/r|X|) \sum_{x \in X} \sum_{z \in U(\phi(x))} \|x - z\|^2, \quad (6.3)$$

$$h(Y, X) = (1/r|Y|) \sum_{y \in Y} \sum_{z \in U(\psi(y))} \|y - z\|^2, \quad (6.4)$$

where  $|X|, |Y|$  are the cardinals of  $X, Y$ . The numerical gradients of  $h(X, Y)$  and  $h(Y, X)$  with respect to variations of  $X$  when  $Y$  remains fixed are always approximated by "freezing" temporarily the points  $\phi(x)$  and  $\psi(y)$ , since the functions  $\phi$  and  $\psi$  are not everywhere differentiable.

The smoothed Hausdorff disparity between  $X$  and  $Y$  will be defined by  $D_H(X, Y) = h(X, Y) + h(Y, X)$ , and will sometimes be referred to below as "global Hausdorff disparity" between  $X$  and  $Y$ . For diffeomorphic matching of surfaces  $S$  and  $S'$  with

boundaries  $\partial S$  and  $\partial S'$ , we always compute separate Hausdorff disparities between discretized versions of the interior sets  $S^o, S'^o$  and of the boundaries  $\partial S, \partial S'$ .

### 6.1.3 Choice of the Scale Parameters in the Gaussian Kernels

When the scale parameter  $\sigma > 0$  of the radial Gaussian kernel  $K_\sigma$  (2.14) defining the Hilbert space  $V = V_K$  increases, then the spatial smoothness of the optimal diffeomorphic deformations tends to increase. Call  $X$  the finite discretization of the interior of an initial surface or curve  $S_0$ . Define  $\dim(X)$  as the dimension of  $S_0$ . For each  $x \in X$ , and each fixed integer  $r > 0$ , define as above  $U(x) \subset X$  as the set of the  $r$  closest neighbors of  $x$  in  $X$ , including  $x$  itself. We then define the radius function  $\rho(x) > 0$  by

$$\rho(x) = \max_{z \in U(x)} \|x - z\| \quad \forall x \in X.$$

The maximum  $R(X) = \max_{x \in X} (\rho(x))$  of the function  $\rho$  concretely defines the *local mesh size* of  $X$ .

We naturally chose  $r = 3$  when  $S_0$  is a curve segment or when  $X$  is a finite discretization of the boundary  $\partial S_0$ , and  $r = 5$  when  $S_0$  is a surface.

Based on the local mesh size  $R(X)$  of  $X$ , we select the scale parameter  $\sigma$  for the radial Gaussian kernel defining the kinetic energy as follows

$$\sigma = \kappa 2^{-1/2} R(X), \tag{6.5}$$

where  $\kappa$  is some constant satisfying  $2 \geq \kappa \geq 1$ . This choice clearly bounds the number of neighbors  $y \in X$  of any given point  $x \in X$  such that the deformation trajectory of  $y$  influences the deformation trajectory of  $x$ .

The scale parameter  $\sigma$  is generally kept fixed during the whole gradient descent, but can be updated dynamically after enough iterations. Numerical evidence suggests to choose  $\sigma$  according to (6.5) and to keep it fixed during the whole process, when there is not much difference between the local mesh sizes selected for the multiple snapshots.

The scale parameter of the radial Gaussian kernel defining the Hilbert distance between bounded measures on  $R^3$  (see (2.17)) is selected to have the order of magnitude of the Hausdorff distances between the given snapshots  $S_j$  and the current deformed shapes  $\hat{S}_j$  at instants  $t_j$  and is updated periodically, in particular when the initialization is not close enough to the assigned multiple snapshots.

## 6.2 Continuation in the Regularization Parameter

Consider first the situation where the weights  $\lambda_j$  in the disparity cost functional (2.18) are all equal to the same  $\lambda > 0$ . This regularization parameter provides a weighting between the kinetic energy (2.3) and the disparity cost functional. For  $\lambda$  small, the regularizing effect of the kinetic energy dominates, whereas large values of  $\lambda$  enhance the matching quality of deformed shapes  $\hat{S}_j$  and the given snapshots  $S_j$ . To reach a good matching quality, one needs to minimize the objective function  $J$  for fixed but sufficiently large  $\lambda$ . However, for increasing  $\lambda$ , the system of optimality

## 6.2. CONTINUATION IN THE REGULARIZATION PARAMETER

---

equations equivalent to  $\text{grad}J = 0$  becomes more and more ill-conditioned, which may result in divergence of the gradient descent. A convenient remedy to overcome this obstacle is to use an appropriate "continuation" in  $\lambda$ . The continuation method consists in combining outer iterations in  $\lambda$  with inner iterations at fixed  $\lambda$ , which we chose to implement by classical gradient descent with Armijo line search (cf., e.g., [3]).

To monitor progress during the outer iterations, we compute  $q$  *performance indicators*  $\text{Dist}_j$ , one for each given snapshot  $S_j$ ,  $j = 1, \dots, q$ , as follows.

$$j = 1, \dots, q, \quad \text{Dist}_j := 90\text{th percentile of } \{d_1^j, \dots, d_{N_0}^j\}, \quad (6.6)$$

where the distances  $d_n^j$ ,  $n = 1, \dots, N_0$ , are defined by

$$d_n^j = \min_{m=1, \dots, N_j} \|x_n(t_j) - x_m^j\|$$

Hence, each  $\text{Dist}_j$  provides an upper bound for 90% of the current geometric errors affecting the points of the current deformed surface  $\hat{S}_j$ . In practical applications, the given snapshots  $S_j$  are typically determined by 3D-image data where geometric accuracy is bounded by the image resolution. For example in Chapter 8 the algorithmic modeling of the  $S_j$  by NURBS introduces other sources of geometric inaccuracy in the  $S_j$  data. Hence one can generally preassign a target threshold level  $\text{THR} > 0$  for the performance indicators  $\text{Dist}_j$ , and we can say that good matching with all the intermediary snapshots has been reached as soon as all the  $\text{Dist}_j$  are smaller than  $\text{THR}$ .

As described above, the continuation method implements a succession of inner iterations, which are gradient descents at fixed  $\lambda$ , and at the end of each inner

## 6.2. CONTINUATION IN THE REGULARIZATION PARAMETER

---

iteration, the regularization parameter  $\lambda$  is increased (outer iteration) by a constant multiplicative factor  $\gamma > 1$ .

At the end of each inner iteration, we want the norm of gradient  $J$  to have decreased at least by a fixed multiplicative factor  $\theta < 1$ .

Formally the continuation method reads as follows:

### **Step 1 (Initialization of the outer iteration)**

Specify a small initial value  $\lambda_0 > 0$  and set  $\nu = 0$ .

### **Step 2 (Initialization of the inner iteration)**

Compute  $\alpha_\nu^{(0)}$  by one of the initialization procedures as outlined above in subsection 8.1 and set  $\mu = 0$ .

### **Step 3 (Gradient method with Armijo line search)**

**Step 3.1** Set  $\mu := \mu + 1$  and compute  $\alpha_\nu^{(\mu)}$  by gradient descent with Armijo line search.

**Step 3.2** If the gradient  $\nabla J$  of the objective function  $J$  verifies the termination criterion

$$|\nabla J(\alpha_\nu^{(\mu)})| < \theta |\nabla J(\alpha_\nu^{(0)})| \quad (6.7)$$

is satisfied, go to Step 4. Otherwise, go to Step 3.1.

If the gradient method fails to converge, adjust the parameter in the Armijo line search, set  $\mu := 0$ , and go to Step 3.1.

### **Step 4 (Termination of the outer iteration)**

If the threshold based termination criterion

$$\text{Dist}_j < \text{THR} \quad , \quad 1 \leq j \leq q, \quad (6.8)$$

## 6.2. CONTINUATION IN THE REGULARIZATION PARAMETER

---

is satisfied, stop the algorithm.

Otherwise, set  $\nu := \nu + 1$ ,  $\boldsymbol{\alpha}_\nu^{(0)} := \boldsymbol{\alpha}_{\nu-1}^{(\mu)}$ , and increase the regularization parameter by

$$\lambda_\nu := \gamma \lambda_{\nu-1}, \tag{6.9}$$

and go to Step 3.

## CHAPTER 7

---

### Smoothing in Time Domain

---

For the optimal control systems 3.1 in Chapter 2 and 4.8 in Chapter 4 which were formulated to obtain optimal matching of a sequence of submanifolds in infinite dimensional setup and in diffeomorphic point matching setup, respectively, we observe that the solution of the adjoint equation derived as a part of first order optimality conditions is capable of being discontinuous in time, namely at the time instances where we expect the deforming submanifold to match with a known submanifold. Hence when we solve numerically the fully discrete system 5.12 associated with 4.8 we expect to see non-smooth transition of the deformed object in time. In this chapter we present numerical experiments featuring multiple snapshots. We quantify the

non-smooth transitions of the deformation in time by analyzing individual trajectories associated with the deformation of the mesh points of reference surface. We then add a smoothing term with a smoothing parameter  $\mu$  in the functional associated with the semi discrete optimal control problem 5.12 and derive necessary optimality conditions for the new control problem. In the last section of this chapter we study the effect of the smoothing term on the optimal solution for two cases: multiple  $1D$  submanifolds and multiple  $2D$  submanifolds, by varying the smoothing parameter  $\mu$  starting with  $\mu = 0$ , i.e. the solution when the smoothing term is not present.

## 7.1 Solutions with Non-smooth Transitions in Time

In this section we discuss about the non-smooth transitions in time by presenting some numerical experiments implemented using the methods described in Chapter 6.

### 7.1.1 Data

We have 10 parametric curves  $C_0, \dots, C_9$  corresponding to 10 snapshots of a deforming closed 3D curve available at 10 time instances,  $t_0 < t_1 \dots < t_9$ . Here, without loss of generality we assume that the time instances are between time unit 0 and 1. These curves represent a fibrous ring part of human mitral valve known as annulus during one heart cycle of a specific patient, and extraction of these parametric equations involve a sequence of tedious work. For details we refer to section 8.1.4 of Chapter 8.

However, for the time being we can just think of these as 1D submanifolds of  $\mathbb{R}^3$ . Our task is to obtain a time dependent diffeomorphism  $F_t$  which deforms shape  $C_0$  such that it is as close to the given snapshots at time  $t_j$ ,  $\forall 1 < j < 9$ . We identify these curves by set of points  $X_0, \dots, X_9$  extracted using the parametric curve equations.

### 7.1.2 Quantifying the Non-smoothness of Solution

One way to observe the non-smoothness of the solution in time space, is to look at the angles between the two line segments obtained by joining three consecutive points on each trajectory  $x_i(t) := F_t(x_i(0))$ ,  $t \in (0, 1)$  for all  $x_i(0) \in X_0$  and  $0 = l_0, l_1, l_2, \dots, l_M = 1$ , i.e. we find  $\theta_t(x_i)$  as defined in (7.1).

$$\theta_t(x_i) = \arccos \left( \frac{(x_i(t+1) - x_i(t)) \cdot (x_i(t) - x_i(t-1))}{|(x_i(t+1) - x_i(t))| |(x_i(t) - x_i(t-1))|} \right). \quad (7.1)$$

The more bigger  $\theta_t(x_i)$  the more irregular the associated trajectory is and in turn the obtained optimal diffeomorphism. Hence smaller values for  $\theta_t$ , would imply smoother solution. Figure 7.1 shows the time evolution of the average of  $\theta_t$  i.e.

$$\theta_t^{\text{Avg}} = \frac{1}{Nx} \sum_{i=1}^{Nx} \theta_t(x_i) \quad (7.2)$$

Clearly we observe that the angle is very sharp at the time instances  $t_j, j = 1, \dots, 9$ , i.e. time when the snapshots are known.

## 7.2 Modified Functional

The discontinuity of the solution of the adjoint state equations is not only reflected in the state variables but is also reflected on control variable  $\alpha$ , cf figure(7.2). Since

## 7.2. MODIFIED FUNCTIONAL

---

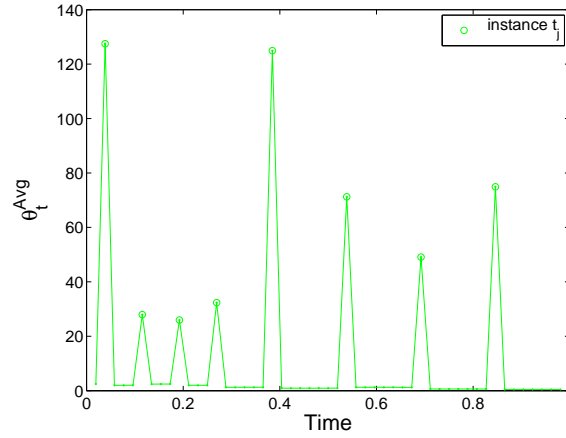


Figure 7.1: x axis represent the time and y axis represent  $\theta_t^{\text{Avg}}$  as defined in 7.2, 'o' represent the value at time  $t_j, j = 1, \dots, 9$  i.e. time instances with known snapshots

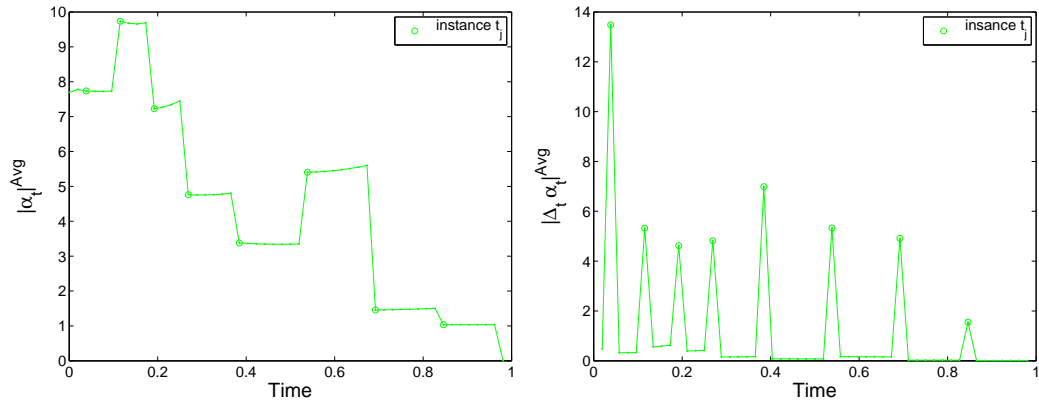


Figure 7.2: Left figure depicts the time evolution of the average of the norm of  $\alpha(t)$ , right figure depicts the evolution of the average of finite difference derivative of  $\alpha(t)$  with respect to time

## 7.2. MODIFIED FUNCTIONAL

---

we also observe discontinuity in control variable we add a smoothing term involving the time derivatives of the control variable in the objective functional. Recalling the notations from page 35 we write the new objective function as

$$J(\alpha) = \frac{1}{2} \int_0^1 \alpha(t)^T A(x(t)) \alpha(t) dt + \lambda \left( \sum_{j=1}^q \lambda_j \text{Disp}_j(x(t_j)) + \frac{\mu}{2} \int_0^1 \frac{d\alpha^T}{dt} \frac{d\alpha}{dt} dt \right). \quad (7.3)$$

Hence the new diffeomorphic matching amounts to the solution of the following control problem

$$\inf_{\alpha} J(\alpha), \quad (7.4a)$$

subject to

$$\frac{dx(t)}{dt} = A(x(t)) \alpha(t), \quad t \in (0, 1], \quad (7.4b)$$

$$x(0) = x^{(0)}. \quad (7.4c)$$

Using the Lagrange multiplier techniques as used in chapter 4 we derive the following necessary optimality conditions for the above system

$$\frac{dx^*(t)}{dt} = A(x^*(t)) \alpha^*(t), \quad t \in (0, 1], \quad (7.5a)$$

$$x^*(0) = x^{(0)}, \quad (7.5b)$$

$$-\frac{dp^*(t)}{dt} = B(x^*(t), \alpha^*(t))^T \left( p^*(t) + \frac{1}{2} \alpha^*(t) \right), \quad t \in (t_{j-1}, t_j), \quad (7.6a)$$

$$p^*(t_q^+) = 0, \quad p^*(t_j^-) = p^*(t_j^+) + \lambda_j \nabla \text{Disp}_j(x^*(t_j)) \quad , \quad j = q, \dots, 1, \quad (7.6b)$$

$$A(x^*(t))(\alpha^*(t) + p^*(t)) - \lambda\mu \frac{d^2\alpha}{dt^2} = 0, \quad t \in (0, 1]. \quad (7.7)$$

## 7.3 Adding Local Smoothing Terms to the Objective Functional

We first add local smoothing terms at the time instance where snapshot is known i.e.

$$J(\alpha) = \frac{1}{2} \int_0^1 \alpha(t)^T A(x(t)) \alpha(t) dt + \lambda \left( \sum_{j=1}^q \lambda_j \text{Disp}_j(x(t_j)) + \sum_{j=1}^q \mu_j \frac{|\alpha_{t_j} - \alpha_{t_{j-1}}|^2}{2\Delta t^{j-1}} \right). \quad (7.8)$$

### 7.3.1 Numerical Experiments

We compare different optimal solutions we obtain by solving original variational problem and the one with local regularization term added as described in 7.8. We take values of all  $\mu_j$  same and call it as  $\mu$  and we take  $\lambda_j = 1$ ,  $j = 1, \dots, q$ . As described in section 6.2, we use the continuation in regularization parameter  $\lambda$ . This implies that the ratio between matching term and smoothing term remains same.

Figure(7.3) represent the average of  $\theta_t$  over the mesh points, we see the solution for the original variational form has very narrow angles at  $t_j$  but adding the regularity term increases measure of these angles and as we increase the value of the parameter  $\mu$  it gets better at the intermediary time steps. However if we carefully observe as we start increasing  $\mu$  the angles start getting narrower around the intermediary time steps.

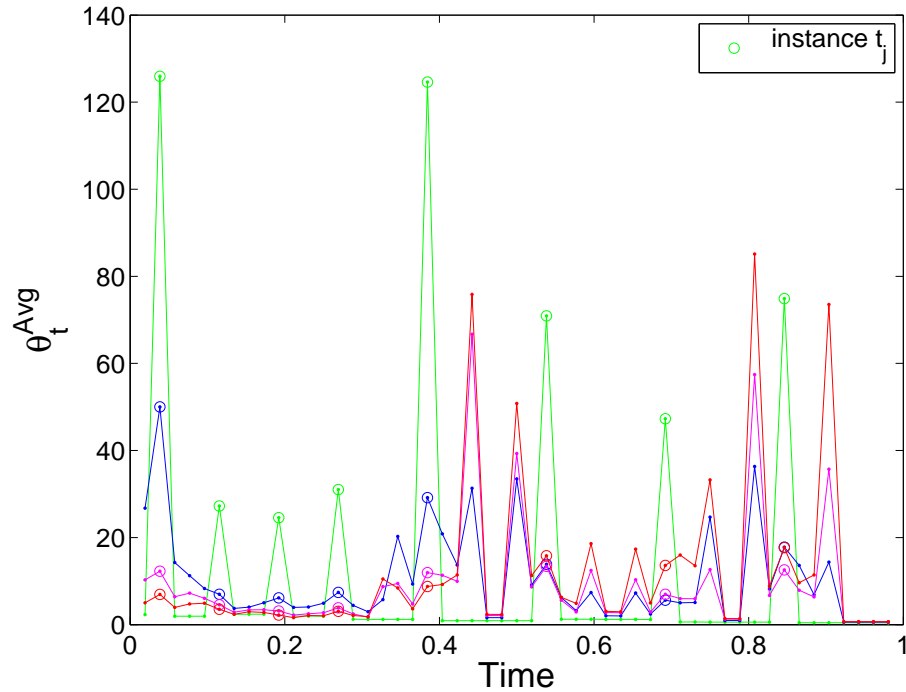


Figure 7.3: average of angles: green-for the original solution, blue-for  $\mu = 0.5$ , pink-for  $\mu = 2$ , red-for  $\mu = 4$  solution with local smoothing term

## 7.4 Adding the Global Smoothing Term to the Objective Functional

### 7.4.1 Results for Curves

We work with same example as discussed above and optimize the new functional 7.3 with different values of  $\mu$ . Figure(7.5) represent the average of  $\theta_t$  over the mesh points, we see the solution for the original variational form has big angles at  $t_j$  but adding the regularity term reduces angles and as we increase the value of the parameter  $\mu$  it improves at the intermediary time steps. In Figure(7.6) we see the changes

## 7.4. ADDING THE GLOBAL SMOOTHING TERM TO THE OBJECTIVE FUNCTIONAL

---

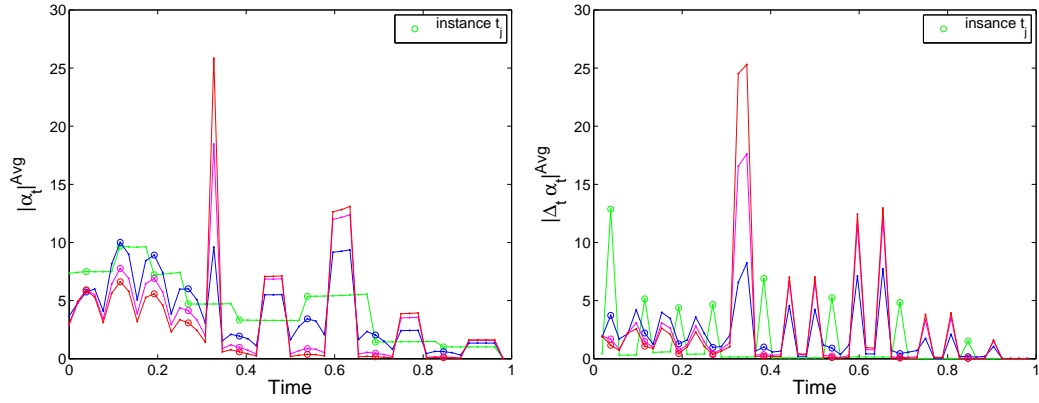


Figure 7.4: average of the norm of  $\alpha_i$ ,  $0 \leq i \leq N_x - 1$ (left),norm of the difference between the alpha of two consecutive time(right)

$\mu$	Kin	$D_{targ}$	$D_{t_1}$	$D_{t_2}$	$D_{t_3}$	$D_{t_4}$	$D_{t_5}$	$D_{t_6}$	$D_{t_7}$	$D_{t_8}$
0	57	0.17	1.12	0.8	0.5	0.7	0.7	0.5	0.84	0.3
0.5	58	0.2	1.15	0.8	0.6	0.65	0.67	0.54	0.7	0.3
2	62	0.2	1.2	0.8	0.7	0.7	0.5	.4	.4	0.3

Table 7.1: Performance indicator at different level of  $\mu$

between different adjoin variable solution  $\alpha_t$  and approximation of it's derivative in time.

In Table(7.1) we compare the performance indicator  $D_{t_j}$  for each snapshot, cf equation(6.6) in Section 6.2. Since we add an extra term in the objective function the desired level of accuracy is attained at different levels of  $\lambda$ , however it is reached at comparable kinetic energy.

7.4. ADDING THE GLOBAL SMOOTHING TERM TO THE OBJECTIVE FUNCTIONAL

---

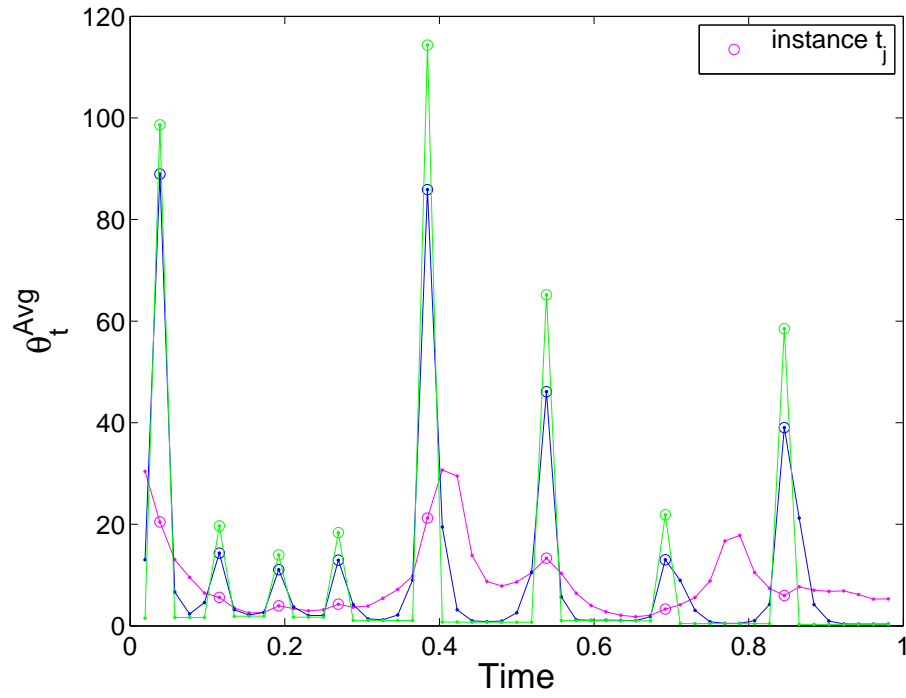


Figure 7.5: average of angles: green-the original solution, blue-  $\mu = 0.5$ , pink-  $\mu = 2$

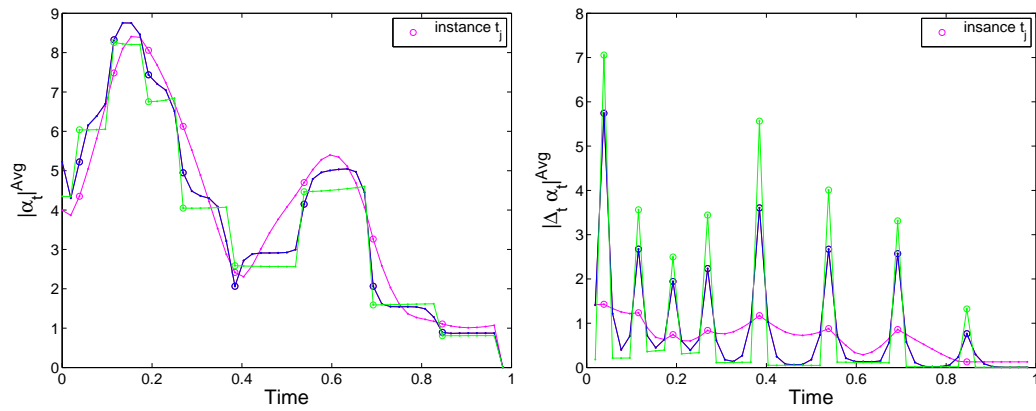


Figure 7.6: average of the norm of  $\alpha_t$ (left), norm of the difference between the alpha of two consecutive time(right)

7.4. ADDING THE GLOBAL SMOOTHING TERM TO THE OBJECTIVE FUNCTIONAL

---

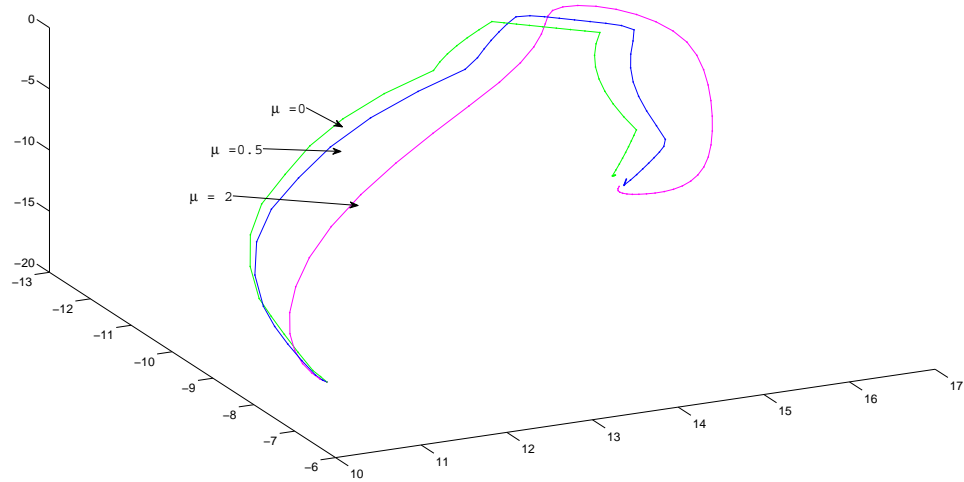


Figure 7.7: One trajectory: uniform time steps and different  $\mu$ :  $\mu = 0$ -green,  $\mu = 0.5$ -blue,  $\mu = 2$ -pink

$\mu$	$\text{mean}(\sum_l \theta_l(x))$	$\text{max}(\sum_l \theta_l(x))$	$\text{min}(\sum_l \theta_l(x))$
0	450	647	262
0.5	470	661	249
2	441	623	235

Table 7.2: Sum of angles

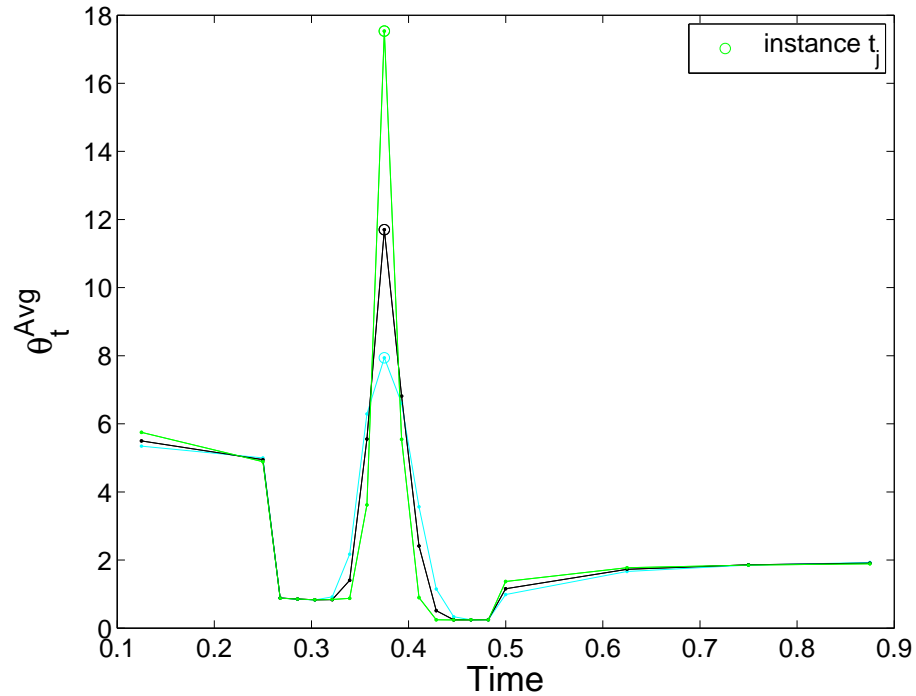


Figure 7.8: Average of angles: green-for the original solution, blue-for  $\mu = 0.5$ , pink-for  $\mu = 2$

### 7.4.2 Result for Surfaces

We consider four snapshots of a dynamic surface. These surfaces are identified by NURBS model, for more details we refer to Section 8.1.4. But for the time being we can just consider them as 2-D sub-manifolds in  $\mathbb{R}^3$ . Since we have less snapshots as compare to the previous case, we expect to get relatively smaller angles. Figure 7.8 is a similar comparison of average of angles for different values of  $\mu$ . Figure 7.9 shows the level of accuracy of the matching at different time instances.

7.4. ADDING THE GLOBAL SMOOTHING TERM TO THE OBJECTIVE FUNCTIONAL

---

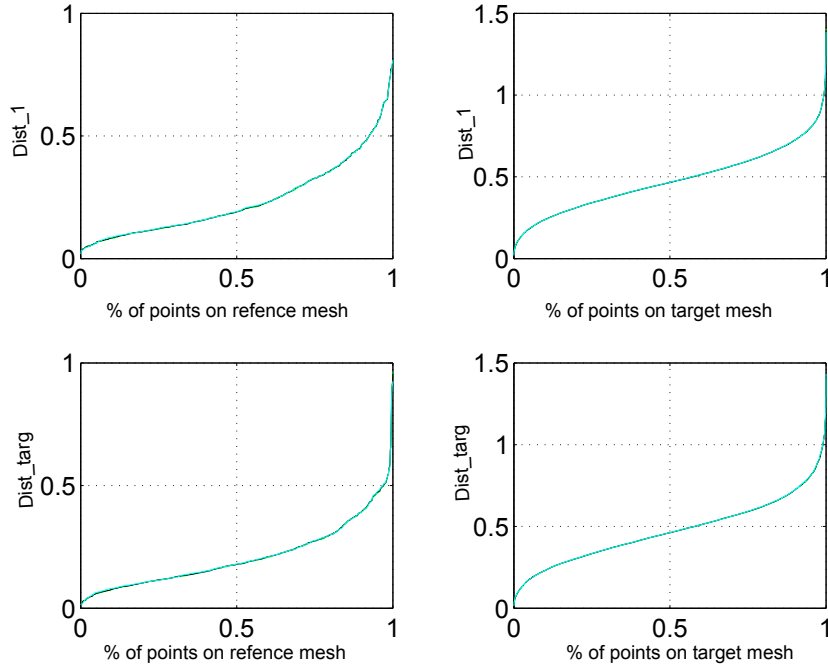


Figure 7.9: Represent the accuracy of the matching, as we can see all the curves overlap and hence we don't compromise on accuracy

$\mu$	$\text{mean}(\sum_l \theta_l(x))$	$\text{max}(\sum_l \theta_l(x))$	$\text{min}(\sum_l \theta_l(x))$
0	50	313	8
0.5	49	315	7
2	49	315	6.81

Table 7.3: Sum of angles

---

# Numerical Results: Reconstructed Motion of Human Mitral Valve

---

### 8.1 Human Mitral Valve Apparatus

Heart is a muscular organ responsible for blood circulation in body through the cardiac cycle. It consists of four chambers: two chambers on top namely the left and right atrium and two chambers on bottom namely the left and right ventricle chambers. Right atrium and right ventricle are connected via tricuspid valve and right atrium is connected to pulmonary arteries via pulmonary valve. Similarly left

## 8.1. HUMAN MITRAL VALVE APPARATUS

---

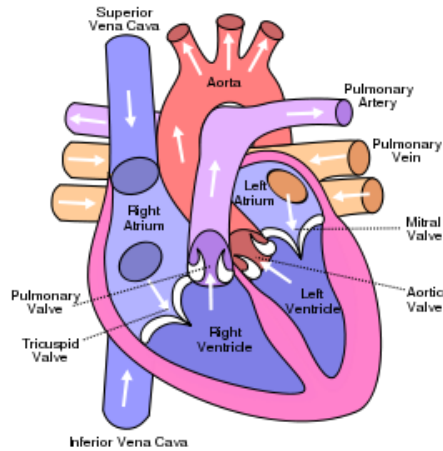


Figure 8.1: Structure of Human Heart

atrium and left ventricle are connected by *Mitral Valve* and left atrium with aorta by aortic valve, cf. Figure 8.1. The deoxygenated blood of the body enters through superior and inferior vena cava and fills in right atrium during diastole, the tricuspid valve is open and right ventricle is filled with venous blood, which is then pumped through pulmonary valve in lungs during systole. Similarly oxygenated blood is filled in the left atrium during diastole and *Mitral Valve* is open and let the blood fill in left ventricle, which is then pumped into the body via aorta through aortic valve during systole, cf. Figure 8.2. All these four valves are unidirectional which is a very important feature required for healthy functioning of heart. Valvular heart disease: stenosis and regurgitation are very commonly found in people. Here we focus on patients suffering from mitral valve regurgitation.

## 8.1. HUMAN MITRAL VALVE APPARATUS

---

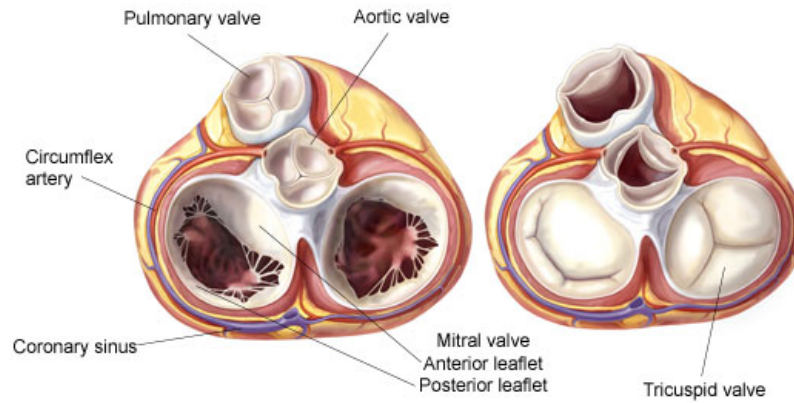


Figure 8.2: The four valves during diastole and systole

### 8.1.1 Anatomy and Physiology of Mitral Valve

Mitral valve is typically 4-6 cm<sup>2</sup> in area. The mitral valve apparatus consists of a saddle shaped annulus(a fibrous ring) and two flaps called leaflets: the anterior and posterior leaflet. Virtually annulus can be divided into two parts anterior and posterior annulus according to the leaflet insertion. The semi-circular shaped anterior leaflet is attached to approximately 40 % of the annulus with its free boundary being indentation free. On the other hand, the quadrangular shaped posterior leaflet has two well-defined indentations that support the opening of the mitral valve.

In a healthy functioning heart, during left ventricle diastole, after the pressure drops in the left ventricular due to relaxation of the ventricular myocardium, the mitral valve opens, and blood filling in left atrium through pulmonary vein starts traveling to left ventricular, followed by the discharge of electrical impulses generated by sinoatrial node( impulse generating tissue located in the right atrium), triggering

## 8.1. HUMAN MITRAL VALVE APPARATUS

---

the atrium to contract. It's then when the left atrium empties the remaining oxygenated blood in the left ventricular which contributes 20% to the volume in the left ventricle prior to ventricular systole. This is also known as left atrial systole. While the left atrium starts relaxing, the mitral valve prevents the oxygenated blood from flowing back into the atrium by coapting the two leaflets together. Left ventricle systole starts exactly when the mitral valve closes. At this point aortic valve is open, the left ventricle receives impulses from the Purkinje fibers (located at the inner walls of the ventricles) and contracts and the oxygenated blood is pumped into the aorta. All this time mitral valve is closed and the leaflets are prevented from prolapsing into the left atrium by the action of tendons attached to the posterior surface of the valve, chordae tendineae. The inelastic chordae tendineae is made of approximately 80% collagen, and the remaining is made up of elastin and endothelial cells. The chordae are attached at one end to the papillary muscles and the other to the valve leaflets, cf Figure (8.3). Papillary muscles are attached to the inner wall of the ventricle. When the left ventricle contracts the intraventricular pressure forces the valve to close, while the tendons keep the leaflet coapting together and prevent prolapsing which results in blood flow in opposite direction.

### 8.1.2 Mitral Valve Regurgitation

Mitral regurgitation is backward flow of oxygenated blood in left atrium during systole, caused by improperly closed mitral valve. It has prevalence of approximately 2% of the population, affecting males and females equally,[55]. Prevalence of this condition would force the heart to work harder to pump the blood to the rest of the

## 8.1. HUMAN MITRAL VALVE APPARATUS

---

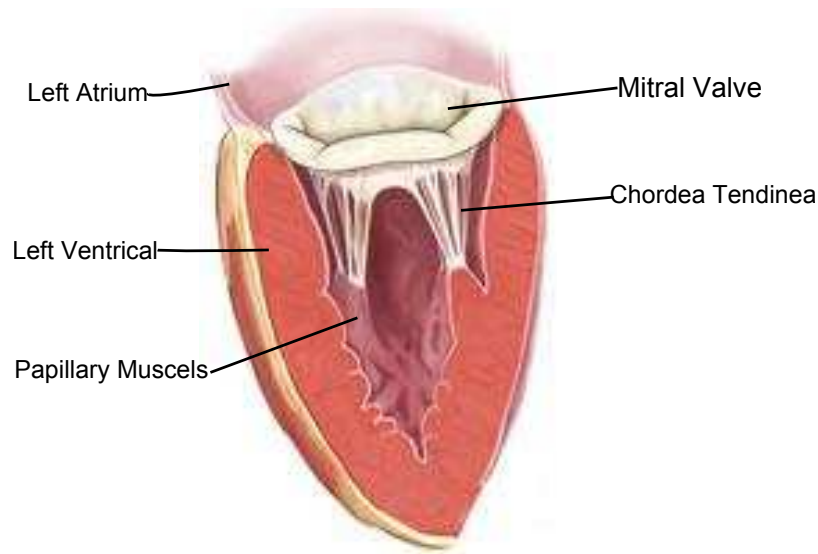


Figure 8.3: Mitral valve posterior surface, chordae tendinea and papillary muscles

body which can lead to congestive heart failiur. The most common cause of mitral regurgitation is mitral valve prolapse, which usually happen due to the elongation of the valve leaflets and the chordae tendineae which prevent the valve to coapting fully.

### 8.1.3 Mitral Valve Regurgitation Treatment: Repair vs. Replacement

There are two surgical options available as a cure for regurgitation: mitral valve repair and mitral valve replacement. Starting from about 1960s, for few decades replacement of mitral valve replacement (valve replaced by an artificial valve) was the only surgical option available. But there were many possible drawbacks with this procedure including: infection of the valve, patients required to take blood thinner

## 8.1. HUMAN MITRAL VALVE APPARATUS

---

can result in many medical complications, more likely to get a stroke, and wear out of the valve in about 10-15 years. In the past two decades a new technique was used where rather than replacing the valve surgeons started repairing the valve. The idea was pioneered by Dr. Alain F Carpentier. One such technique is to insert a ring around the valve to reduce the size of the annulus which supports proper coapting of the leaflets. Mitral valve repair is still an emerging field and surgeons want to study the functional impact of surgery by visualizing echocardiographic images available as key time frames. We recompute the dynamic deformation of the mitral valve apparatus using these images which help us finding various quantifications like strain and stress maps for the leaflets etc. Hence allowing the surgeons to perform a comparative study of various quantifications for normal organic and post-operative patients and understand the impact of mitral valve repair surgery.

### 8.1.4 Mitral Valve Shape Models: From Ecocardiographic Images to Static Modeling using NURBS

#### 8.1.4.1 Acquisition of Echocardiographic 3D images and tagging by TMHRI

The 3D volumes image data are obtained via Phillips iE33 transthoracic ultrasound. Raw Phillips image data are converted to the Dicom format by Q-lab 7 ( software provided with the Phillips system). Each 3D echocardiographic movie includes 27-30 3D frames per heartbeat cycle and represents a high volume of image data corrupted by 'speckle' noise. Our group at the Dept. of Mathematics, University of Houston developed a proprietary software ITMA, built on the SLICER (version 3.4) freeware,

## 8.1. HUMAN MITRAL VALVE APPARATUS

---

dedicated to the interactive tagging of the mitral valve apparatus. The Dicom files are then read into ITMA.

The tagging was focused on four components of MVA, viewed as deformable smooth shapes in  $\mathbb{R}^3$ : the anterior and posterior leaflets  $Al$  and  $PL$ , enclosed by the fibrous ring annulus and the coaptation line along which leaflets close the valve during systole. To tag the mitral apparatus on a 3D image frame, one first identifies 1 plane PL1 "parallel" to the mitral annulus MA and 2 other planes PL2 and PL3 orthogonal to PLMA, intersecting roughly at the center of the MA. Plane PL2 is then rotated by successive small angles to span and tag the MA circumference. The anterior and posterior leaflets (AL and PL), the coaptation line, and leaflet boundaries are tagged on a second set of planes, perpendicular to plane PL1, and intersecting at the mitral-aortic continuity. These tags are stored as lists of 3D points in ITMA and automatically exported to Matlab file formats for algorithmic processing.

### 8.1.4.2 Modeling of mitral valve annulus and leaflets

The mitral leaflets and annulus are mathematically modeled by NURBS (Non-Uniform Rational B-Splines) using Matlab coded algorithms developed by [9]. 3 NURBS model are obtained, one for each leaflet and a third one for the MA.

For each patient we have roughly 40 tagging points on the mitral annulus at both MidSystole (MS) and EndSystole (ES). These tagged points are automatically ordered in a natural periodic geometric sequence. We fit a NURBS model to this ordered sequence, by simultaneous optimization of the curve smoothness and of the

accuracy of fit to the data.

Tagged points are not uniformly distributed along the MA circumference, so quadratic errors of fit are pondered by weights linked to distances between neighboring tagged points. This 1st model fitting generates errors of fit, and a 2nd fitting is implemented, with new weights based on these errors of fit. This automatic procedure generates smooth MA models with very good accuracy, which are then displayed in 3D-graphics within SLICER. For a normal patient, for each leaflet there are about 500 points tagged and transported to Matlab. Using PCA analysis a local plane is found and the points are projected on this plane. Using spline models a function  $f : \mathbb{R}^2 \rightarrow \mathbb{R}$  is generated such that the surface created by  $(x, y, f(x, y))$  approximates the leaflet with minimal errors. But for organic patients due to the prolapsing of the leaflets, the thin surface is curled in itself and hence different techniques are used to fit the models.

Due to speckle noise, manual tagging and fitting of models using minimization techniques, the *accuracy of the models is up-to one unit*.

## 8.2 Mitral Valve Apparatus as a NURBS Model

As explained about, the mitral valve models  $S_j$  are based on *NURBS* (non-uniform rational B-splines), and were obtained in [9] by combining optical flow extraction algorithms with sparse tagging by medical experts. The number  $q+1$  of intermediary key heartbeat cycle instants  $t_j$  ranged from 3 to 8, and the time range  $I = [t_0, t_1]$  covers either a half or a whole heartbeat cycle with total duration between 1/2 to 1

second.

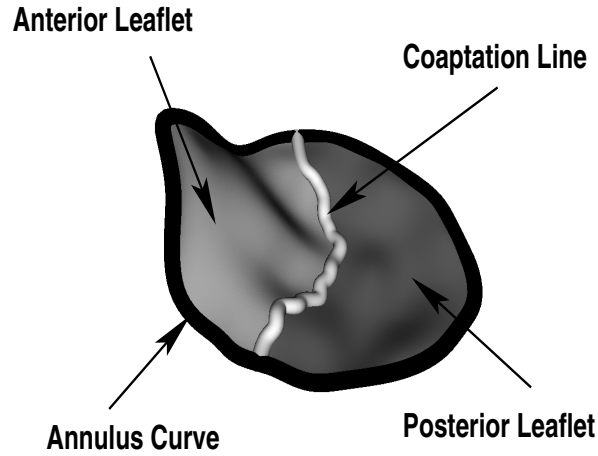


Figure 8.4: Mitral valve: the middle line is the coaptation line along which the surfaces of the anterior and posterior leaflets meet when the valve is closed. The closed black thick curve is the mitral annulus.

The mitral valve apparatus (MVA) involves the *annulus* (a closed thin deformable ring) and two deformable surfaces with boundaries, namely the *anterior and posterior leaflets*. These mitral leaflets are flexibly linked to the annulus by a subsegment of their boundaries. When the valve is closed, the exterior parts of the leaflets have a common boundary called the *coaptation line*.

The MVA can be viewed as a *composite deformable object* built from several smooth deformable shapes (see Figure 8.4), namely a closed curve MA (the mitral annulus), a curve segment COA (the coaptation line), two surfaces AL and PL (the mitral leaflets) with boundaries  $\partial AL = COA \cup \text{antMA}$  and  $\partial PL = COA \cup \text{postMA}$ , where antMA and postMA are complementary subsegments of the MA.

### 8.3 Multiple Snapshots for the Mitral Annulus and Leaflets

The given snapshots are modeled by parametrized closed curves in  $R^3$  for the mitral annulus, and by parametrized surfaces with boundaries in  $R^3$  for the anterior and posterior leaflets. The parametric equations of these curve and surface models and of their boundaries have previously been extracted from 3D-image data as indicated above, and are explicit linear combinations of cubic B-splines which are tensor products of polynomials of degree 3 in one variable restricted to bounded intervals.

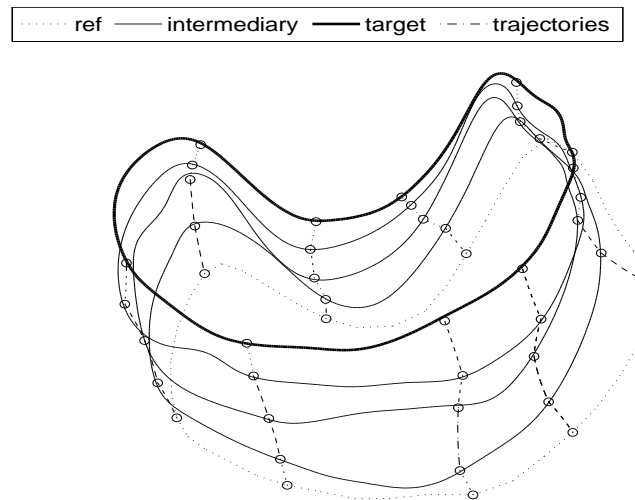


Figure 8.5: The 5 closed curves are 5 successive annulus snapshots. The dotted curve is the initial snapshot. From bottom to top, the next 3 curves are the intermediary snapshots and the last one is the final target. The vertical '—' lines are computed deformation trajectories for selected points of the reference curve.

For example for a particular patients for which we will present examples here, for

the annulus, we have 10 given snapshots, and we focus first on the 5 annulus snapshots  $A_0, A_1, A_2, A_3, A_4$  corresponding to instants  $t_0 = 1, t_1 = 3, t_2 = 5, t_3 = 7, t_4 = 10$ . The time unit, equal to  $1/27$  second, is the time interval between 2 frames.

The annulus B-spline models enable the selection of point meshes  $XA_j$  on  $A_j$  with equal arc length between successive points. The first discretizations used in the numerical implementations of continuation algorithms presented here start with 42 points for  $XA_0$ , and approximately 500 points for each one of the other  $XA_j$ .

For each mitral leaflet, 4 snapshots  $S_0, S_1, S_2, S_4$  are available at instants  $t_0 = 0, t_1 = 1, t_2 = 5, t_4 = 10$ . We discretize them by meshes for which distances between any mesh point and its closest neighbor are approximately constant. Separate discretizations are applied to the interior of the  $S_j$  and to their boundaries. For the anterior leaflet, we initially select a mesh of 126 points on the reference surface  $S_0$ , split into 84 points for its interior and 42 points on its boundary, and meshes of approximately 1600 points each on each one of the other snapshots of the anterior leaflets.

## 8.4 Diffeomorphic Matching for Multiple Annulus Snapshots

We sketch the results of optimized diffeomorphic matching for multiple annulus snapshots, first when the disparity term is the smooth Hausdorff disparity ("Hausdorff matching") as described section 6.1.2, and second when the disparity is computed by

Hilbert distances between Borel measures (“measure matching”), see equation (4.2). In both cases, we have used the continuation algorithm described in last chapter 6.2 and the trivial initialization  $\alpha = 0$  with discrete time steps  $\Delta t^\ell = 1/18$  and  $\theta = 0.3$  in the termination criterion (6.7) for gradient descent with Armijo line search. The scale parameter computed by (6.5) is  $\sigma = 3.53$  for the Gaussian kernel  $K_\sigma$ .

The computational performance of the continuation algorithm is evaluated first by the convergence history for the  $q$  indicators of the geometric matching accuracy  $\text{Dist}_j$  6.6 and for the corresponding values  $\text{Disp}_j$  of the  $q$  components of the disparity functional.

We also record and display the tradeoffs between these matching quality indicators and the kinetic energy of the corresponding deformation flows. At the end of each inner iteration of gradient descent with fixed regularization parameter  $\lambda$ , we generate a point on each one of the approximate *Pareto frontiers* displaying matching quality indicators as functions of the kinetic energy. For the global disparity term (sum of the  $q$  individual snapshot disparities  $\text{Disp}_j$ ), we expect and empirically observe convexity of these approximate Pareto frontiers, viewed as usual as the location of the weak Pareto optima for the pair of competing criteria (kinetic energy versus matching disparity) (cf., e.g., [18]).

### 8.4.1 Smoothed Hausdorff Matching for Multiple Annulus Snapshots.

The initial value  $\lambda^{(0)} = 1$  of the regularization parameter is increased at each outer iteration by the multiplicative factor  $\gamma = 1.1$  (cf. (6.9)). The convergence history is documented in Figure 8.6 which displays the decrease of the geometric accuracy indicators  $\text{Dist}_j$  and of the disparity components  $\text{Disp}_j$  for our 4 snapshots  $A_j, 1 \leq j \leq 4$ . It takes 200 iterations to reach the threshold geometric accuracy required for this application (see (6.8) ), but we have extended iterations beyond this value to obtain a more complete view of the Pareto frontiers.

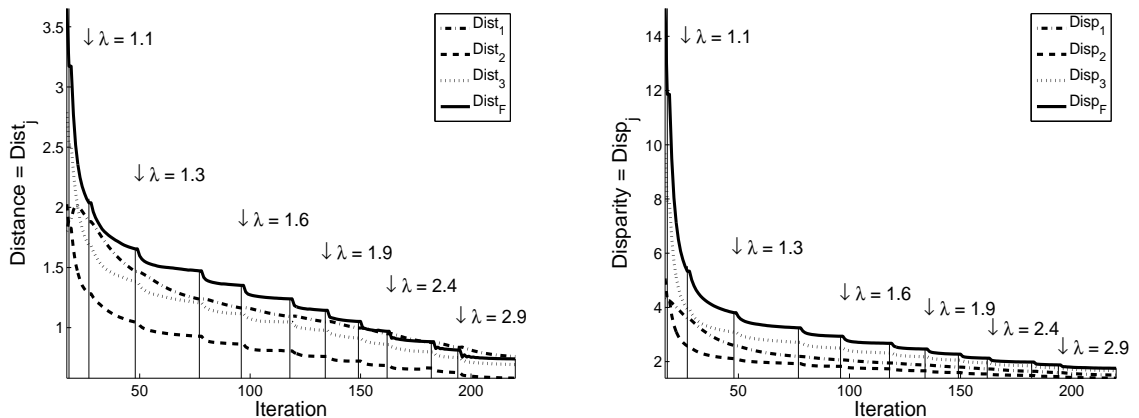


Figure 8.6: Diffeomorphic matching for multiple mitral annulus snapshots, using smoothed Hausdorff distances: Convergence history for the geometric accuracy indicators  $\text{Dist}_j$  and for the smoothed Hausdorff disparity components  $\text{Disp}_j$ .

The Pareto frontiers for the geometric accuracy indicators  $\text{Dist}_j$ , the Hausdorff

disparities  $\text{Disp}_j$ , and the global Hausdorff disparity  $\sum_j \text{Disp}_j$  are shown in Figure 8.7. Note that for the first annulus snapshot the geometric accuracy  $\text{Dist}_1$  and the Hausdorff disparity  $\text{Disp}_1$  do not exhibit a convex decrease pattern at the beginning of the continuation procedure. Indeed, the implemented algorithmic optimization strategy first "focuses" on matching the final snapshot  $A_4$  and then successively shifts the focus on the matching of the intermediary snapshots  $A_3, A_2, A_1$  in decreasing order. This is due to the fact that in the backwards adjoint ODE, the snapshots matching errors kick in successively in the same reverse order. Hence, as long as the final snapshots errors are large, the corrections implemented for the first snapshots remain quite fuzzy, and only turn out to be efficient once the matching errors on the final snapshots have become small enough.

#### **8.4.2 Diffeomorphic Matching for Multiple Annulus Snapshots: Measure Matching.**

Here, the disparity terms are the squared Hilbert distances between measures. The regularization parameter  $\lambda$  starts at  $\lambda^{(0)} = 200$  and is multiplied by  $\gamma = 2$  at each outer iteration. Figure 8.8 displays the corresponding convergence history for 4 individual geometric accuracy indicators and 4 measure matching disparities. The desired threshold geometric accuracy is achieved for all snapshots after 70 iterations. But the computing time for each iteration is about 3 times higher than for Hausdorff

### 8.4. DIFFEOMORPHIC MATCHING FOR MULTIPLE ANNULUS SNAPSHOTS

---

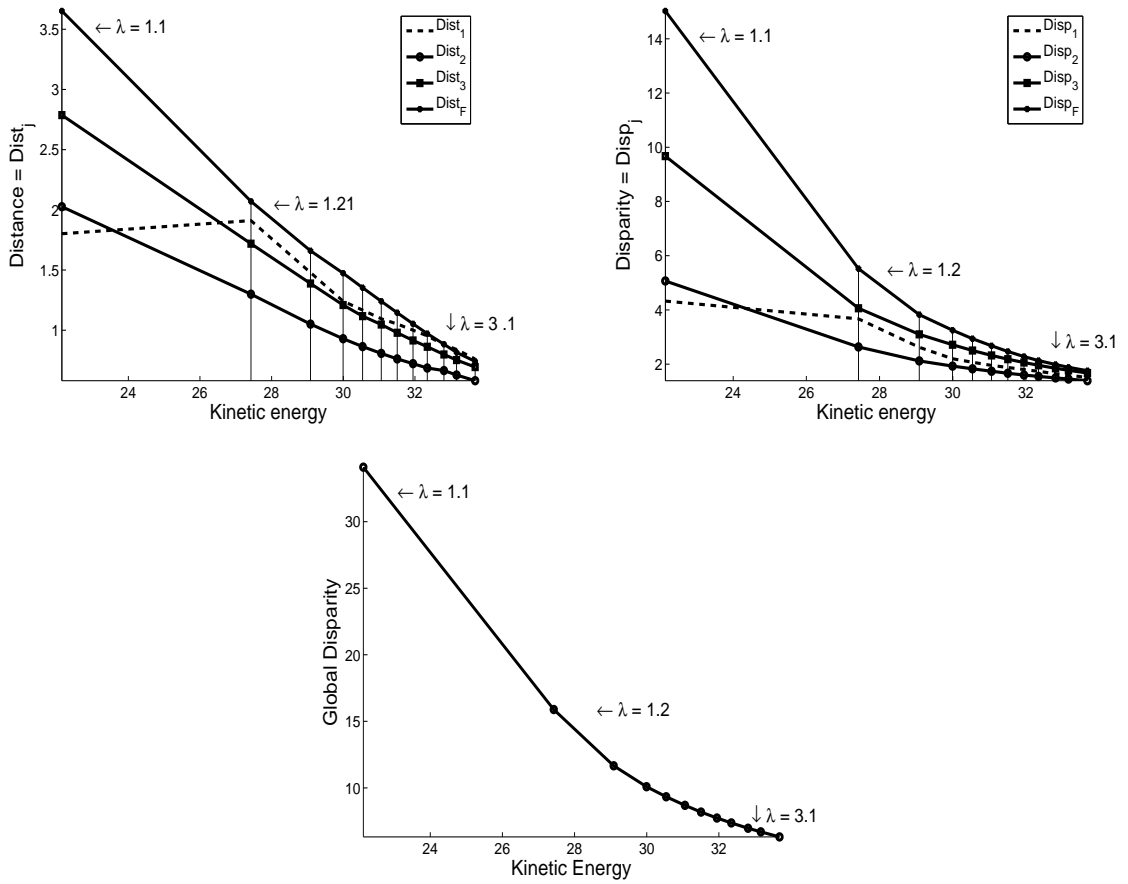


Figure 8.7: Diffeomorphic matching for multiple annulus snapshots, using smoothed Hausdorff distances: Pareto frontiers for the geometric accuracy indicators  $\text{Dist}_j$  (top left), for the Hausdorff disparities  $\text{Disp}_j$  (top right), and for the global Hausdorff disparity  $\sum_j \text{Disp}_j$  (bottom).

#### 8.4. DIFFEOMORPHIC MATCHING FOR MULTIPLE ANNULUS SNAPSHOTS

---

matching, due to the fact that measure matching invokes large numbers of evaluations of exponentials. This unfavorable computational feature of measure matching with respect to Hausdorff is quickly amplified when the number  $N_0$  of trajectories increases.

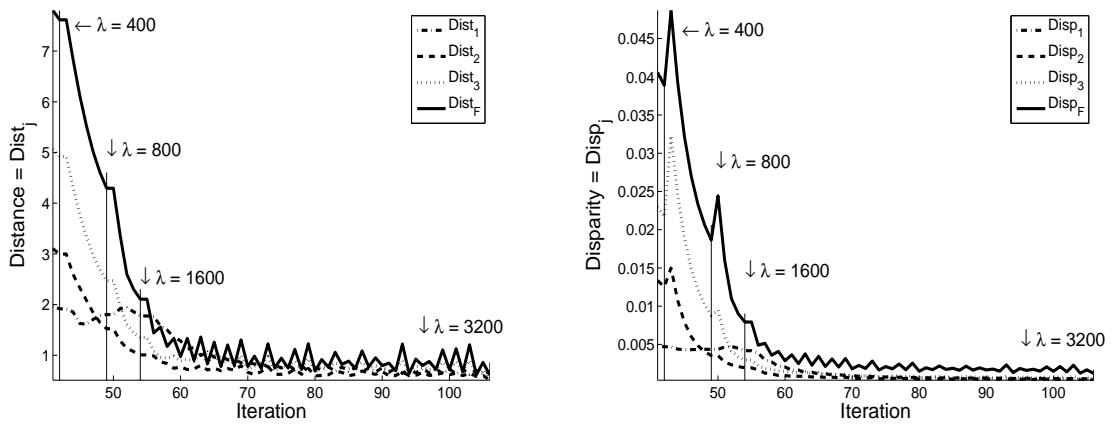


Figure 8.8: Diffeomorphic matching for multiple annulus snapshots, using measure matching disparities: Convergence history for the individual geometric accuracy indicators  $\text{Dist}_j$  (left) and the measure matching disparities  $\text{Disp}_j$  (right).

The corresponding Pareto frontiers are shown in Figure 8.9. As in the case of Hausdorff matching, and for the same algorithmic reasons, the performance indicators improve first for the final snapshots and the improvements successively kick in for the other snapshots in reverse order of the snapshot times  $t_j$ . Comparing Figures 8.9 and 8.7, we see that for a given geometric matching accuracy, the achievable kinetic energy remains higher for measure matching than for smoothed Hausdorff matching.

### 8.4. DIFFEOMORPHIC MATCHING FOR MULTIPLE ANNULUS SNAPSHOTS

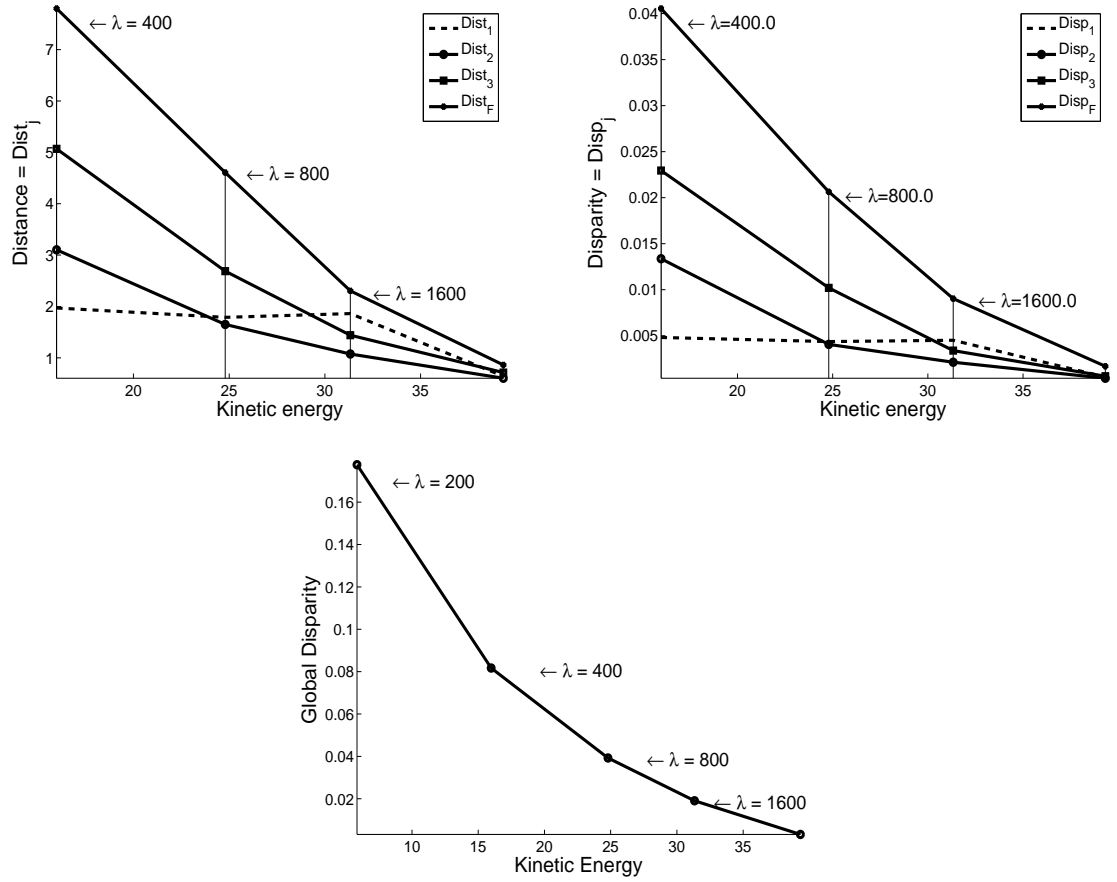


Figure 8.9: Diffeomorphic matching for multiple annulus snapshots using measure matching disparities: Pareto frontiers for the geometric accuracy indicators  $\text{Dist}_j$  (top left), for the individual measure matching disparities  $\text{Disp}_j$  (top right), and for the global measure matching disparity  $\sum_j \text{Disp}_j$  (bottom).

### 8.4.3 Diffeomorphic Matching for 10 Annulus Snapshots

We consider here the 10 annulus snapshots  $A_j, 0 \leq j \leq 10$ , acquired at times  $0, 1, 3, 5, 7, 10, 14, 18, 22, 26$ . We choose 42 points on the reference  $A_0$  and approximately 500 points on the other snapshots. We use the smoothed Hausdorff disparity (2.15). We initialize  $\alpha$  by  $\alpha = 0$ , and use 52 discretized time steps. The parameters  $\theta, \sigma, \rho$  are the same as above.

Since good matching accuracy for the first snapshots now takes a longer time (see Figure 8.10), we perform continuation with different weights  $\lambda_j$  for the individual Hausdorff disparities  $\text{Disp}_j$ , adjusted to dynamically balance the current average sizes of these distinct disparities (cf. Figures 8.11). Since we dynamically change the global disparity functional, we cannot expect to have nice convex Pareto frontiers (cf. Figure 8.11).

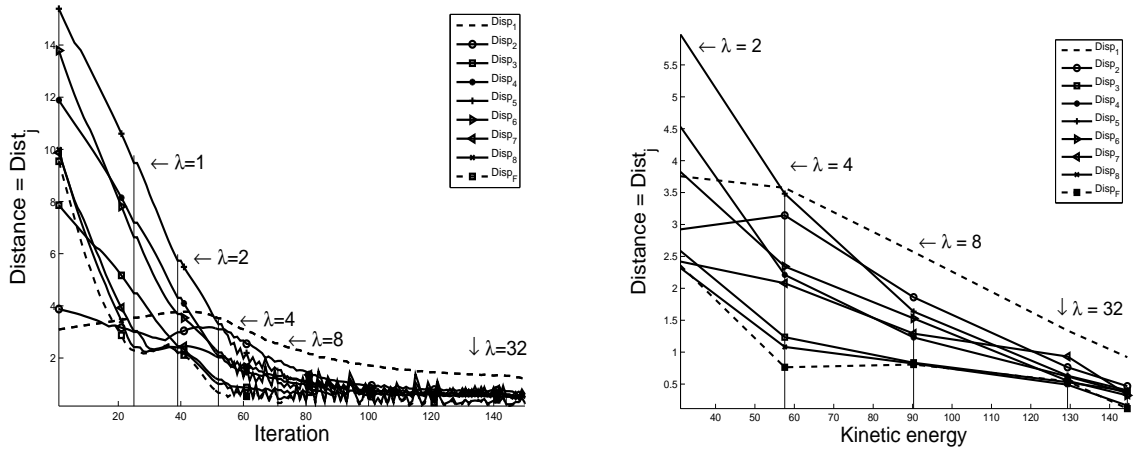


Figure 8.10: Diffeomorphic matching for ten annulus snapshots using Hausdorff disparities: Convergence history of geometric accuracies (left) and corresponding Pareto frontiers (right) using a single regularization parameter  $\lambda$  for the nine Hausdorff disparities.

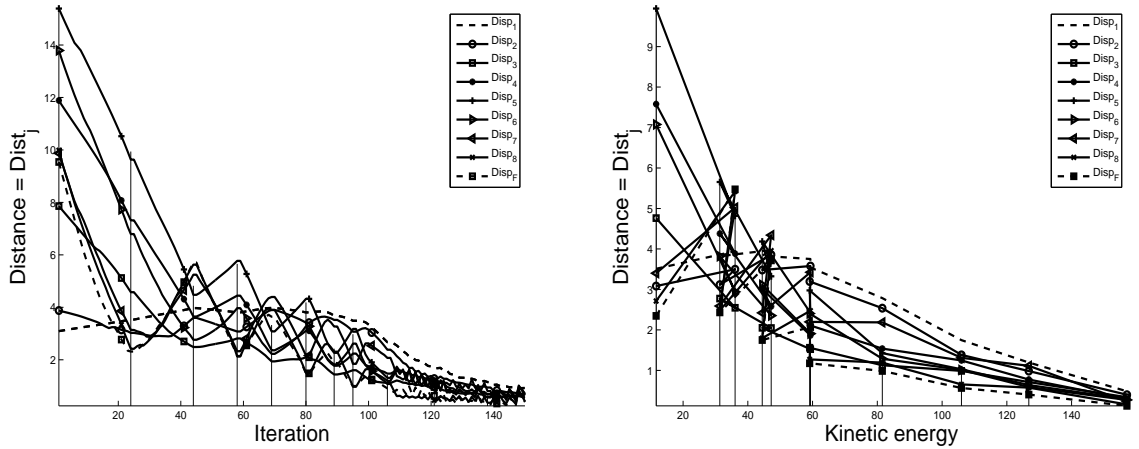


Figure 8.11: Diffeomorphic matching for ten annulus snapshots: Convergence history of the geometric accuracies (left) and corresponding Pareto frontiers (right) using nine dynamic regularization parameters  $\lambda_j$ .

## 8.5 Diffeomorphic Matching of the Anterior Leaflet

We present the performances of diffeomorphic matching for 4 snapshots  $S_0, S_1, S_2, S_3$  of the anterior leaflet, acquired at times 0, 1, 5, 10, using smoothed Hausdorff snapshot disparities, where the disparities are separately computed for the boundary and the interior of each snapshot as outlined in 6.1.2. Indeed, initial experiments where this distinction was not implemented quickly displayed much poorer performances. Rough initial discretization starts with point meshes of cardinals 400 for  $S_0$  and roughly equal to 1700 for  $S_1$  and  $S_2$ .

The continuation algorithm starts with  $\lambda = 0.1$ , and  $\lambda$  is multiplied by  $\gamma = 1.5$  at each outer iteration. The scale and termination parameters  $\sigma$  and  $\theta$  are as above.

The following Figures 8.12 and 8.13 display satisfactory performance results.

We display in Figure 8.14 a visualization of the computed deformations of the

## 8.5. DIFFEOMORPHIC MATCHING OF THE ANTERIOR LEAFLET

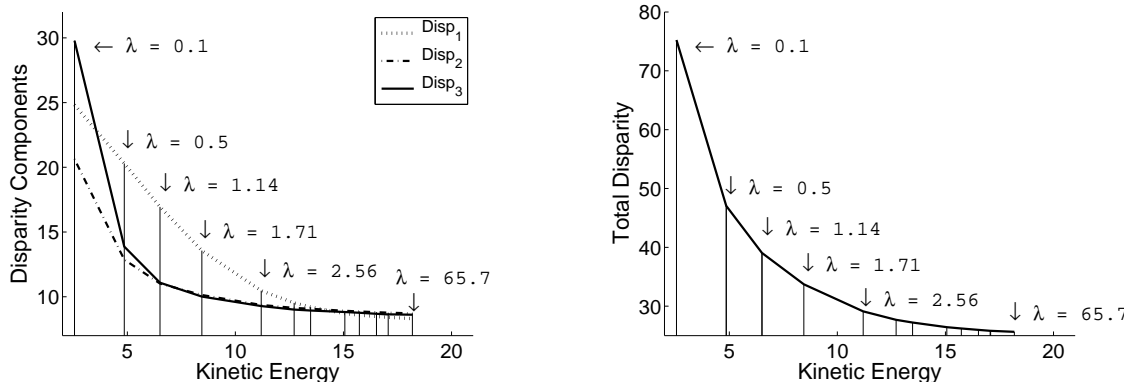


Figure 8.12: Diffeomorphic matching of four anterior leaflet snapshots: Pareto frontiers for the separate Hausdorff disparities to snapshots (left) and for the global Hausdorff disparity (right).

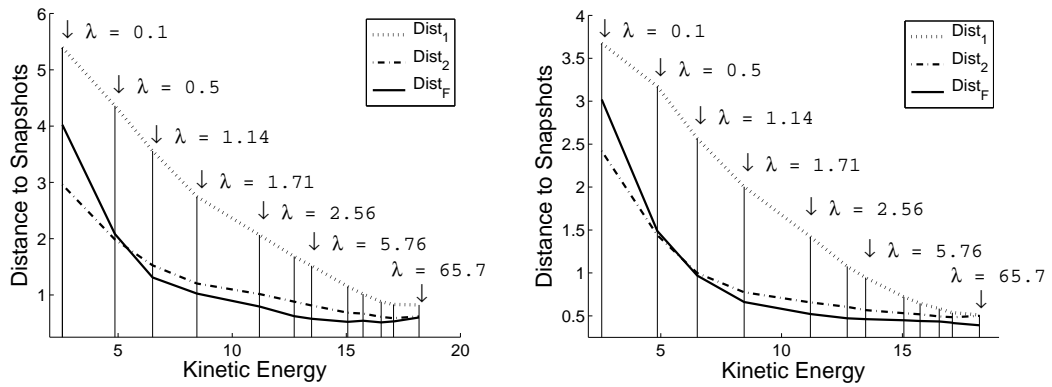


Figure 8.13: Pareto frontiers for the maximum distances to snapshots (left) and for their 90th percentiles (right).

### 8.5. DIFFEOMORPHIC MATCHING OF THE ANTERIOR LEAFLET

---

anterior leaflet at the 4 snapshot times 0, 1, 5, 10. The corresponding dynamic deformations of the anterior leaflet boundary are presented in Figure 8.15. A few deformation trajectories are indicated. They are computed as solutions of the dynamics equations (2.4).

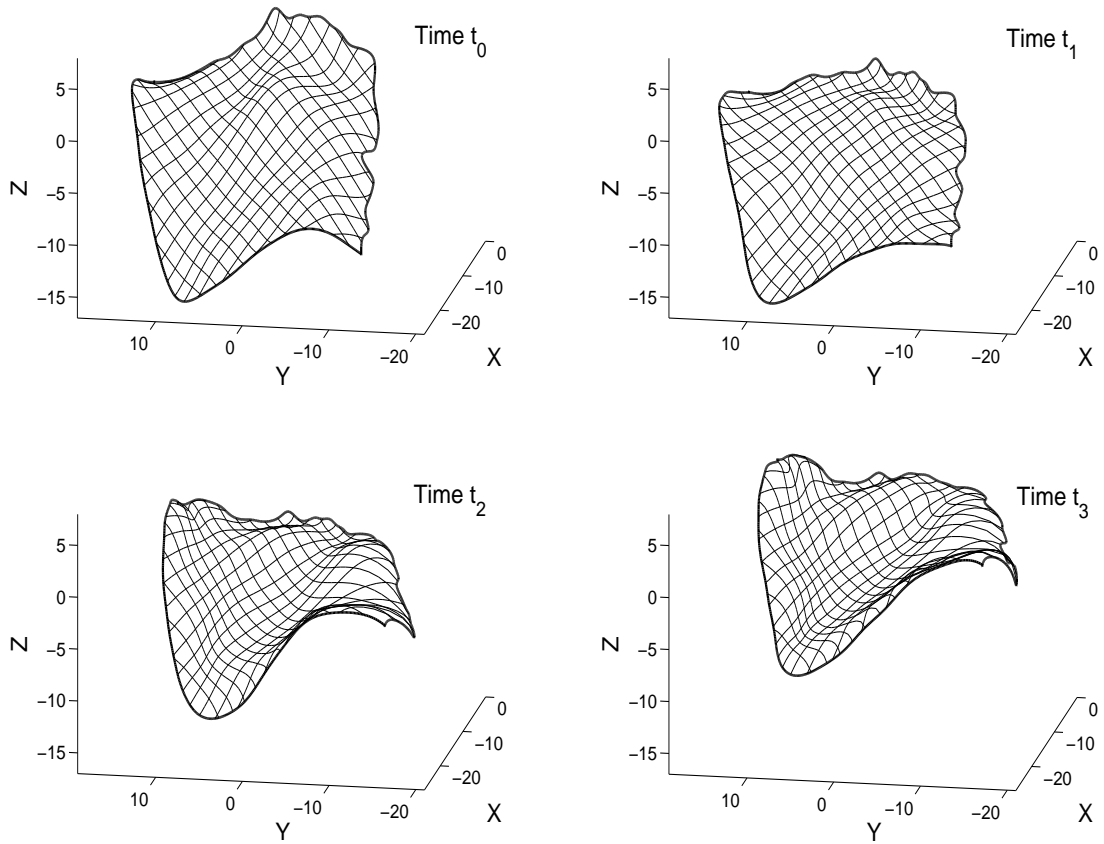


Figure 8.14: Computed deformations matching four snapshots of the anterior leaflet at instants 0, 1, 5, 10 .

For each computed deformation  $\hat{S}_j$  of the initial snapshot  $S_0$ , the three graphs in Figure 8.16 display several level curves for the point matching errors between  $\hat{S}_j$

## 8.5. DIFFEOMORPHIC MATCHING OF THE ANTERIOR LEAFLET

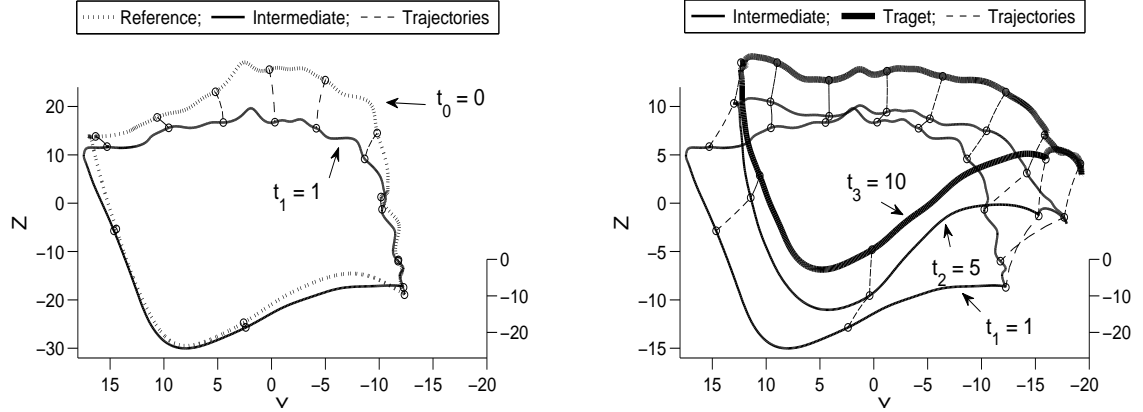


Figure 8.15: Computed deformations of the anterior leaflet boundary: for easier visualization, the boundary deformations are displayed separately for instants 0, 1 and for instants 1, 5, 10.

and the given anterior leaflets snapshots  $S_j$ . The coordinate system has been modified isometrically at each snapshot instant in order to display a better "horizontal" projection of  $\hat{S}_j$ .

8.5. DIFFEOMORPHIC MATCHING OF THE ANTERIOR LEAFLET

---

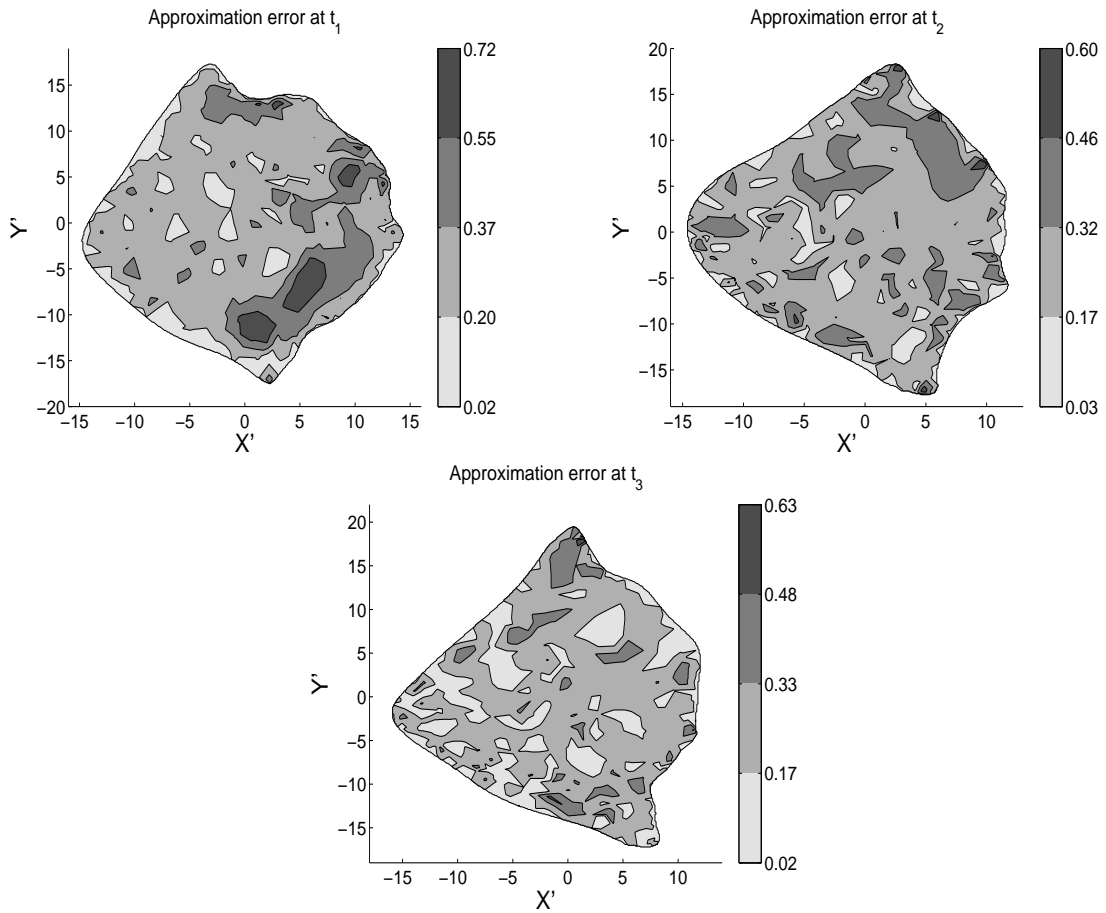


Figure 8.16: Matching errors between the computed anterior leaflet deformations  $\hat{S}_j$  and the snapshots  $S_j$ .

## 8.6 Diffeomorphic Matching for Multiple Snapshots of the Posterior Leaflet

We have similarly implemented the diffeomorphic matching for 4 snapshots  $S_0, S_1, S_2, S_3$  of the posterior leaflet acquired at times 0, 1, 5, 10, using smoothed Hausdorff snapshot disparities, with disparities separately computed for the surface boundary and the interior as outlined in 6.1.2. Time is discretized into 30 equal intervals. The 4 snapshots are discretized by point meshes of approximate cardinals 250 for the initial leaflet  $S_0$ , and 1100 for the other snapshots.

The initialization and the choice of the algorithmic parameters are similar to the implementation just described for the anterior leaflet (cf. 8.5). As already noted above, when one uses the same value  $\lambda$  for all 3 regularization weights  $\lambda_j$ , the matching quality between  $S_j$  and  $\hat{S}_j$  improves more slowly for  $j = 1$  than for  $j = 3$  (see Figure 8.17). We have compared this approach to a more adaptive one, where one dynamically adjusts the weights  $\lambda_j$  at each outer iteration by appropriately balancing current values of the 3 Hausdorff disparities (cf. Figure 8.18). The geometric matching accuracies reach a desirable pragmatic threshold slightly faster for the dynamically independent weights, at the cost of some loss of convexity for the Pareto frontiers, which suggests that dynamic adjustment of weights may provide less robustness in the continuation procedure.

Figure 8.19 displays the computed deformations of the posterior leaflet at the 4 instants 1, 4, 16, 31. The computed dynamic deformations of the posterior leaflet

8.6. *DIFFEOMORPHIC MATCHING FOR MULTIPLE SNAPSHOTS OF THE POSTERIOR LEAFLET*

---

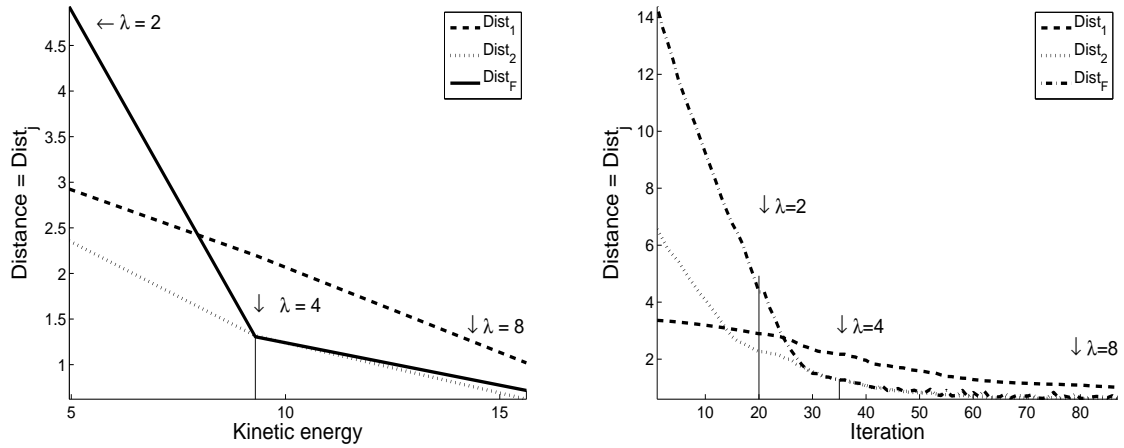


Figure 8.17: Diffeomorphic matching for four posterior leaflet snapshots: Geometric accuracy indicators and Pareto frontiers for strictly equal regularization weights  $\lambda_j$ .

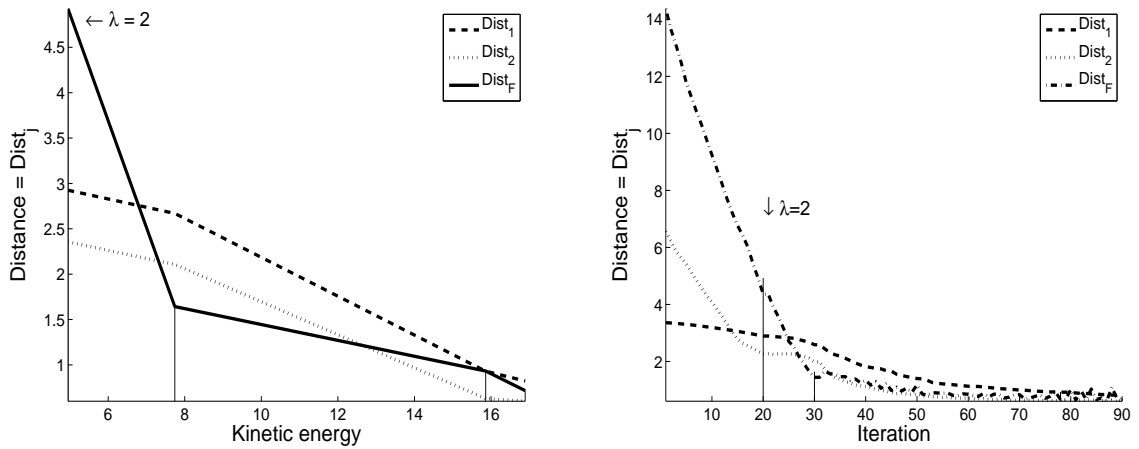


Figure 8.18: Diffeomorphic matching for four posterior leaflet snapshots: Geometric accuracy indicators and Pareto frontiers for dynamically adjusted regularization weights  $\lambda_j$ .

## 8.6. DIFFEOMORPHIC MATCHING FOR MULTIPLE SNAPSHOTS OF THE POSTERIOR LEAFLET

---

boundary are presented in Figure 8.20 with a few deformation trajectories.

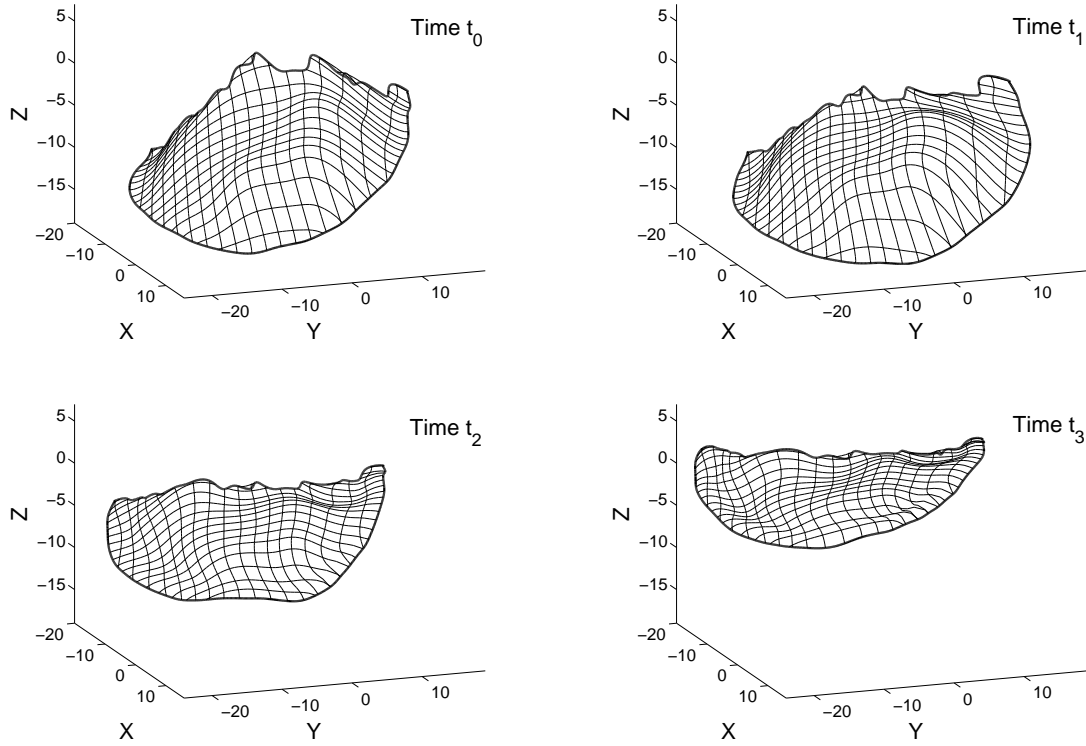


Figure 8.19: Computed deformations matching four snapshots of the posterior leaflet at instants 0, 1, 5, 10.

Figure 8.16 displays point matching errors between computed deformations  $\hat{S}_j$  of the posterior leaflet and the given snapshots  $S_j$ . The coordinate system is modified isometrically for each computed deformation  $\hat{S}_j$  to display a good "horizontal" projection of  $\hat{S}_j$ .

## 8.6. DIFFEOMORPHIC MATCHING FOR MULTIPLE SNAPSHOTS OF THE POSTERIOR LEAFLET

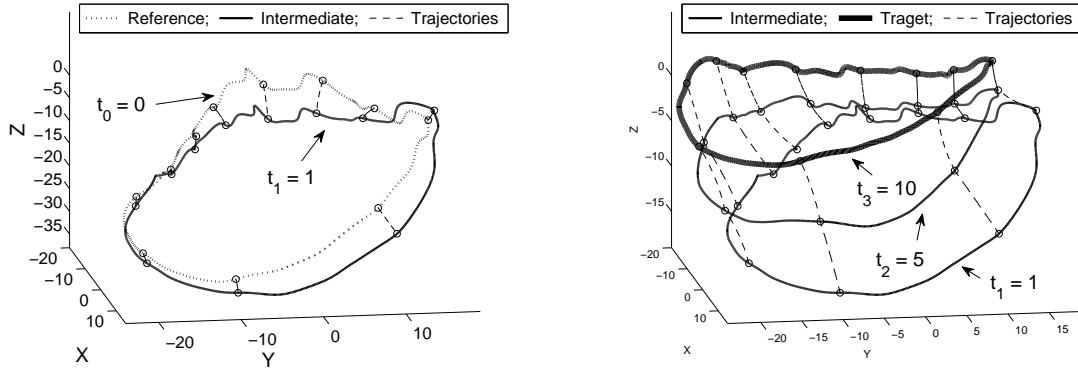


Figure 8.20: Computed deformations of the posterior leaflet boundary: the continuous boundary deformations are displayed separately for instants 0, 1 and for instants 1, 5, 10.

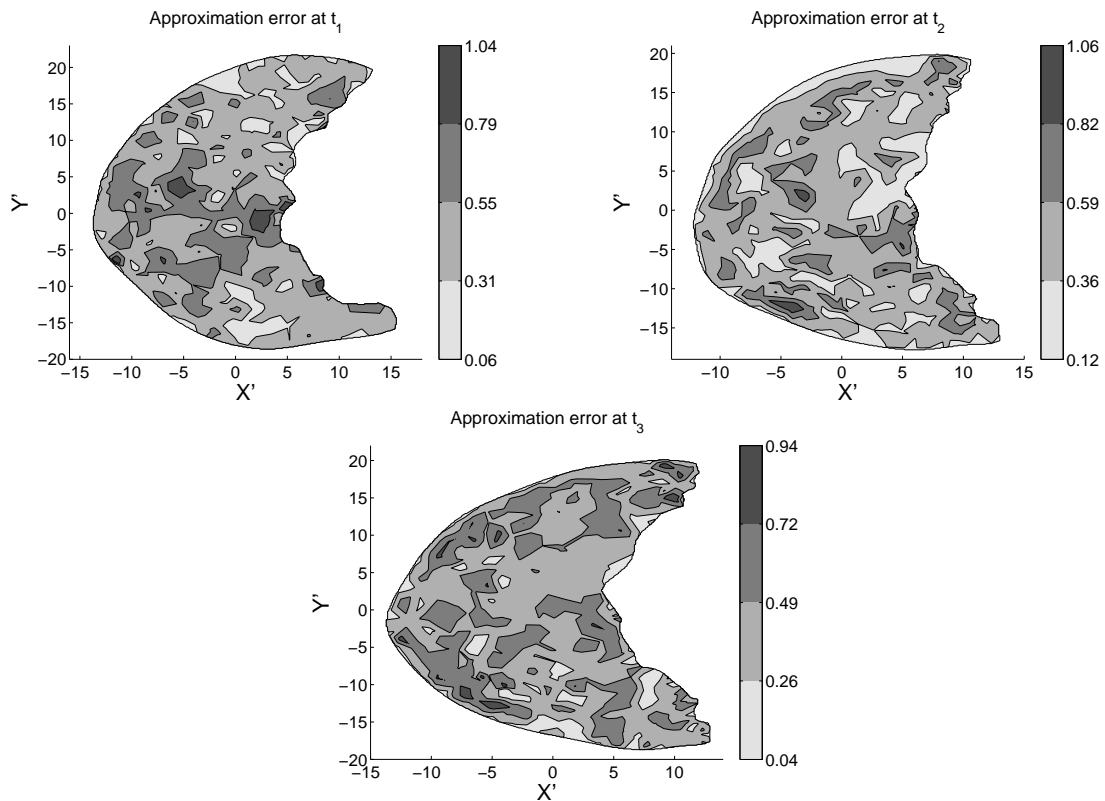


Figure 8.21: Matching errors between the computed posterior leaflet deformations  $\hat{S}_j$  and the snapshots  $S_j$ .

## 8.7 Diffeomorphic Matching of the Whole Mitral Valve Apparatus

We now compute diffeomorphic deformations of the whole mitral valve apparatus ("MVA") viewed as one single *composite deformable object* as introduced above. We apply the diffeomorphic matching algorithms outlined above to 3 given MVA snapshots  $MVA_0, MVA_1, MVA_2$ , acquired at instants 1, 5, 10. Our discretization meshes involve roughly 150 points each for the initial anterior leaflet  $AL_0$  and posterior leaflet  $PL_0$ , and respectively 3200 and 1700 points each for the anterior and posterior leaflets snapshots  $AL_1, PL_1, AL_2, PL_2$ . The smoothed Hausdorff disparities involve several disparity terms for each one of the given MVA snapshots  $MVA_1$  and  $MVA_2$ , quantifying separately the disparities between AL surfaces, PL surfaces, annulus curves, and coaptation lines. We initialize  $\alpha$  by  $\alpha = 0$ . All the choices of parameter values driving the continuation algorithm are identical to the choices made above to compute deformations of the anterior leaflet (see 8.5).

## CONCLUSIONS

---

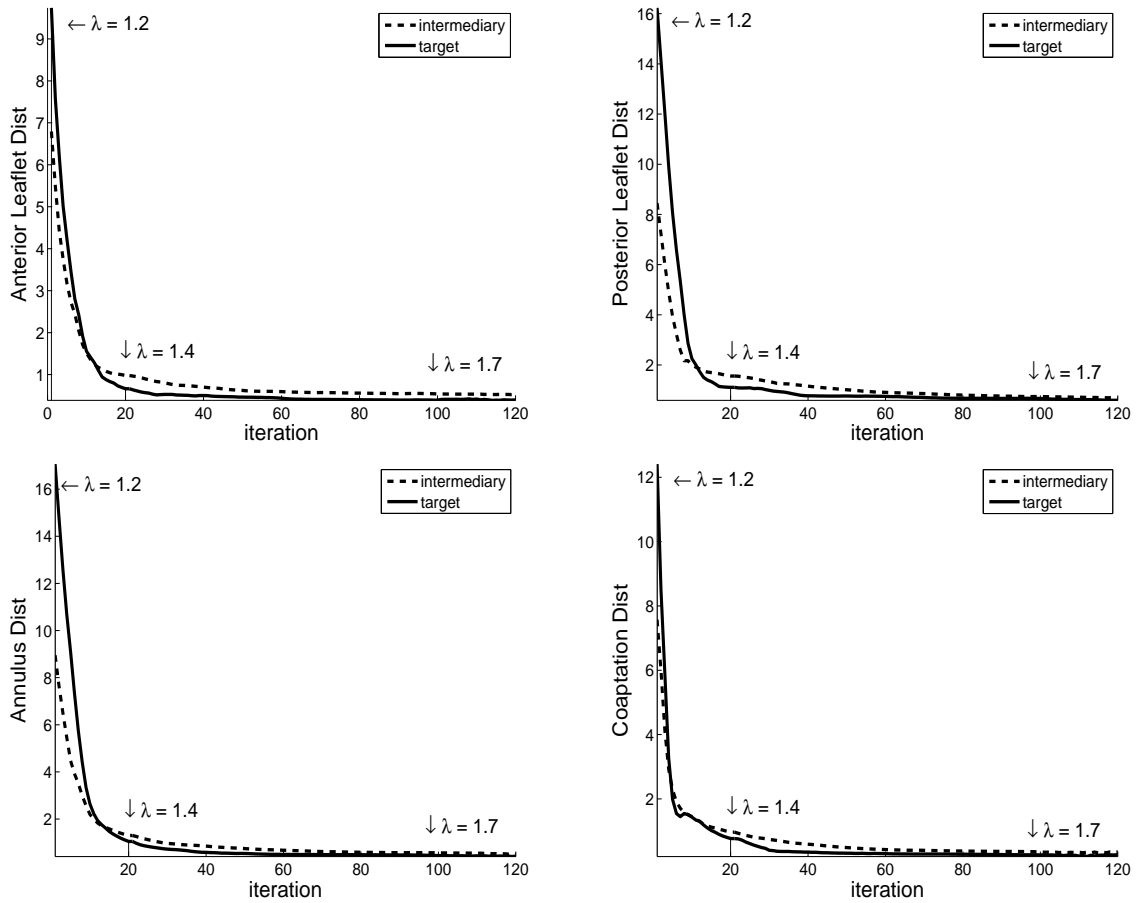


Figure 8.22: Diffeomorphic matching of the whole Mitral Valve Apparatus: Convergence history for the geometric matching accuracy.

## CHAPTER 9

---

### Conclusions and Future Work

---

In this thesis, we have focused on finding optimal matching for multiple sub-manifolds in  $\mathbb{R}^3$ . Given an arbitrary number of snapshots  $S_{t_j}, j = 0 \dots q$ , of a deforming object available at time instances  $t_0 < t_1 \dots < t_q$  while in motion, our goal is to obtain a time dependent diffeomorphism  $F_t$  which can regenerate the motion of the object. We use a variational approach pioneered by Grenander et al. in the context of pattern recognition and further explored by Dupuis, Miller, Mumford, Trouné, Younes et. al. focusing mainly on comparing shapes. However, the key difference here is that we extend the existing framework to multiple snapshots in order to

## CONCLUSIONS

---

recover the full motion. Akin to their work, we restrict our search for time dependent diffeomorphisms to the solution of non linear differential equations associated with time dependent vector fields belonging to a certain class of Hilbert spaces [23]. Further, due to various computational advantages of using a Reproducing Kernel Hilbert Space (RKHS) as experienced in the past, we work with RKHS associated with Gaussian kernels. We formally introduce the variational problem in the infinite dimensional setting where the objective functional consists of two terms: the first term features functions quantifying disparities between the deformed shape and the associated available shape so that the reconstructed motion of the dynamic shape is close to the original deformation of the shape, and the second term is a regularizing energy term. In the description of the former term, the word 'close' is relative to the context, i.e., a suitable disparity function or a union of disparity functions can be used to achieve the desired standards of closeness. Chapters 3-5 are then dedicated to prove the existence of an optimal solution and to derive the necessary optimality conditions in the infinite dimensional case followed by the semi-discrete system (in spatial domain), and finally the fully discrete system (in spatial and time domain) so as to make it numerically accessible. The optimality conditions comprise coupled dynamical systems with a state equation forward in time and an adjoint state equation backward in time as well as the gradient of the objective functional with respect to the control variable. We observe that due to the fact that disparity functionals depend on various time instances, the lack of smoothness of the solution of the adjoint state equations results in non-smooth transitions of the solution in time. Hence, we introduce a smoothing term involving first-order derivatives of the control variable

## CONCLUSIONS

---

in time as part of the objective functional and present numerical results to illustrate the benefits of this approach.

As an application to the model developed in the thesis, we reconstruct the deformation of the mitral valve apparatus between the available snapshots. The mitral valve apparatus comprises two thin leaflets and a fibrous ring called annulus. The annulus serves as a 1-D sub-manifold matching problem, whereas the leaflets represent 2-D manifold matching cases. We also show that it is possible to deform all these parts of the mitral valve leaflet as one object and hence to reconstruct the deformation of the MVA between available snapshots.

In this thesis, we have used first order optimality conditions to obtain the optimal solution of the control problem. However, it is well known that using second order information can lead to faster iterative methods. We further plan to apply Newton's method to the optimality conditions in terms of a *predictor-corrector method* based on [58, 59] featuring an adaptive choice of the continuation parameter [1, 40].

*Multiscale diffeomorphic point matching.* In various practical applications, one often encounters deformable objects with complex structures. It is preferable to use a finer mesh in order to precisely capture the local properties of the object, e.g., in the application presented in the thesis concerning the deformation of the mitral valve apparatus, a higher Gaussian curvature is observed for the leaflets associated with organic patients. But increasing the size of the mesh points is computationally challenging. One of the obvious remedies is to take advantage of multiscaling techniques, and the other is to use a non uniform mesh size, i.e., choosing finer points in the respective regions. However, due to the high dependency of the scale parameter

## CONCLUSIONS

---

$\sigma$  on the resolution of the mesh size, the transition between different levels of meshes demands an adapted multiscale algorithm to deal with the choice of new continuation parameters and initialization techniques to move to a finer mesh.

*Additional matching requirements.* One of the advantages of the present algorithms is that it can accommodate a wide range of matching requirements. For example, for MVA applications the shapes of various parts of the MVA are extracted using echocardiographic images and hence, at each snapshot we also have intensity information available. In order to obtain more precise matching, one can add an intensity matching term to the objective functional. Since the available intensity functions are discrete functions, one can use standard interpolation techniques to obtain an intensity functional defined on an open set of  $\mathbb{R}^3$ . Experiments concerning curve matching with additional terms as intensity matching have already been implemented by our group with successful results. We further plan to analyze the effect of intensity matching in the context of surfaces. A study done in the group shows that image matching disparity evaluated for deformed shapes obtained by solving the original system itself is small. Hence, we expect that adding this will further help the system to converge faster and give more precise results. Another aspect of these elastic deformations is to study the amount of spatial stretch during the deformation. Depending on the requirement of the application, one can use *bending energy* terms as well to restrict large spatial deformations [26].

---

## Bibliography

---

- [1] H Antil, R. H.W. Hoppe and C. Linsenmann 1 *Adaptive Multilevel Interior-Point Methods in PDE Constrained Optimization Journal of Numerical Mathematics* 2007 **15**(2):81-100
- [2] N. Arad, N. Dyn, D. Reisfeld, and Y. Yeshurun, Image warping: application to facial expressions, *CVGIP: Graphical Models and Image Proc.*, **56** (1994), pp. 161–172.
- [3] L. Armijo, Minimization of functions having Lipschitz continuous first partial derivatives, *Pacific J. Math.*, **16** (1966), pp. 1–3.
- [4] V.I. Arnold, Sur la géométrie différentielle des groupes de Lie de dimension infinie et ses applications à l'hydrodynamique des fluides parfaits, *Ann. Inst. Fourier (Grenoble)*, **1** (1966), pp. 319–361.
- [5] V.I. Arnold, Ordinary Differential Equations *Springer-Verlag*
- [6] N. Aronszajn, Theory of reproducing kernels, *Trans. Amer. Math. Soc.*, **68**, 337–404, 1950.
- [7] R. Azencott, Elastic deformations of soft 3D-shapes, *IBIS Colloquium on Medical image analysis. The Methodist Hospital, Kiawah Island, 2006*
- [8] R. Azencott, R. Glowinski, and A. Ramos, A controllability approach to shape identification, *Applied Math. Letters* **21** (2008), pp. 861–865.

## BIBLIOGRAPHY

---

- [9] R. Azencott, S. Alexander, A. Aggarwaal, A. Jajoo, S. Jain, Y. Li, S. BenZekry (MD), S.H. Little (MD), W. Zoghbi (MD), New parameters to compare Mitral Annulus shapes extracted from 3D-echocardiography, *submitted*, 2010
- [10] R Azencott, Roland Glowinski, Jiwen He, Ronald H. W. Hoppe, Aarti Jajoo, Yipeng Li, Andrey Martynenko, Sagit Benzekry, Stephen H. Little, William A. Zoghbi, Diffeomorphic matching and dynamic deformable surfaces in 3D medical imaging, *Comput. Meth. in Appl. Math.* 10, pages 235-274, 2010
- [11] R Azencott, A Jajoo, S Jain, J He, Y Li, A Martynenko, S Ben Zerky MD, G Lawrie MD, S H Little, W A Zogbhi MD Comparitive evaluation of Mitral Valve Starin by deformation tracking in 3D-Echocardiography *IEEE*,*submitted*, 2010
- [12] M.F. Beg, M.I. Miller, A. Trouvé, and L. Younes, Computing large deformations metric mappings via geodesic flows of diffeomorphisms, *Int.J. Comp. Vis.*, **61**(2005), pp 139–157.
- [13] L Bookstein Morphometric tools for landmark data: geometry and biolody, Cambridge University Press, 1991
- [14] F. L. Bookstein. Landmark methods for forms without landmarks: morphometrics of group differences in outline shape, *Medical Image Analysis*, 1:225-243, 1996.
- [15] F. L. Bookstein. Biometrics, biomathematics and the morphometric synthesis, *Bulletin of Mathematical Biology*, 1996.
- [16] L. G. Brown, A survey on image registration techniques, *ACM Computing Surveys*, **24** (1992), pp. 326–376.
- [17] Y. Cao, M. I. Miller, R. Winslow, and L. Younes, Large deformation metric mapping of vector fields, *IEEE Trans. Med. Imaging*, **24** (2005), pp. 1216–1230.
- [18] A. Chinchuluun, P.M. Pardalos, A. Migdalas, and L. Pitsoulis (eds.), Pareto Optimality, Game Theory and Equilibria, *Springer, Berlin-Heidelberg-New York*, 2008.
- [19] H. Chui and A. Rangarajan, A new point matching algorithm for non-rigid registration, *Computer Vision and Understanding*, **89** (2003), pp. 114–141.
- [20] M.Chupin, D. Hasboun, S. Baillet, and altri, Competitive segmentation of the hippocampus and volumetry in Alzheimer disease, *In: 10th meeting of the Organization for Human Brain Mapping*, 2004.

## BIBLIOGRAPHY

---

- [21] J.M. Coron, Control and Nonlinearity, *Math. Surveys and Monographs*, Vol. 136, American Mathematical Society, Providence, 2007.
- [22] N. Dyn, Interpolation and approximation by radial and related functions, *Approximation theory VI: vol. 1*, 1989
- [23] P. Dupuis, U. Grenander, and M. I. Miller, Variational problems on flows of diffeomorphisms for image matching, *Quart. Appl. Math.*, **56** (1998), pp. 587–600.
- [24] H. Drury, D.V. Essen, M. Corbetta, and A. Snyder, Surface based analysis of human cerebral cortex, *In: Brain Warping*, 337–363, Academic Press, 1999.
- [25] A. Elen, H. F. Choi, D. Loeckx, H. Gao, P. Claus, P. Suetens, F. Maes, and J. Dhooge, Three-dimensional cardiac strain estimation using spatio-temporal elastic Registration of Ultrasound Images, *IEEE Trans Med Imaging*, 27(11):15801591, 2008
- [26] T. Franke, R. Hoppe, C. Linsenmann, L. Schmid, C. Willbold, A. Wixforth, Numerical simulation of the motion and deformation of red blood cells in microchannels Computing and Science Visualization, Springer
- [27] L. Greengard, and J Strain, *Fast Gauss transform*, SIAM Jour. Sci. Stat. Comp., **12** (1991), pp. 79–94.
- [28] J. Glaunès, *Transport par difféomorphismes de points, de mesures et de courants pour la comparaison des formes et l’anatomie numérique*, PhD Thesis, Université Paris 13, 2005.
- [29] J. Glaunès, A. Trounev and L. Younes *In: Modeling Planar Shape Variation via Hamiltonian Flows of Curves*, Statistics and Analysis of Shapes. Krim H, Yezzi A, editors. Birkhauser, 2006
- [30] J. Glaunès, A. Qiu, M.I. Miller, and L. Younes, *Large deformation diffeomorphic metric curve mapping*, *Int. J. Comp. Vision*, **80** (2008), pp. 317–336.
- [31] J. Glaunès, A. Trounev, and L. Younes, *Diffeomorphic matching of distributions: A new approach for unlabelled point-sets and sub-manifolds matching*, in: *2004 IEEE Computer Society Conference on Computer Vision and Pattern Recognition (CVPR’04)*, Vol. 2, IEEE Computer Society, Washington, DC, 2004, pp. 712–718.

## BIBLIOGRAPHY

---

- [32] J. Glaunès, M. Vaillant, and M. I. Miller, *Landmark matching via large deformation diffeomorphisms on the sphere*, J. Math. Imaging Vis., **20** (2003), pp. 179–200.
- [33] R. Glowinski, J.L. Lions, and J. He; *Exact and Approximate Controllability for Distributed Parameter Systems: A Numerical Approach*, Cambridge University Press, Cambridge, 2008.
- [34] H. Guo, A. Rangarajan, S. Joshi, and L. Younes, *Non-rigid registration of shapes via diffeomorphic point matching*, in: Proceedings of the 2004 Int. Symposium on Biomedical Imaging: From Nano to Macro, IEEE Computer Society, Washington, DC,, 2004, pp. 924–927.
- [35] H. Guo, A. Rangarajan, and S. Joshi, *Diffeomorphic point matching*, in: Handbook of Mathematical Models in Computer Vision, Springer, Berlin-Heidelberg-New York, 2006, pp. 205–219.
- [36] U. Grenander, and M. I. Miller, *Computational anatomy: an emerging discipline*, Quart. App. Math., **56** (1998), pp. 617–694.
- [37] U Grenander, Srivastava, A., Saini, S. *Characterization of biological growth using iterated diffeomorphisms* , ISBI. pp. 1136–1139
- [38] H. Guo, *Diffeomorphic point matching with applications in medical image analysis*, Ph.D. thesis, Department of Computer and Information Science and Engineering, University of Florida, Gainesville, FL, 2005.
- [39] B. Heyde, S. Cygan, H. F. Choi, B. Lesniak-Plewinska, D. Barbosa, A. Elen, P. Claus, D. Loeckx, K. Kaluzynski, J. Dhooge, *Three dimensional cardiac motion and strain estimation*, IEEE International Ultrasonics Symposium Proceedings, pp 15341537, 2010.
- [40] R.H.W. Hoppe,C. Linsenmann *An Adaptive Newton Continuation Strategy for the Fully Implicit Finite Element Immersed Boundary Method*, *Journal of Computational Physics*, 2011.
- [41] *S. Joshi and M. Miller*, Landmark matching via large deformation diffeomorphisms, *IEEE Trans. Image Processing*, **9** (2000), pp. 1357–1370.
- [42] *E. Klassen, A. Srivastava, W. Mio, and S. Joshi*, Analysis of planar shapes using geodesic paths on shape spaces, *IEEE Trans. Pattern Analysis and Machine Intelligence*, **26** (2004), pp. 372–383.

## BIBLIOGRAPHY

---

- [43] *J.L. Lions*, Controlabilité exacte, perturbation et stabilisation des syst'emes distribués, *Masson, Paris, 1988*.
- [44] *I. Miller, A. Trouvé, and L. Younes*, On the metrics and Euler-Lagrange equations of computational anatomy, *Ann. Review of Biomedical Engineering*, **4** (2002), pp. 375–405.
- [45] *M.I. Miller and L. Younes*, Group action, diffeomorphism and matching: A general framework, *Int. J. Comp. Vis.*, **41** (2001), pp. 61–84.
- [46] *A. Rangarajan, E. Mjolsness, S. Pappu, L. Davachi, S. Goldman Rakic, P. , and S. Duncan, J*, A robust point matching algorithm for autoradiograph alignment, in *Visualization in Biomedical Computing (VBC)*, *H. Hohne, K and R. Kikinis, eds.*, 1996, pp. 277–286.
- [47] *S. Saitoh*, Theory of Reproducing Kernels and its Applications, *Pitman Research Notes in Mathematics, Vol. 189, Longman, 1988*.
- [48] *L. Tartar*, Introduction to Sobolev Spaces and Interpolation Theory, *Springer, Berlin-Heidelberg-New York, 2007*.
- [49] *A. Trouvé*, Diffeomorphisms groups and pattern matching in image analysis, *Int. J. of Comp. Vis.*, **28** (1998), pp. 213–221.
- [50] *A. Trouvé and F.-X. Vialard*, Shape splines and stochastic shape evolution: A second order point of view, *To appear in Quarterly of Applied Mathematics, 2010*
- [51] *L. Younes*, Computable elastic distances between shapes, *SIAM J. Appl. Math.* **58** (1998), pp. 565–586.
- [52] *B. Zitová and J. Flusser*, Image registration methods: a survey, *Image and Vision Computing*, **21** (2003), pp. 977–1000.
- [53] *E. Zuazua*, Controllability and observability of partial differential equations, *Chapter 7 in Handbook of Differential Equations, Vol. 3, Evolutionary Equations, Elsevier, Amsterdam, 527-621, (2007)*.
- [54] *L. Piegl and W. Tiller*, The NURBS Book, *Berlin; Springer-Verlag (1997)*
- [55] *Ronan J. Curtin and Brian P. Griffin* The Cleveland Clinic Center for Continuing Education Mitral Valve Disease: Stenosis and Regurgitation, *Retrieved September 2010*

## BIBLIOGRAPHY

---

- [56] *L. Younes*, Shapes and Diffeomorphisms. *Springer, Berlin-Heidelberg-New York, 2010.*
- [57] *M Vaillant and Joan Glaunes*, Surface matching via currents *Proceedings of Information Processing in Medical Imaging, vol 3565, Springer, 2005*
- [58] *P Deufhard*, Newton Methods for Nonlinear Problems. Affine Invariance and Adaptive Algorithms. Springer, Berlin-Heidelberg-New York, 2004.
- [59] *M Weiser and P Deufhard*, *Inexact central path following algorithms for optimal control problems. SIAM J. Control Optim.* **46**, 792815, 2007